



## RESEARCH ARTICLE

10.1002/2013JB010436

## Key Points:

- Mantle convection supports 0.5–1 km of Eastern Highland topography
- Local fluvial erosion data enable dating of landscape uplift from river profiles
- River profile commonalities show dynamic topography grew during Cenozoic times

## Correspondence to:

K. Czarnota,  
karol.czarnota@ga.gov.au

## Citation:

Czarnota, K., G. G. Roberts, N. J. White, and S. Fishwick (2014), Spatial and temporal patterns of Australian dynamic topography from River Profile Modeling, *J. Geophys. Res. Solid Earth*, 119, 1384–1424, doi:10.1002/2013JB010436.

Received 18 JUN 2013

Accepted 9 JAN 2014

Accepted article online 15 JAN 2014

Published online 18 FEB 2014

## Spatial and temporal patterns of Australian dynamic topography from River Profile Modeling

K. Czarnota<sup>1,2</sup>, G. G. Roberts<sup>2,3</sup>, N. J. White<sup>2</sup>, and S. Fishwick<sup>4</sup>
<sup>1</sup>Geoscience Australia, Canberra, Australian Capital Territory, Australia, <sup>2</sup>Bullard Laboratories, Department of Earth Sciences, University of Cambridge, Cambridge, UK, <sup>3</sup>Now at Department of Earth Sciences and Engineering, Imperial College London, UK, <sup>4</sup>Department of Geology, University of Leicester, Leicester, UK

**Abstract** Despite its importance, the temporal and spatial evolution of continental dynamic topography is poorly known. Australia's isolation from active plate boundaries and its rapid northward motion within a hot spot reference frame make it a useful place to investigate the interplay between mantle convection, topography, and drainage. Offshore, dynamic topography is relatively well constrained and can be accounted for by Australia's translation over the mantle's convective circulation. To build a database of onshore constraints, we have analyzed an inventory of longitudinal river profiles, which is sensitive to uplift rate history. Using independently constrained erosional parameters, we determine uplift rates by minimizing the misfit between observed and calculated river profiles. Resultant fits are excellent and calculated uplift histories match independent geologic constraints. We infer that western and central Australia underwent regional uplift during the last 50 Myr and that the Eastern Highlands have been uplifted in two stages. The first stage from 120 to 80 Ma, coincided with rifting along the eastern margin and its existence is supported by thermochronological measurements. A second stage occurred at 80–10 Ma, formed the Great Escarpment, and coincided with Cenozoic volcanism. The relationship between topography, gravity anomalies, and shear wave tomographic models suggest that regional elevation is supported by temperature anomalies within the lithosphere's thermal boundary layer. Morphology and stratigraphy of the Eastern Highlands imply that these anomalies have been coupled to the base of the plate during Australia's northward motion over the last 70 Myr.

## 1. Introduction

Australia is an important natural laboratory for studying dynamic topography, generated by an interplay between plate motion and subplate convective circulation [Sandiford, 2007; DiCaprio *et al.*, 2009; Heine *et al.*, 2010]. Its importance stems from the continent's distance from active plate boundaries after Cretaceous times together with its rapid northward motion since Eocene times (70 km Myr<sup>−1</sup>). Offshore, the spatial and temporal pattern of dynamic topography is consistent with horizontal translation of Australia over a changing pattern of convective circulation (Figure 1a) [Czarnota *et al.*, 2013]. Here our principal aim is to investigate how methods for extracting uplift rate histories from drainage networks can be used to constrain the onshore evolution of dynamic topography. We start by reviewing independent constraints on Australian dynamic topography.

The Australian landscape is often thought of as being old, flat, and stable [e.g., Pain *et al.*, 2012]. Neo-Proterozoic landforms and Carboniferous weathering profiles indicate that in some places, modern topography has been inherited [Ollier *et al.*, 1988; Stewart *et al.*, 1986; O'Sullivan *et al.*, 2000; Pillans, 2005]. However, landscape preservation can be attributed to successive periods of burial and exhumation rather than to prolonged exposure [O'Sullivan *et al.*, 2000; Belton *et al.*, 2004; Weber *et al.*, 2005; Pillans, 2007].

During Middle Cretaceous times, >40% of Australia was flooded by a shallow sea (Figure 1a) [Frakes *et al.*, 1987; Langford *et al.*, 1995]. In northern and western Australia, lateritic weathering profiles developed over Cretaceous marine sediments (Figure 1a). Paleomagnetic dating shows that extensive chemical weathering occurred at ~60 Ma, which is consistent with low relief [Pillans, 2005, and references there in]. These uplifted marine deposits and weathering profiles suggest that the bulk of Australia has been uplifted since Late Cretaceous times.

Today, the east-dipping Western Plateau is separated from the Eastern Highlands by Lake Eyre, by the Murray-Darling basin, and by the Flinders Ranges (Figure 1b). Elevation of the Western Plateau is generally

This is an open access article under the terms of the Creative Commons Attribution License, which permits use, distribution and reproduction in any medium, provided the original work is properly cited.

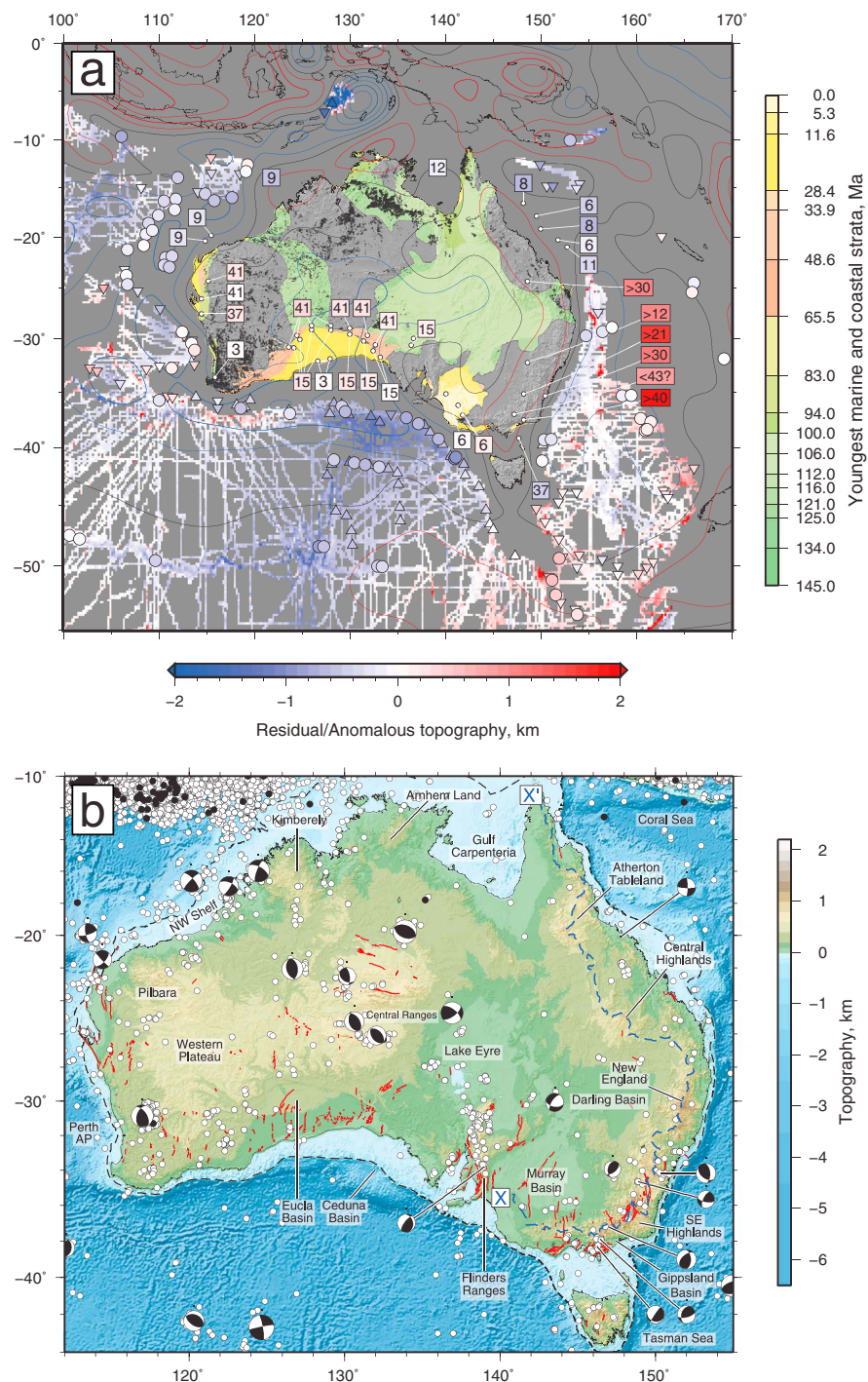


**Figure 1.** Australian topography and seismicity. (a) Map of residual bathymetry (i.e., dynamic topography) of oceanic lithosphere relative to oceanic age-depth curve from *Czarnota et al.* [2013]. Colored circles and upward/downward triangles = accurate estimates and lower/upper bounds of residual bathymetry from seismic profiles in  $2^\circ \times 2^\circ$  bins. Colored squares = relative epeirogenic movement (color = magnitude of movement, number = onset age in Ma). Filigree of lines = residual bathymetry from ship tracks corrected for sediment loading. Red/black/blue contours = positive/zero/negative contours of dynamic topography calculated from long-wavelength gravity anomalies assuming a water-loaded admittance of 23 mGal/km for the oceans; contour interval = 0.5 km [Czarnota et al., 2013]. Colored polygons = youngest onshore marine and coastal strata [Langford et al., 1995]. Black polygons = laterites [Raymond et al., 2012]. (b) Shuttle Radar Topography Mission (SRTM) topography, seismicity, and Neogene faults. Black dots and white circles = epicenters of earthquakes  $M_w$  4–6 and  $>6$ , respectively (Incorporated Research Institutions for Seismology catalog, 1973–2012). Earthquake focal plane solutions  $M_w$  or  $M_L \geq 4.5$  from centroid moment tensor catalog and  $P$  wave polarity local network studies with  $\geq 25$  stations and quality rating  $\geq C$  [Zoback, 1992; Leonard et al., 2002]. Fault plane solutions of largest earthquakes in a cluster are shown. Red lines = Neogene faults [Clark et al., 2011]. Black dashed line = edge of continental shelf. Blue dashed line = Eastern Highlands drainage divide, labeled X–X'.

< 600 m; local highs in the Pilbara and Central Ranges exceed 800 m. Maximum elevation of the Eastern Highlands rarely exceeds 1500 m with saddle elevations of 400–600 m. These highlands comprise two broad domal swells in the north and a strip of elevated topography, which follows the coastline southward. Distance of the drainage divide from the coast emulates the width of the adjacent continental shelf. In contrast, the Great Escarpment is located < 150 km from the coast along the whole length of the Eastern Highlands [Ollier, 1982]. Highland relief is generally low and the region is characterized by plateaux at different elevations [Bishop, 1989].

Earthquake focal mechanisms and the predominance of Neogene thrust faults show that the Australian plate is in a state of compression [Leonard *et al.*, 2002; Hillis *et al.*, 2008; Clark *et al.*, 2011]. Seismicity is generally sparse but discrete bands coincide with topographic relief in the Flinders Ranges and in the South-eastern Highlands (Figure 1b) [Sandiford *et al.*, 2004; Sandiford and Quigley, 2009; Braun *et al.*, 2009; Quigley *et al.*, 2010]. In these regions, strain rates of up to  $\sim 10^{-16} \text{ s}^{-1}$  have been estimated from seismic moment release and from Quaternary slip rate data [Sandiford *et al.*, 2004; Braun *et al.*, 2009]. Dating of onshore and offshore faulting and models of plate-scale stress indicates that the associated east-west oriented principal stress axis developed between 5–10 Ma ago [Coblentz *et al.*, 1995; Reynolds *et al.*, 2002; Sandiford *et al.*, 2004]. Extrapolating these strain rates over the last 10 Myr indicates that < 200 m of regional uplift can be attributed to the east-west compressive stress field when flexure is considered, suggesting the landscape is predominantly sculpted by epirogenic processes [Braun *et al.*, 2009].

## 2. Geophysical and Geologic Constraints

There is a fragmented record of Cenozoic vertical motion preserve along the edges of the Western Plateau, Pilbara, Kimberley, and Arnhem Land, all of which currently sit on thick lithosphere (Figure 2d). Rapid regional uplift is recorded by paleoshorelines in the Eucla Basin, on the southern edge of the Western Plateau [Sandiford, 2007]. These paleoshorelines record  $\sim 300$  m of uplift since  $\sim 40$  Ma [Hou *et al.*, 2008]. The present-day tilt of these paleoshorelines matches that of the Western Plateau. Uplifted marine sedimentary rocks of a similar age and elevation occur at isolated localities along the western side of this plateau (Figure 1a) [Collins and Baxter, 1984; Haig and Mory, 2003]. In contrast, subsidence analyses from the Northwest Shelf show that northwestern Australia has been drawn down by up to 700 m during the last  $\sim 9$  Ma [Czarnota *et al.*, 2013]. Combining these observations with residual depth estimates from oceanic crust reveals a diachronous pattern of long-wavelength vertical motion. Southern Australia has steadily emerged from a broad region of drawdown which now coincides with the Australian-Antarctic Discordance. More recently, northern Australia has started to submerge as it drifts toward Southeast Asia [Lithgow-Bertelloni and Gurnis, 1997; Sandiford, 2007; Czarnota *et al.*, 2013].

The uplift history of the Eastern Highlands is controversial [e.g., Bishop, 1982; Jones and Veevers, 1982; Lambeck and Stephenson, 1985; Wellman, 1987; Ollier and Pain, 1994; Persano *et al.*, 2002]. Maximum age of uplift is constrained by elevated marine Cretaceous sedimentary rocks in the north and by uplifted Triassic deltaic sequences of the Sydney Basin in the south (Figure 2a) [Wellman, 1987]. The minimum age is constrained by the vertical extent of paleochannels infilled by Cenozoic basalts [Wellman and McDougall, 1974b; Wellman, 1987]. In southeastern Australia, subaerially erupted basalts, which are  $\sim 30$  Ma, occur at an elevation of  $\sim 30$  m along the coast. Their existence implies that the erosional Great Escarpment was established by this time and that negligible uplift has subsequently occurred [Young and McDougall, 1982]. Similar observation from the Central Highlands suggests that the escarpment developed before 30 Ma with a maximum of 150 m of subsequent uplift [Young and Wray, 2000]. The uplift history between Triassic/Cretaceous and mid-Oligocene times is largely unconstrained although thermochronological data show that a significant phase of rock cooling occurred between 80 and 100 Ma [Gleadow *et al.*, 2002; Persano *et al.*, 2002].

Models of the Eastern Highlands often attribute regional uplift either to faulting, to magmatic underplating, to rifting of the Tasman Sea, or to erosion of pre-existing topography [Wellman, 1979b; Bishop, 1982; Jones and Veevers, 1982; Lambeck and Stephenson, 1985; Lister and Etheridge, 1989; Van Der Beek *et al.*, 1999; Persano *et al.*, 2005; Holdgate *et al.*, 2008]. These models assume that the crust beneath the Eastern Highlands is isostatically compensated. At the southeastern end, crustal thickness and topography do correlate, which suggests that crustal isostatic compensation is locally important [Wellman, 1979a; Young, 1989]. However, high elevations coincide with positive long-wavelength free-air gravity anomalies and with a belt of



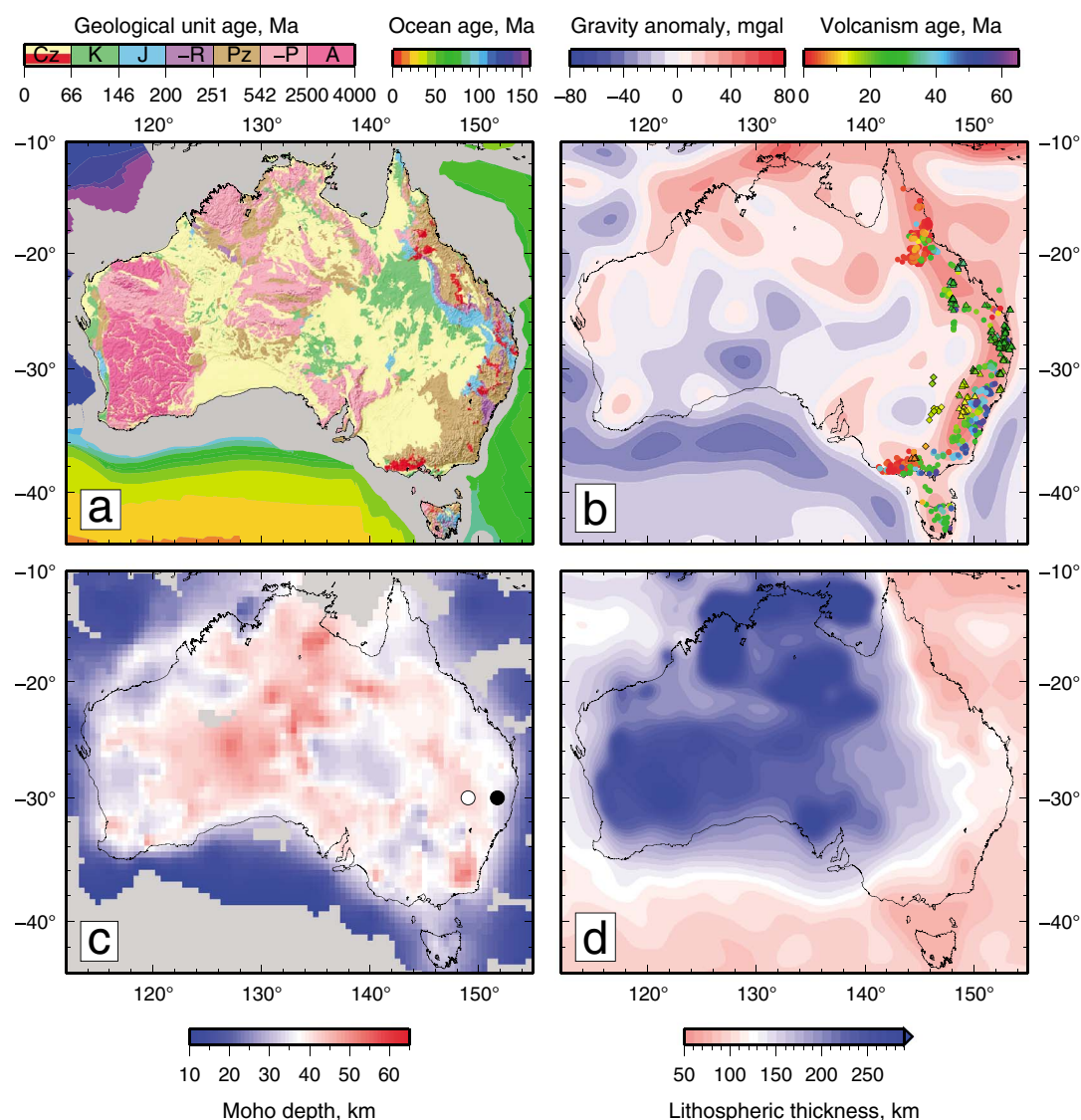


**Figure 2.** (a) Onshore 1:2,500,000 geological map of Australia shaded by topography [Raymond *et al.*, 2010]. Cenozoic Era strata subdivided into sedimentary (yellow) and volcanics (red) rocks. Oceanic crustal age from Müller *et al.* [2008]. (b) EIGEN6c gravity filtered to exclude wavelength less than ~500–800 km [Förste *et al.*, 2011]. Colored symbols = Cenozoic volcanism [Vasconcelos *et al.*, 2008]; circles = mafic lava fields; triangles = central bimodal volcanoes; diamonds = leucite volcanoes. (c) Depth to Moho [Salmon *et al.*, 2013]. White circle = 45 km thick crust, 0.16 km elevation; black circle = 35 km thick crust, 1.4 km elevation. (d) Lithospheric thickness based on surface wave tomography converted to lithospheric thickness [Priestley and McKenzie, 2006; Fishwick and Rawlinson, 2012].

thinner lithosphere. These observations indicate that subcrustal processes play a role in generating highland topography (Figures 2b and 2d). It is instructive to compare crustal thicknesses and elevations around the Eastern Highlands (Figure 2c). For example, at  $-30^{\circ}\text{S}$  and  $152^{\circ}\text{E}$ , the crust is 35 km thick with an elevation of 1.4 km. At  $-30^{\circ}\text{S}$  and  $149^{\circ}\text{E}$ , the crust is 42 km thick and 160 m high. These observations require sub-crustal density variations.

## 2.1. Admittance Analysis

At short ( $< 10^2$  km) wavelengths, topography is supported by lithospheric flexure. At longer wavelengths, topography is usually supported isostatically (i.e., by lithospheric density variation) and/or dynamically (i.e., by mantle convective processes). The admittance,  $Z$ , is defined as the ratio of free-air gravity and topography anomalies in the spectral domain. Its variation as a function of wave number allows the mechanism of topographic support to be constrained, provided that topography and gravity anomalies are coherent [Watts, 2001; McKenzie, 2010]. Here we have calculated  $Z$  for a box, which encompasses Eastern Australia,



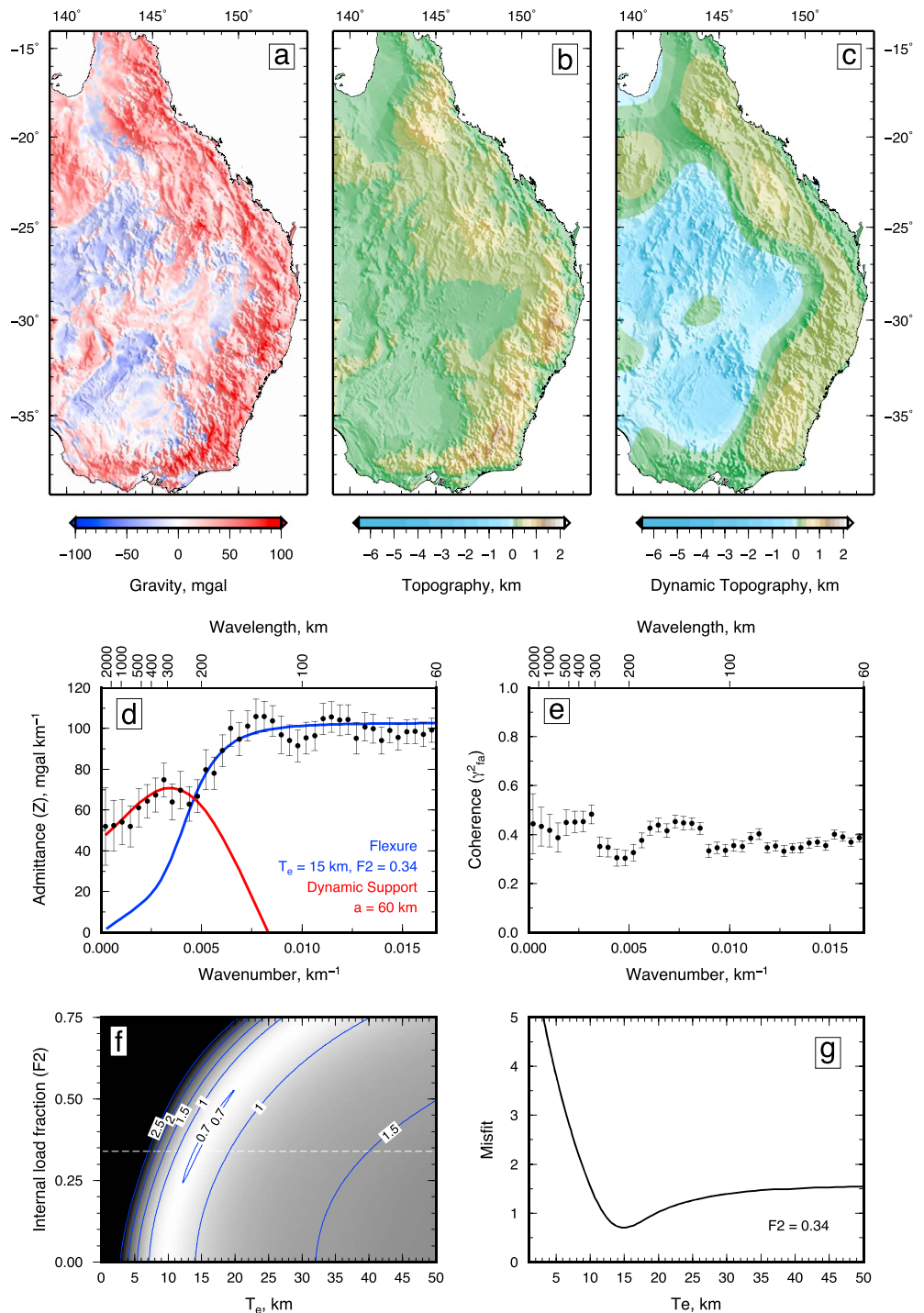


**Figure 3.** Admittance between gravity and topography in eastern Australia. (a) Onshore EIGEN6c gravity shaded by topography [Förste *et al.*, 2011]. (b) Decimated SRTM topography. (c) Predicted dynamic topography shaded by topography. Filtered gravity data to exclude wavelengths  $<500$ – $800$  km divided by an admittance of  $52 \text{ mGal km}^{-1}$ . (d) Admittance,  $Z$ , plotted as function of wave number and wavelength, for data shown in Figure 3a. Solid circles with error bars =  $Z$  with  $1\sigma$  error within wave number bands. Blue solid line = predicted values of  $Z$ , calculated using an elastic model, which best fit observed values (elastic thickness,  $t_e = 15$  km for internal load fraction,  $F2 = 0.34$ ) [McKenzie, 2003]. Crustal thickness =  $38$  km (mean for eastern Australia) [Salmon *et al.*, 2013]; upper crustal thickness and density =  $10$  km and  $2.45 \text{ Mg/m}^3$ , lower crustal thickness and density =  $28$  km and  $2.85 \text{ Mg/m}^3$ . Note observed admittance of  $\sim 52 \text{ mGal km}^{-1}$  at longest wavelengths, indicative of dynamic support. Red solid line = predicted dynamic support values of  $Z$ , calculated using an analytical solution to Stokes flow equation, which best fits observed values ( $t_e = 15$  km, mechanical lithospheric thickness,  $a = 60$  km) [McKenzie, 2010]. (e) Coherence between free-air gravity and topography plotted as a function of wave number. (f) Misfit as a function of elastic thickness and internal loads. White dashed line = slice through minimum misfit shown in Figure 3g. (g) Misfit as a function of elastic thickness for an internal load fraction of  $0.34$ . Minimum RMS misfit =  $0.70$ .

using the spectral method of *McKenzie and Fairhead* [1997, Figures 3a–3c]. The size of this box is predicated by the need to minimize spectral leakage, to recover  $Z$  up to wavelengths of  $10^3$  km, and to avoid regions with low coherence between gravity and topographic signals [*Crosby*, 2007]. We have omitted central and western Australia where a combination of subdued topographic relief and large internal loads yields a mean coherence,  $\overline{\gamma_{fa}^2}$ , of  $< 0.1$  [*Goleby et al.*, 1989; *McKenzie and Fairhead*, 1997; *McKenzie*, 2003]. The Shuttle Radar Topography Mission (SRTM) topography and EIGEN6c gravity data sets were used to calculate  $Z$  [*Farr et al.*, 2007; *Förste et al.*, 2011]. The EIGEN6c data set combines Gravity Recovery and Climate Experiment and Gravity Field and Steady-State Ocean Circulation Explorer satellite measurements to spherical harmonic degree 240 (i.e.,  $\lambda \approx 167$  km) with land station gravity data between degrees 160 and 1420 (i.e.,  $\lambda \approx 30$ –250 km). Since Australia is densely covered in land stations with a minimum spacing of 11 km, the EIGEN6c data set is reliable at short wavelengths [*Wynne and Bacchin*, 2009]. The gravity signal is noisier than the topographic signal; therefore,  $Z$  as a function of wave number,  $k = 2\pi/\lambda$ , is given by

$$Z(k) = \left| \frac{\langle \Delta g t^* \rangle}{\langle t t^* \rangle} \right|, \quad (1)$$

where  $\Delta g$  and  $t$  are the multitaper Fourier transforms of gravity and topography,  $\langle \rangle$  represents annular averages over wave number bands, and  $*$  denotes the complex conjugate [*McKenzie and Fairhead*, 1997]. The coherence is given by

$$\gamma_{fa}^2 = \frac{\langle \Delta g t^* \rangle^2}{\langle t t^* \rangle \langle \Delta g \Delta g^* \rangle}. \quad (2)$$

Our results are summarized in Figure 3d. At wavelengths of  $< 150$  km,  $Z \sim 100$  mGal km $^{-1}$ , which is a measure of upper crustal density (i.e.,  $\rho_{uc} = 2.45$  kg m $^{-3}$ ). This value is consistent with the density of unconsolidated Cenozoic sedimentary rocks and weathered basement rocks (Figure 2).  $Z$  decreases rapidly between wavelengths of 150 and 250 km which constrains the elastic thickness of the plate,  $T_e$ . By minimizing the difference between observed and predicted admittance, we obtained  $T_e = 15_{-5}^{+15}$  km. This estimate accounts for the presence of internal crustal loads using the method of *McKenzie* [2003, Table 1]. It agrees with values of 15–35 km obtained by *Zuber et al.* [1989] who ignored the effects of internal loading and used a coherency method even though  $\gamma_{fa}^2 = 0.4$ . In the absence of dynamic support,  $Z$  should decrease to zero with increasing wavelength. In Eastern Australia,  $Z \approx 50$  mGal km $^{-1}$  at wavelengths  $> 500$  km, which is indicative of dynamic support. Similar values have been estimated in the oceanic realm and in Africa, where long-wavelength topography is maintained by sublithospheric convective circulation [*Crosby and McKenzie*, 2009; *Jones et al.*, 2012]. Numerical convective experiments predict  $Z \sim 50$  mGal km $^{-1}$  [*Anderson et al.*, 1973; *McKenzie et al.*, 1980; *Parsons and Daly*, 1983]. We assume that a thermal anomaly,  $T(x, z)$ , located below the base of the mechanical lithosphere can be described using

$$T(x, z) = T_0 \exp(kz) \cos(kx), \quad (3)$$

where  $T_0$  determines the amplitude of a thermal anomaly. The admittance at wavelengths  $> 250$  km is described by an analytical solution of the Stokes Equation (Table 1) [*McKenzie*, 2010]. This solution is sensitive to the value of elastic thickness and to the location of the base of the mechanical boundary layer. For  $T_e = 15_{-5}^{+15}$  km, the best-fitting distribution of  $Z$  is obtained for a mechanical boundary layer thickness of 60–80 km (Figure 3d). This range is consistent with the depth of the deepest mantle nodules from Cenozoic volcanic fields across the Eastern Highlands [*Ferguson et al.*, 1979; *O'Reilly and Griffin*, 1985]. Thus, it is possible that a thermal anomaly located within or below the thermal boundary layer of the lithosphere maintains Eastern Highland topography [cf. *Parsons and Daly*, 1983; *Demidjuk et al.*, 2007]. The amplitude of this support can be estimated by dividing long-wavelength free-air gravity by an admittance of  $\sim 50$  mGal km $^{-1}$ . Figure 3c shows that the estimated dynamic topography closely matches the observed topography of the Eastern Highlands. Immediately to the west, a region of downwelling could account for the loci of the Murray, Darling, and Lake Eyre basins.

The amount of topography,  $e$ , supported by variations in crustal thickness and density can be predicted by balancing a column of continental lithosphere against a mid-oceanic ridge so that

$$e = \frac{\alpha(\rho_a - \rho_m) + t_c(\rho_m - \rho_c) + t_{oc}(\rho_{oc} - \rho_a) + t_w(\rho_w - \rho_a)}{\rho_m}, \quad (4)$$

**Table 1.** List of Parameters Used in Admittance and Isostatic Balance Calculations

Variable	Description	Value	Units
<i>Common Variables</i>			
$\rho_m$	Density of lithospheric mantle	$3.3 \times 10^3$	$\text{kg m}^{-3}$
$\rho_w$	Density of sea water <sup>a</sup>	$1.0 \times 10^3$	$\text{kg m}^{-3}$
$g$	Acceleration due to gravity	9.81	$\text{m s}^{-2}$
<i>Variables for Admittance Analysis</i>			
$t_e$	Elastic thickness		m
$\lambda$	Wavelength		m
$t_u$	Thickness of upper crust	$10 \times 10^3$	m
$t_l$	Thickness of lower crust <sup>b</sup>	$28 \times 10^3$	m
$k$	Wave number ( $2\pi/\lambda$ )		$\text{m}^{-1}$
$\rho_u$	Upper crust density <sup>c</sup>	$2.45 \times 10^3$	$\text{kg m}^{-3}$
$\rho_l$	Mean lower crust density <sup>d</sup>	$2.85 \times 10^3$	$\text{kg m}^{-3}$
$E$	Young's modulus	$9.5 \times 10^{10}$	Pa
$T_0$	Thermal anomaly	100	$^{\circ}\text{C}$
$\alpha$	Thermal expansivity	$4 \times 10^{-5}$	$^{\circ}\text{C}^{-1}$
$\sigma$	Poisson's ratio	0.29	dimensionless
<i>Variables for Isostatic Balance</i>			
$e$	Elevation above sea level		m
$t_c$	Thickness of continental crust		m
$t_w$	Mean ocean ridge axial depth	$2.8 \times 10^3$	m
$t_{oc}$	Thickness of oceanic crust	$7.1 \times 10^3$	m
$a$	Lithospheric thickness	$100\text{--}110 \times 10^3$	m
$\rho_{oc}$	Density of oceanic crust	$2.86 \times 10^3$	$\text{kg m}^{-3}$
$\rho_c$	Mean density of continental crust <sup>e</sup>	Gridded in Figure 4	$\text{kg m}^{-3}$
$\rho_a$	Density of the asthenosphere	$3.2 \times 10^3$	$\text{kg m}^{-3}$

<sup>a</sup>For air-loaded  $t_e$  calculations  $\rho_w$  is set to zero.

<sup>b</sup> $t_u + t_l$  = average crustal thickness of Eastern Australia from Australian Seismological Reference Model (AusREM) [Salmon *et al.*, 2013].

<sup>c</sup>Density of topography which corresponds to the admittance at short wavelengths.

<sup>d</sup>Average crustal density for Eastern Australia from AusREM model [Salmon *et al.*, 2013].

<sup>e</sup>Mean density of crustal column along transect shown in Figures 4b and 4c.

where values of parameters are given in Table 1. We assume that the thickness and density of the lithospheric mantle are constant, and use the AusREM model of Salmon *et al.* [2013] to define crustal thicknesses and densities. In the Eastern Highlands, we find that there is considerable residual topography which matches long-wavelength gravity anomalies and which cannot be accounted for by crustal isostasy alone. If, for example, the Eastern Highlands are compensated at the base of the crust predicted and observed topography ought to be similar. Figures 4e and 4f show that predicted topography is fairly uniform. These observations can be accounted for by differences in the density structure of the mantle. It is noteworthy that lithospheric thickness variations determined from surface wave tomography broadly correlate with topography and with the pattern of volcanism (Figures 4a–4d).

## 2.2. Magmatism

Eastern Australia is peppered by Cenozoic volcanism, which tracks the drainage divide and supports the notion arising from the geophysical analysis that a significant thermal anomaly occurs beneath the Eastern Highlands (Figures 2a–2b) [O'Reilly and Zhang, 1995]. Volcanism can be divided into at least two categories: mafic lava fields and bimodal central volcanoes. The volcanoes progressively young southward and record Australia's  $\sim 70 \text{ km Myr}^{-1}$  northward translation within a hot spot reference frame [Wellman and McDougall, 1974a; Knesel *et al.*, 2008]. In contrast, the lava fields have no systematic age progression. Instead, scattered eruptions occur along the length of the Eastern Highlands between  $\sim 70 \text{ Ma}$  and the termination of central volcano volcanism (Figure 5a). These lavas have ocean island basalt source affinities contaminated by sub-continental lithospheric mantle [O'Reilly and Zhang, 1995]. Mafic granulitic and rare eclogitic xenoliths suggest high geothermal gradients at the time of volcanism, and widespread intrusion of mafic material at the base of the crust (i.e., underplating) [Lovering and White, 1969; O'Reilly and Griffin, 1985; Griffin *et al.*, 1987; O'Reilly *et al.*, 1988; Roach, 2004]. These high geothermal gradients are consistent with  $> 90 \text{ mW m}^{-2}$  heat flow measurements in areas of recent ( $< 10 \text{ Ma}$ ) volcanism [Purss and Cull, 2001].



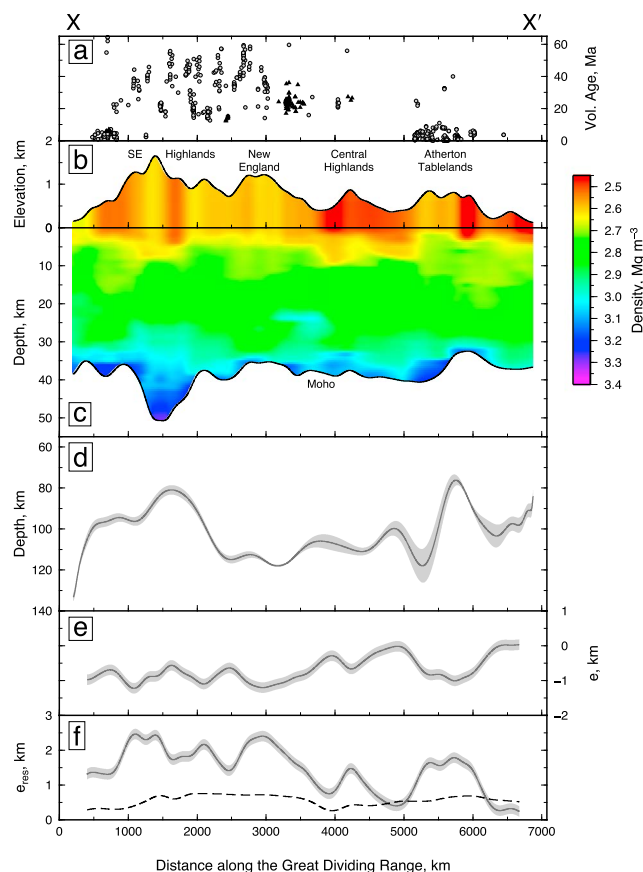


**Figure 4.** Crustal isostatic balance along crest of Great Dividing Range, X-X' in Figure 1b. (a) Cenozoic volcanism within a 50 km swath of the Great Divide; symbols as in Figure 5. (b-c) Topography and Moho depth along the Great Divide; density from *P* wave velocities [Salmon et al., 2013]. (d) A 25 km wide swath along the Great Divide of lithospheric thickness (Figure 2d). (e) Crustal isostatic elevation, *e*, as a function of distance along the Great Divide calculated using equation (4). (f) Residual topography,  $e_{res}$  = observed topography - *e*; dashed line = dynamically supported topography calculated from long-wavelength gravity using an admittance of 52 mGal km<sup>-1</sup> (Figures 2b and 3d); gray band in Figures 4e-4f = uncertainty arising from a reference lithospheric thickness of 105 ± 5 km. All profiles have been 400 km Gaussian filtered to remove high-frequency variations. Notice elevation of Eastern Highland cannot be accounted for by crustal isostasy, implying that it must be controlled by changes in mantle lithospheric thickness and density and/or subplate thermal anomalies.

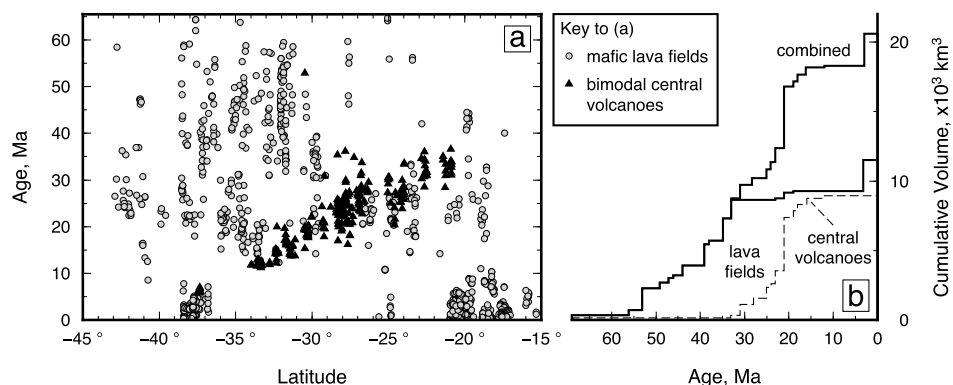


**Figure 5.** East Australian Cenozoic volcanism. (a) Age of volcanism as a function of latitude after Vasconcelos et al. [2008]. Notice strong progression in bimodal central volcanoes at a rate of ~70 km Myr<sup>-1</sup> [Wellman and McDougall, 1974a]. (b) Cumulative volume of volcanism as a function of age [Wellman and McDougall, 1974a].

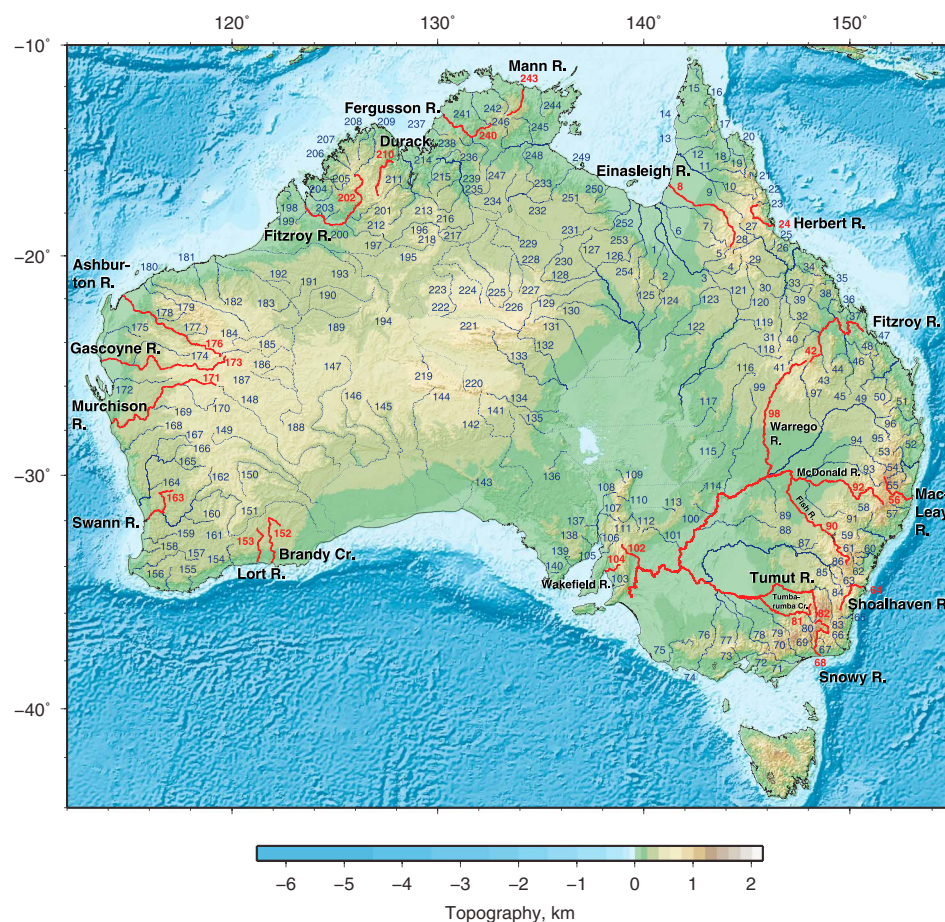


**Figure 6.** Topographic map of Australia illuminated from north and west. Numbered lines = rivers extracted from SRTM data set [Farr *et al.*, 2007] (see Table A1). Solid lines = real rivers; dashed lines = interconnected lakes and/or paleodrainage; dotted lines = artifacts of the extraction process, localized to region of internal drainage around Lake Eyre, and karst drainage in Eucla Basin.

The age of magmatic underplating is unknown. However, equilibration temperatures and pressures from phenocrysts of Cenozoic Central Highland basalts are consistent with magma fractionation at Moho depths [Ewart *et al.*, 1980]. A combination of seismic wide-angle and receiver function profiles from the south-eastern highlands reveal thick (35–55 km) crust with  $V_p$  velocities of 7.35–8.08 km s<sup>-1</sup> and  $V_s$  velocities of > 4 km s<sup>-1</sup> [Finlayson, 1979; Tkalčić *et al.*, 2012]. These velocities are consistent with magmatic underplating which may have caused some of the regional uplift [Christensen, 1982; Johnson, 1989; Lister and Etheridge, 1989]. However, the pronounced crustal root beneath the Snowy Mountains probably makes a negligible contribution to uplift because of its high density (Figure 4c).

### 3. Drainage Patterns

Longitudinal river profiles are sensitive to spatial and temporal variations in uplift [e.g., Whipple and Tucker, 1999; Schoenbohm *et al.*, 2004; Roberts and White, 2010; Roberts *et al.*, 2012a]. Given that it is mostly arid, Australia would seem to be an unlikely place to exploit this sensitivity. However, extensive temperate and wet rain forests prevailed until late Miocene times [Kershaw *et al.*, 1994; Macphail *et al.*, 1994]. In early Pleistocene (0.78–2.59 Ma) times, a transition to arid conditions coincided with a change from freshwater to evaporitic and gypsiferous deposition within lakes of the Western Plateau, of the Central Ranges and of the Murray Basin [Zheng *et al.*, 1998; Chen and Barton, 1991; English *et al.*, 2001; Dodson and Lu, 2005; McLaren and Wallace, 2010; Fujioka and Chappell, 2010]. In late Pleistocene times, particularly during the last glacial maximum, dune fields were established [Herczeg and Chapman, 1991; Chen *et al.*, 1991; Nanson *et al.*, 1992; Hesse *et al.*, 2004]. The youthfulness of this aridity makes it possible to identify and map out extensive drainage systems.



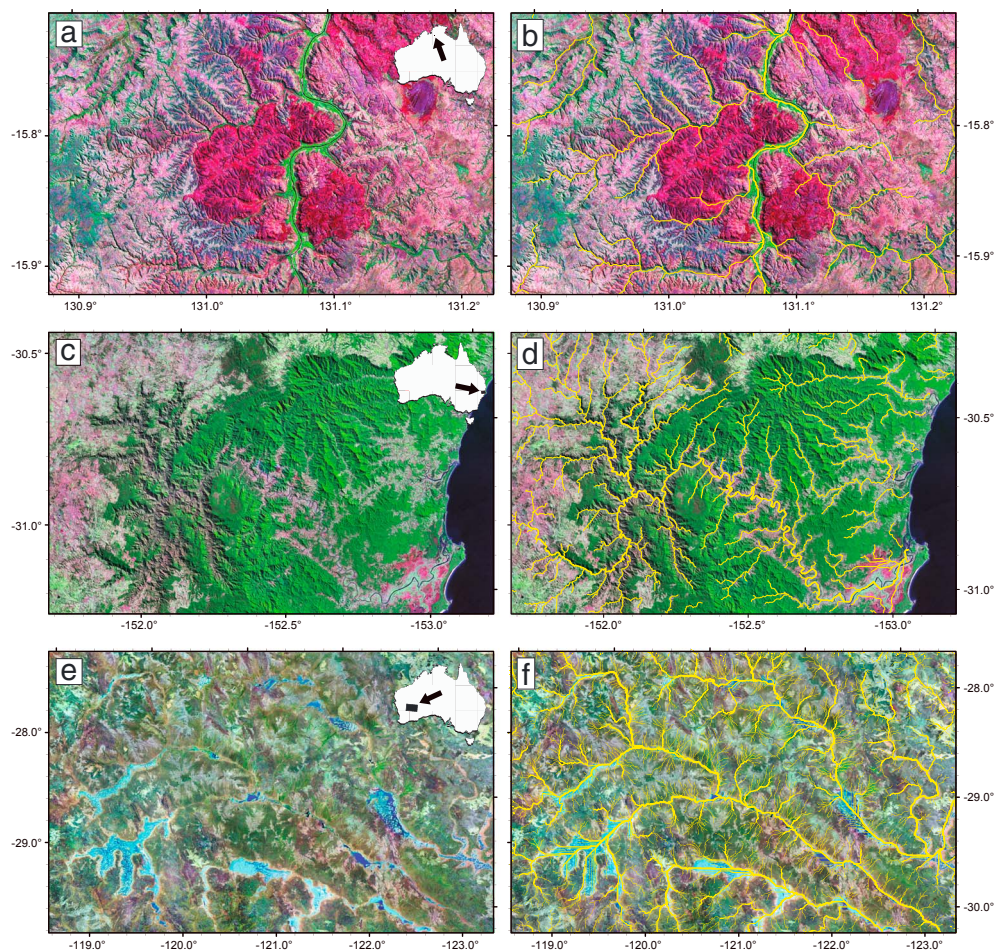


**Figure 7.** Comparison of SRTM-derived drainage with Landsat data at three scales. (a) Landsat image (RGB = bands 2, 4, 7) over Victoria River (214–218 in Figure 6), illumination from northeast. Black box on inset map = location of Landsat data. (b) Yellow lines = SRTM-derived drainage. (c–d, e–f) As above, for MacLeay River knickzone (river 56) and interconnected lakes along Ponton Creek (river 149), respectively. Planform drainage discrepancies of up to 5 km are restricted to low slope river channels (Figures 7b and 7f) and estuaries (Figure 7d). Straight line drainage segments in Figure 7f illustrate artifacts arising from internal drainage.

We extracted 254 river profiles of Strahler order  $\geq 4$  from the 90 m SRTM data set (Figure 6) [Strahler, 1952; Farr *et al.*, 2007]. The fidelity of recovered drainage networks is ensured by a three stage process. First, local sinks and spikes were removed. Second, a drainage network was reconstructed by calculating flow directions (Figure 7). Finally, sets of longitudinal river profiles were extracted from this data set which best match drainage patterns imaged by satellites (Figures 7a–7d and Table A1). However, planform discrepancies of  $> 1$  km occur in anabranching river channels on very low gradient depositional slopes (e.g., the Murray-Darling Basin). Elevations of longitudinal river profiles located within 1 km of spot heights measured by the Global Navigation Satellite System are consistently 20–30 m lower [Brown *et al.*, 2011]. Comparison with published river profiles derived from topographic maps are also in good agreement although our recovered profiles are  $\sim 20\%$  longer in headwater regions [Wellman, 1979b; Young and McDougall, 1993; van der Beek and Bishop, 2003]. We attribute this difference to the superior spatial resolution of SRTM data.

The drainage network is divided into three groups consisting of present-day river channels, paleoriver channels, and artifacts (Figure 6). Paleoriver channels comprise interconnected lake systems partially infilled by alluvial sediments (e.g., Figures 7e–7f). Southwest of the Central Ranges and between the Pilbara and the Kimberley, paleoriver channels often consist of depressions within dune fields which constitute a drainage pattern. There are two important sources of artifacts, both of which stem from the requirement that drainage from any point must reach the coast. Thus, internal drainage basins are not preserved and all rivers drain to the coast via interconnected lakes. An extreme example is the Lake Eyre Basin where rivers drain to an elevation of  $\sim 80$  m above sea-level, controlled by the divide, separating Lake Eyre and Lake



Torrens, which formed during Late Miocene times [Sandiford *et al.*, 2009]. A second form of artifact occurs when rivers are forced to reach the coast despite evidence for karstic drainage (e.g., the Eucla Basin). We have included some of these profiles since their upstream tracts contain useful information.

Many Australian river profiles have irregular, convex-upward shapes (Figure 8). Knickzones of 20–50 km wide can separate segments with lower relief and these knickzones can contain multiple knickpoints < 5 km wide. Ollier [1982] suggested that prominent knickzones along eastward-draining rivers indicate erosion of the Great Escarpment. Knickzones with similar amplitudes occur at common elevations along westward-draining highland rivers. Elevations of both east- and west-facing knickzones match the amplitude of dynamic support (Figures 8a–8j). This spatial correlation suggests that the pattern of knickzones is an expression of the growth of dynamic topography along the east coast. On the southwest side of the continent, river profiles have consistent convex-up profiles with knickzone amplitudes of 200–300 m.

It is unlikely that lithology alone controls knickzone morphology (Figure 8). Figures 8j and 8o show that changes in lithology and patterns of Neogene faulting can generate short-wavelength knickpoints with amplitudes of ~100 m. However, these short-wavelength features do not control the overall form of a river profile. The correlation between changes in tensile strength of channel substrate,  $\Delta\sigma_t$ , a proxy for rock erodibility, and both slope and curvature along a profile is shown for three rivers in Figure 9. Our results suggest that there might be negligible lithologic control along the Tumut, Snowy, and Shoalhaven rivers. In their catchment-wide study of the Lachlan River, Bishop and Goldrick [1999] concluded that lithology plays a minor role in controlling profile morphology [cf. Bishop *et al.*, 1985]. This conclusion agrees with the results of mapping subbasaltic river profiles throughout the Eastern Highlands whose morphology is dominated by the headward propagation of knickzones [Young and McDougall, 1993; Nott *et al.*, 1996].

#### 4. Uplift Histories From River Profiles

Recent work has shown that inverse algorithms can successfully determine the spatial and temporal evolution of uplift rate history from longitudinal river profiles [Pritchard *et al.*, 2009; Roberts and White, 2010; Roberts *et al.*, 2012a, 2012b]. The rate of change of elevation along a river profile,  $\partial z/\partial t$ , is given by

$$\frac{\partial z}{\partial t} = U(x, t) + E(x, t), \quad (5)$$

where  $z$  and  $x$  are elevation and distance along a given river profile,  $U$  is the uplift rate which can vary through space and time,  $t$ , and  $E$  is the rate of erosion [e.g., Rosenbloom and Anderson, 1994; Whipple and Tucker, 1999]. River profiles can be modeled by bedrock channel incision where  $E$  is given by

$$E(x, t) = -vA(x)^m \left( \frac{\partial z}{\partial x} \right)^n + \kappa \frac{\partial^2 z}{\partial x^2}. \quad (6)$$

The left-hand, advective term describes how a kinematic wave travels upstream in accordance with the well-established detachment-limited stream power model [e.g., Howard *et al.*, 1994; Whipple and Tucker, 1999].  $m$  and  $n$  help to determine the transient shape of a river profile.  $A(x)$  is upstream drainage area and  $A(x)^m$  is related to fluvial discharge [Hack, 1957]. If  $n = 1$  and  $m = 0$ , then  $v$  is, by definition, the knickzone retreat velocity. If  $n \neq 1$  and  $m > 0$ , the advective velocity becomes a nonlinear function of local slope and upstream drainage area. The second term is an approximation of the transport-limited component of erosion, where  $\kappa$  is “erosional diffusivity” [e.g., Willgoose *et al.*, 1991; Whipple and Tucker, 1999]. This downwearing term allows synchronous erosion along the length of a river [Rosenbloom and Anderson, 1994].

The challenge is to solve the inverse problem. Given a river profile, its upstream drainage area, and values of  $v$ ,  $m$ ,  $n$ , and  $\kappa$ , can  $U(x, t)$  be determined? Pritchard *et al.* [2009] and Roberts and White [2010] used synthetic and observational data sets to demonstrate that  $U$  is recoverable if upstream drainage area is invariant. Along the Eastern Highlands, the distribution of Cenozoic lavas suggests that the crest of the Great Dividing Range and the locations of individual rivers have remained largely fixed since Early Cenozoic times [e.g., Young, 1983; Bishop *et al.*, 1985; Taylor *et al.*, 1985; Young and McDougall, 1985, 1993; Nott, 1992]. Paleocurrent data from North Queensland imply that this drainage divide may have persisted since Mesozoic times [Nott and Horton, 2000]. However, large-scale drainage reversal and reorganization does occur in regions with low relief (e.g., along northwestern edge of the Western Plateau) [Sandiford *et al.*, 2009]. In these areas, we have excluded anomalous river profiles from inverse modeling.

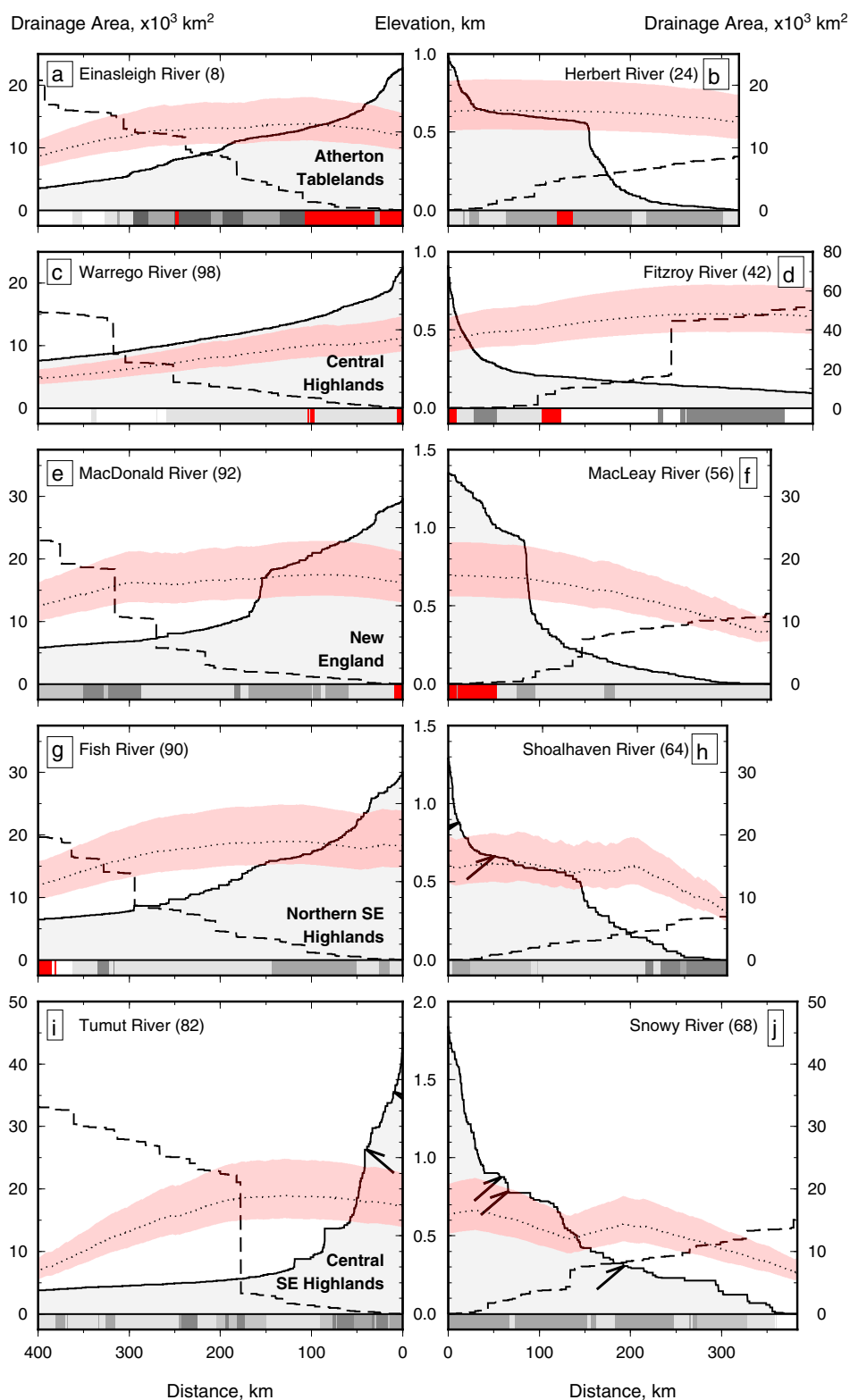


**Figure 8.** (a–j) Example river profiles draining Eastern Highlands. Solid gray line = longitudinal river profile (elevation as a function of distance along river); dashed line = upstream drainage area; gray and red stripes below each profile = geology along river profile (for key, see overleaf Raymond *et al.* [2010]); black arrows = location of Neogene reverse faults [Clark *et al.*, 2011, Figure 1]. Dotted line and red band = dynamic support calculated from EIGEN6c gravity low-pass filtered to exclude wavelengths <500–800 km using an admittance of  $52.4 \pm 12.4 \text{ mGal km}^{-1}$  [Förste *et al.*, 2011, Figure 3]. Notice correspondence between elevation of knickzones and calculated dynamic support. Right- and left-hand column rivers drain to east and west, respectively. For locations, see Figure 6. (k–t) Example river profiles from central and western Australia.

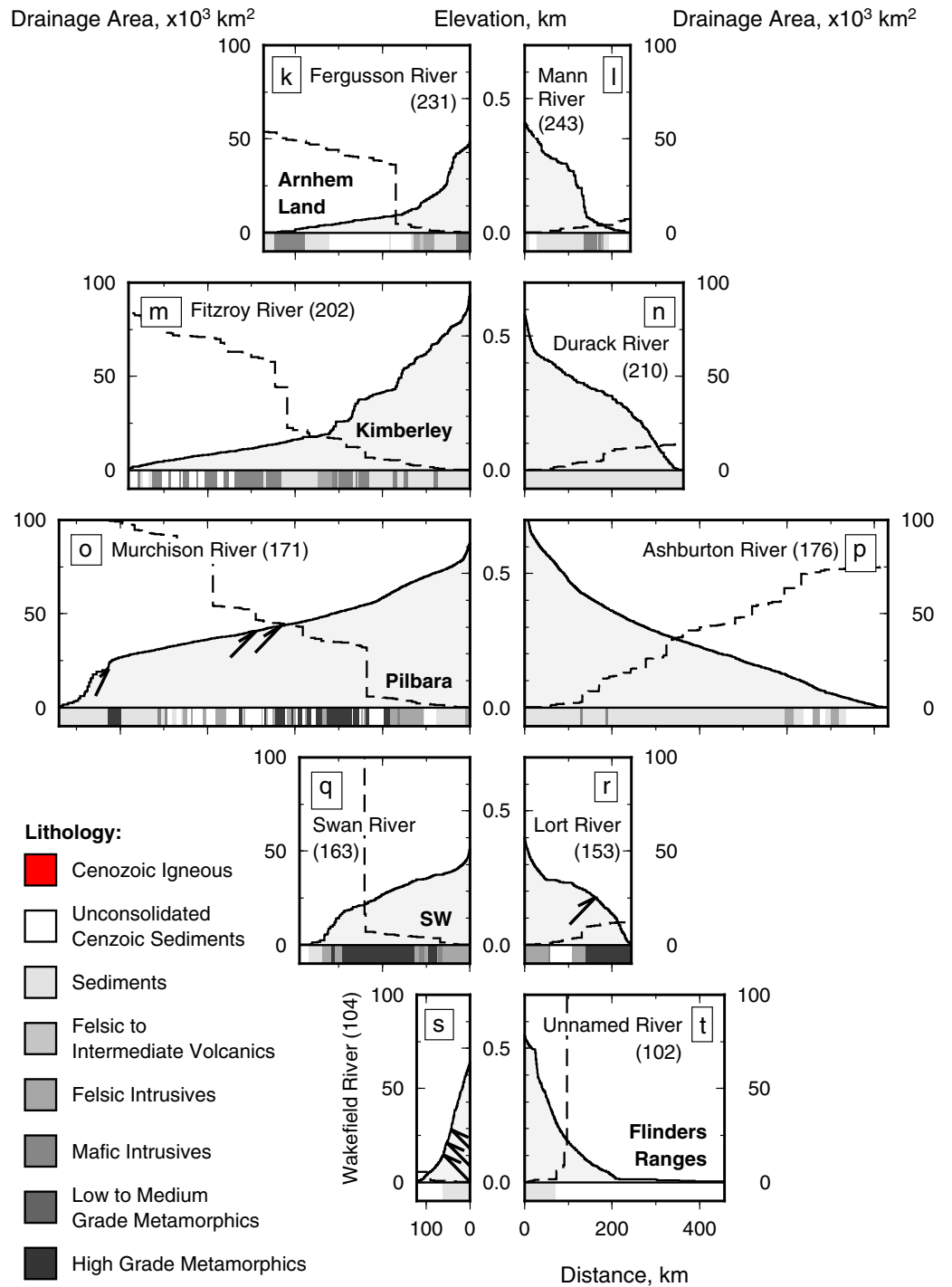


Figure 8. (continued)

#### 4.1. Landscape Response Time

Rivers act as tape recorders of uplift history [Pritchard *et al.*, 2009]. The position of a knickzone along a river can be used to infer the time of an uplift event. However, once a knickzone has propagated to the head of a river, its position can only be used to infer the minimum age of uplift. If  $\kappa = 0$  and  $n = 1$ , the time taken for a knickzone to propagate upstream, which we refer to as Gilbert Time,  $\tau_G$ , is given by

$$\tau_G = \int_0^x \frac{dx}{vA^m} \approx \sum_{i=1}^x \frac{\Delta x_i}{vA_i^m}. \quad (7)$$



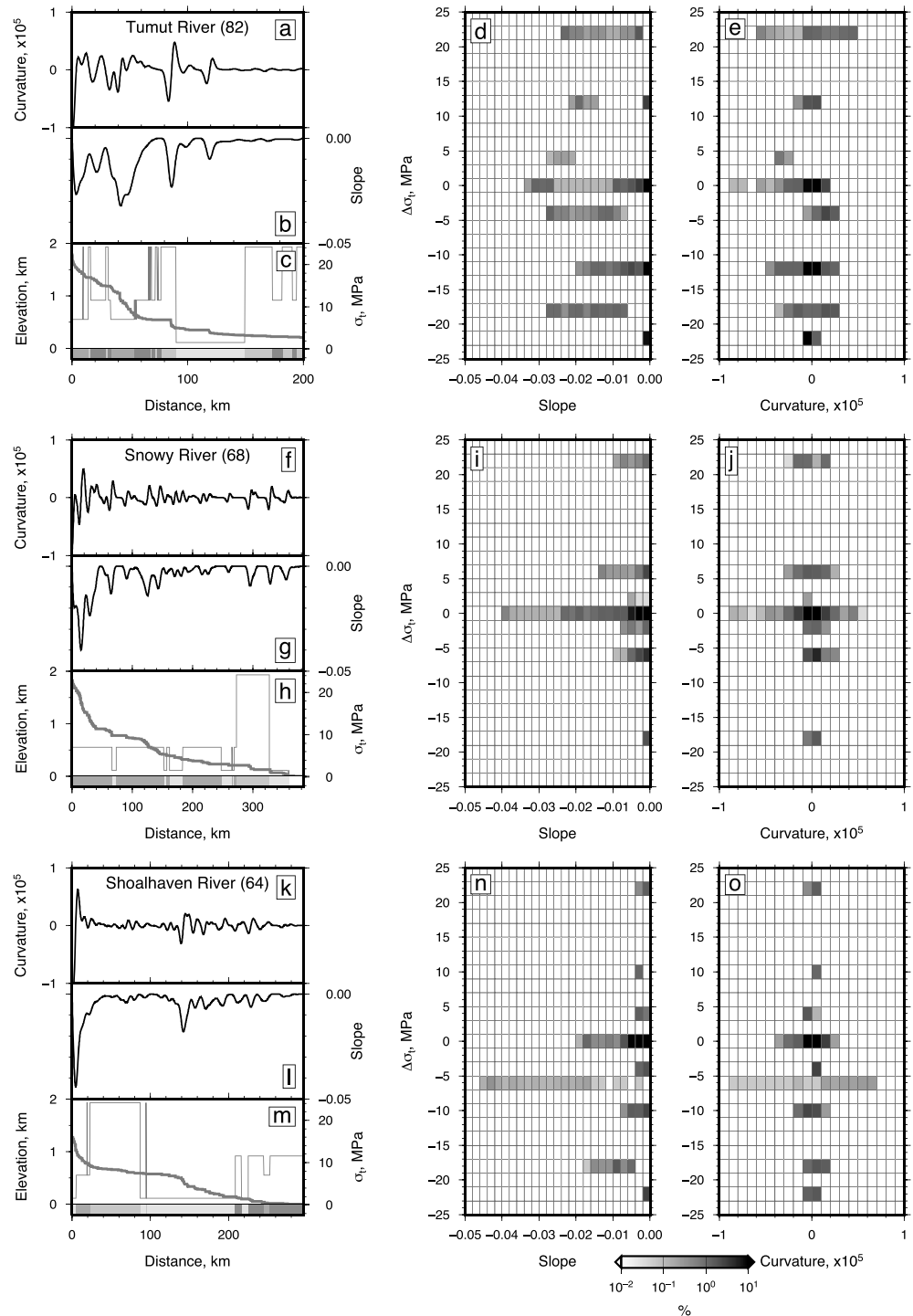


**Figure 9.** Relationship between lithology and longitudinal river profile slope and curvature. (a–c) Curvature, slope, and lithology along Tumut River. In Figure 9c, dark gray line = lithology; thin gray line = estimate of tensile rock strength based on values reported by *Sklar and Dietrich* [2001]. For lithology key, see Figure 8. (d–e) Maximum differences in tensile rock strength within a 6 km moving window along the Tumut River,  $\Delta\sigma_t$ , plotted as function of slope and curvature measured from SRTM topography. Cell shading = percentage of data points which fall within cell. (f–j, k–o) As above, for Snowy River and Shoalhaven River, respectively.

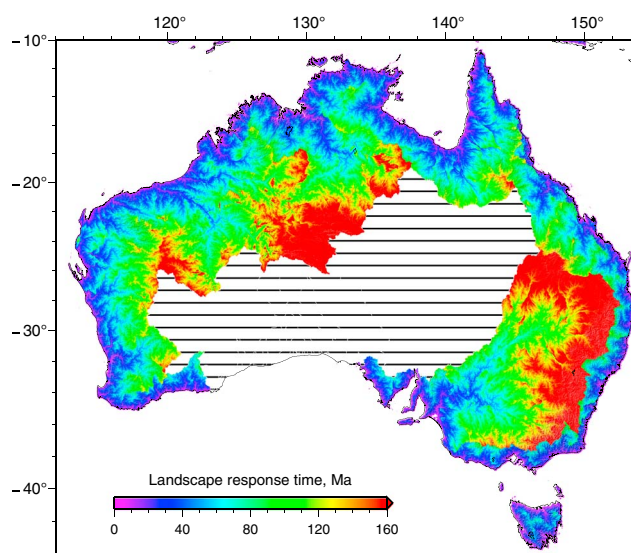


**Figure 10.** Landscape response time,  $\tau_G$ , for knickzones input at coastline calculated using equation (7) with  $m = 0.3$  and  $v = 5.96$  (see section 4.3.2 for parameter justification). Extensive regions of karst and internal drainage (e.g., Eucla Basins and Lake Eyre Basin) have been blanked out. Notice that most drainage basins can record  $\sim 145$ – $100$  Ma uplift events and younger.

Maps of  $\tau_G$  provide a useful estimate of maximum landscape response times (Figure 10). Thus, Australia's drainage network potentially resolves Cretaceous uplift events. Pritchard *et al.* [2009] showed that if  $\kappa = 0$  and if  $A$  can be approximated by  $x^2$ , uplift rate history as a function of time can be determined analytically (Figure 11). This rule-of-thumb analysis suggests that the Eastern Highlands have been affected by several uplift events. The youngest event occurs at 15–20 Ma and is visible at the northern end of the Eastern Highlands. Several distinct uplift events occur between 30 and 50 Ma. The oldest uplift event has a minimum age of 70 Ma, which is at the limit of resolution.

#### 4.2. Erosional Parameters

On the western slopes of the southeastern highlands, paleoriver channels are preserved beneath  $\sim 21$  Ma basalt flows [Young and McDougall, 1993]. The shape and location of these paleoriver channels can be used to calibrate the four erosional constants. Despite a gap of  $> 20$  Ma, Miocene and present-day river profiles have remarkable similar gradients (Figures 12a and 12e). This similarity of form suggests that highland landscape evolution is dominated by headward propagation of knickzones. Two large rivers mapped by Young and McDougall [1993], the Tumut River and Tumbarumba Creek, are suitable for modeling since they have large erosive signals.

Advective erosional parameters were calibrated by forward-modeling river profiles for the last 21 Ma. Paleoriver channels were used as starting solutions. A systematic sweep through  $n$ ,  $m$ , and  $v$  was carried out by allowing the parameters to vary between 0–2, 0–1, and  $10^{-5}$ – $10^3$   $\text{m}^{1-2m} \text{Myr}^{-1}$ , respectively. The misfit between modern observed and modeled river profiles was calculated. Finite-difference schemes that implement the Crank-Nicolson scheme to solve the diffusive term and the upwind scheme to solve the advective term were used to model river profile evolution. The schemes were combined using operator splitting techniques, and the time step was set by the Courant criterion [Press *et al.*, 1992; Roberts and White, 2010].  $A(x)$  was measured directly from digital elevation models. We set  $U = 0$  and  $\kappa = 0.01$ .  $\kappa$  can vary by 7 orders of magnitude without affecting our results (see section 4.3.1). In Figure 12 we show orthogonal slices through the misfit function at  $n = 1$  together with corresponding minimum misfit values of  $v$  and  $m$ . As noted by Roberts and White [2010], there are important trade-offs between all three parameters. The  $\chi^2$  misfit in the direction of trade-off is shown above each panel in Figure 12. Optimal fits are obtained when  $n$  is close to 1 and when  $m$  is 0.3–0.5. Trade-off functions for each river are slightly different. Given that the Tumut River has a larger drainage area and more extensive vertical and lateral paleoriver channel constraints, we have greater confidence in the robustness of this result.

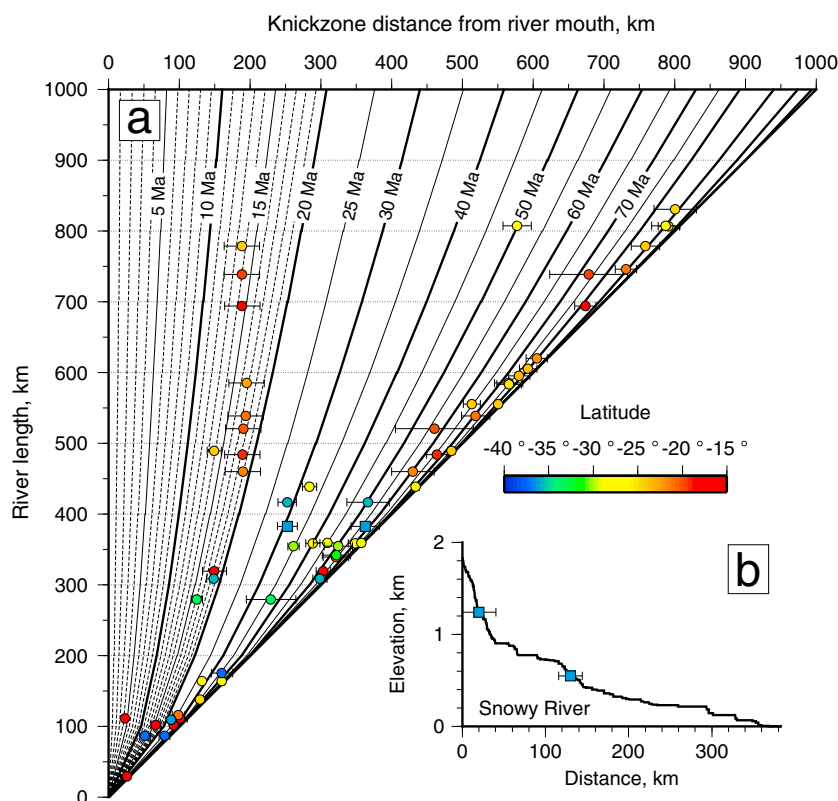


**Figure 11.** Look-up chart for estimating timing of uplift events from knickzone distances along river profiles. Amplitude of event can be estimated from knickzone height. Knickzone retreat rate =  $v x^{2m} \text{ Ma}^{-1}$  [Pritchard et al., 2009; Roberts and White, 2010]. We set  $m = 0.25$  to simplify the dimensions of the solution, therefore  $v = 16.8$  based on the Tumut River trade-off (Figure 12b). (a) River length plotted as a function of knickzone distance from mouth. Numbered lines = uplift event isochrons for a given river length-knickzone distance pair. (b) Squares = knickzone estimate for Snowy River is shown. Circles = knickzone estimates of uplift timing for rivers east of Great Divide; color = latitude at head of river. Notice presence of youthful knickzones between 50 and 15 Ma.

There is reasonable agreement between our results and those of both *Stock and Montgomery* [1999] and *van der Beek and Bishop* [2003] (Figures 12a and 12e). There is a consensus that optimal fits between modern and paleoriver channel profiles are obtained for  $n = 1$ . Their estimates of  $m$  and  $v$  lie along our minimum misfit trade-off, except for the *Stock and Montgomery* [1999] estimate from Tumbarumba Creek. This discrepancy probably arises from their choice of boundary conditions. They applied a constant gradient boundary at the downstream limit of the paleoriver channel, effectively simulating a constant rate of uplift for which there is little direct evidence. *van der Beek and Bishop* [2003] applied five different erosional models to smaller relief paleoriver channel profiles in the headwaters of the Lachlan River. They found that best fits are obtained for a detachment-limited stream power law and for an undercapacity model which includes a term for channel width. Values of  $v$  for the Tumut River are about 4 times smaller for  $m < 4.5$  compared with those obtained for the Colorado River by *Roberts et al.* [2012a]. The implication is that Australian incision rates are slower [e.g., *Bishop and Goldrick*, 1999].

#### 4.3. Uplift Rate as Function of Time

An important objective is to extract uplift rate histories from analysis of longitudinal river profiles. Given the parameter trade-off relationship for the Tumut River, how well can observed river profiles be fitted and how sensitive are extracted uplift histories to parameter variation? The simplest way to analyze this problem is to examine river profiles where it is reasonable to assume that uplift rate varies solely as a function of time (i.e., block uplift with knickzone propagation from the river mouth). Given the variation of dynamic topography across the Eastern Highlands, this assumption is reasonable for eastward-draining rivers where the drainage divide lies within 200 km of the coastline (Figure 6).

Uplift rate histories are obtained using the inverse approach developed by *Roberts and White* [2010]. If  $z(x)$  is known, equations (5) and (6) are solved iteratively to obtain  $U(t)$ . A general optimization algorithm relies on minimizing a trial function,  $H$ , for  $U \geq 0$ . Minimization is achieved by systematically varying uplift rate,



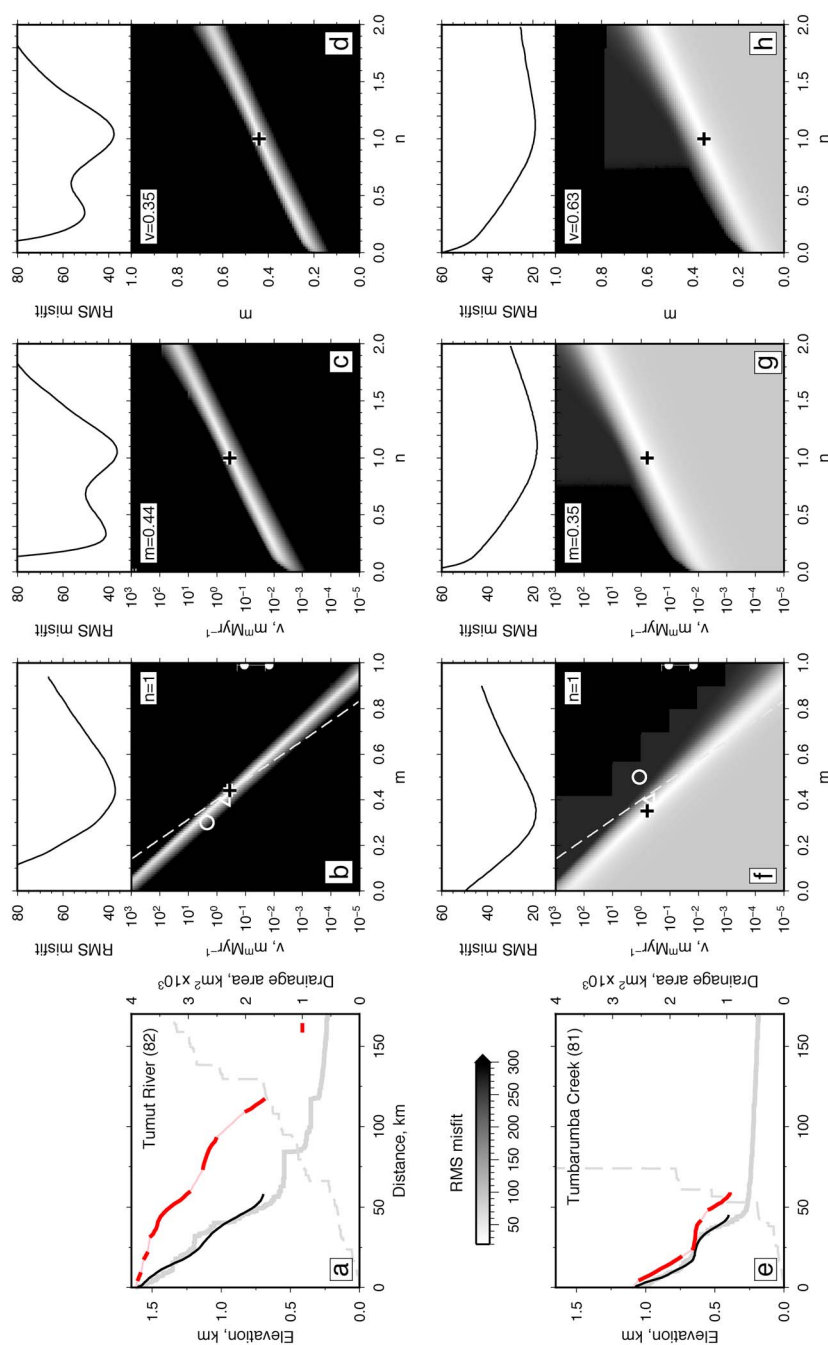


**Figure 12.** Constraints on advective erosional parameters ( $V$ ,  $m$ ,  $n$ ) from paleoriver profiles. (a) Gray line = present-day Tumut River profile; gray dashed line = upstream drainage area; thick red line = mapped 21 Ma sub-saltic paleoriver profile [Young and McDougall, 1993]; thin pink line = modeling starting solution; black line = best fit solution at the black cross in Figures 12b–12d. (b–d) Slices through misfit function (at labeled  $n$ ,  $m$ , and  $V$ ) illustrating how erosional parameters trade-off against each other. At  $n = 1$ ,  $V \approx 2445 \exp(-20m)$  along minimum misfit trade-off. Insets show RMS misfit along the minimum misfit trade-off. Black crosses = location of slices through misfit cube at minimum misfit for  $n = 1$ ; white ring = best fit parameters from Stock and Montgomery [1999]; triangle = best fit parameters for the Lachlan River and Wheeo Creek from van der Beek and Bishop [2003]; white circles = parameters and range used by van der Beek and Braun [1998] and van der Beek and Braun [1999]; dashed white line = minimum misfit trade-off for Colorado River [Roberts et al., 2012a]. (e–h) As above, for Tumbarumba Creek. River locations are shown in Figure 6.

**Table 2.** List of River Modeling Parameters

Variable	Description	Value	Units
$x$	River length from head to mouth		m
$z$	River elevation		m
$\sigma$	Vertical data error	20	m
$x$	Horizontal data sampling	$\sim 4.5\text{--}20 \times 10^3$	m
$x$	$U(x, y, t)$ grid node spacing in $x$ direction	$500 \times 10^3$	m
$y$	$U(x, y, t)$ grid node spacing in $y$ direction	$500 \times 10^3$	m
$A$	Upstream drainage area		m <sup>2</sup>
$t$	Time		Ma
$\tau_G$	Landscape response time		Ma
$t$	Time step	4–10	Ma
$U$	Uplift rate		m Ma <sup>−1</sup>
$E$	Erosion rate		m Ma <sup>−1</sup>
$\kappa$	Diffusive coefficient of erosion	$10^2\text{--}10^4$	m <sup>2</sup> Ma <sup>−1</sup>
$v$	Advective coefficient of erosion	2.11–16.78	m <sup>1–2</sup> Ma <sup>−1</sup>
$m$	Area exponent	0.25–0.35	Dimensionless
$n$	Slope exponent	1–1.05	Dimensionless
$W_1$	$U(t)$ slope weighting coefficient	$10^{-8}\text{--}1$	Dimensionless
$W_2$	$U(t)$ curvature weighting coefficient	$10^{-8}\text{--}1$	Dimensionless
$W_3$	Positivity weighting coefficient	0.001	Dimensionless
$W_4$	$U(x)$ slope weighting coefficient	75	Dimensionless
$W_5$	$U(x)$ curvature weighting coefficient	75	Dimensionless
$W_6$	$U(y)$ slope weighting coefficient	75	Dimensionless
$W_7$	$U(y)$ curvature weighting coefficient	75	Dimensionless
$T$	$U(x, y, t)$ number of temporal nodes	13	Dimensionless
$X \times Y$	$U(x, y, t)$ number of spatial nodes	61	Dimensionless
$\mu$	Model smoothness coefficient	0.25–0.5	Dimensionless

$U_k$ , in order to find the smoothest distribution of  $U$  which yields the smallest misfit between observed and calculated river profiles. The trial function is given by

$$H = \left[ \frac{1}{N} \sum_{i=1}^N \left( \frac{z_i^o - z_i^c}{\sigma_i} \right)^2 \right]^{\frac{1}{2}} + \mu W_1 \left[ \frac{1}{M-1} \sum_{k=2}^M \left( \frac{U_k - U_{k-1}}{\Delta t} \right)^2 \right]^{\frac{1}{2}} + \mu W_2 \left[ \frac{1}{M} \sum_{k=1}^M (U_k'')^2 \right]^{\frac{1}{2}} + \frac{W_3}{M} \sum_{k=1}^M f_1. \quad (8)$$

The first term calculates  $\chi^2$  misfit between observed,  $z_i^o$ , and calculated,  $z_i^c$ , river elevation at all positions,  $N$ , along the river, where the uncertainty in observed elevation is  $\sigma_i$ . The second and third terms control the smoothness of  $U(t)$  by penalizing the slope and curvature of  $U(t)$ , respectively.  $U(t)$  is subdivided into  $M$  number of discrete time steps,  $\Delta t$ .  $U_k''$  denotes the second derivative of  $U(t)$ . The final term on the right-hand side is a positivity constraint, which is applied when  $U < 0$  where  $f_1 = \cosh(U_k) - 1$ .  $W_1$ ,  $W_2$ , and  $W_3$  are weighting coefficients and  $\mu$  controls the model smoothness by covarying  $W_1$  and  $W_2$ . A conjugate gradient technique is used to minimize  $H$  [Press et al., 1992]. In our starting model,  $U(t) = 0$ . Other parameter values are listed in Table 2.

#### 4.3.1. Sensitivity Analysis

The sensitivity of calculated uplift rate histories can be assessed by systematically covarying erosional parameters. We confine our analysis to the Snowy River but the inferences we make apply elsewhere. The headwaters of the Snowy River are located on the other side of the drainage divide from the Tumut River (Figure 6). During optimization, the mean residual misfit,  $\chi^2$ , between the observed and calculated river profile decreased from 31.5 to 1.4 (Figure 13a). Model smoothness and data misfit trade-off against each other and it is important to determine the amount of model smoothness which yields a good fit [Parker, 1994]. Figures 13b–13h summarizes the effect that varying the regularization parameter,  $\mu$ , has upon data misfit,  $\chi^2$ , and model roughness,  $\|m\|$ , where

$$\|m\| = \left[ \frac{1}{M-1} \sum_{k=2}^M \left( \frac{U_k - U_{k-1}}{\Delta t} \right)^2 \right]^{\frac{1}{2}} + \left[ \frac{1}{M} \sum_{k=1}^M (U_k'')^2 \right]^{\frac{1}{2}}. \quad (9)$$

Models which best satisfy Parker's [1994] criteria are located where  $\mu \approx 0.25$ . Smoother models do not resolve discrete events and rougher models yield complex uplift rate histories of questionable geologic significance.

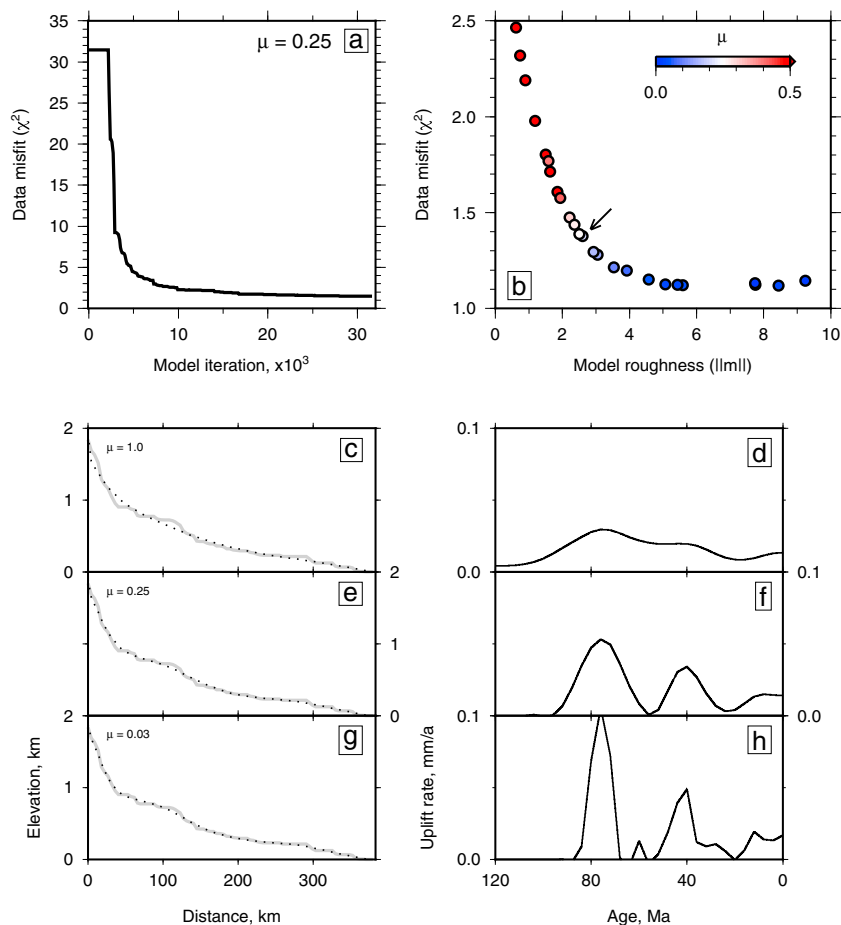


**Figure 13.**  $U(t)$  for Snowy River (68 in Figure 6). (a)  $\chi^2$  data misfit as a function of model iteration for model smoothing parameter,  $\mu = 0.25$ . (b)  $\chi^2$  data misfit as a function of model roughness,  $\|m\|$ , colored by  $\mu$ . Arrow points to smoothest model at lowest misfit used for all 1-D inversions. (c) Gray line = observed river profile; dotted line = calculated river profiles for labeled  $\mu$ . (d) Uplift rate history for  $\mu$  value in Figure 13c. (e–f and g–h) As for Figures 13c–13d.

Variations in erosional parameters  $v$ ,  $m$ , and  $n$  give rise to large differences in both calculated uplift histories and residual misfit. In Figures 14a–14g, we show the result of covarying  $m$  and  $v$  for  $n = 1$  according to the Tumut River minimum misfit trade-off (Figure 12b). Since this trade-off relationship was established in a region with a small upstream drainage area, a decrease in  $m$  produces older uplift ages and vice versa. The sensitivity of the calculated uplift history is shown in Figures 14d and 14e. Thus, varying  $m$  from 0.3 to 0.2 while covarying  $v$  appropriately shifts uplift events back in time.

Covarying all three parameters  $v$ ,  $m$ , and  $n$  along the minimum misfit for the Tumut River shows that the best fit occurs for  $n \approx 1$  (Figures 14h–14n). Since river slopes are less than  $45^\circ$ , a decrease in  $n$  produces faster erosion rates and vice versa.  $\kappa$  can vary by many orders of magnitude without affecting our results (Figures 14o–14u). More importantly, upstream drainage area can vary by  $\pm 30\%$  and only shift peak uplift rate by small amounts (Figures 14v–14ab). This insensitivity to substantial variations in upstream drainage area suggests that putative river capture events have a modest effect upon our principal results. Furthermore, uncertainties in estimating upstream drainage area from SRTM data should not affect the robustness of our results [Hancock et al., 2006]. In Figures 14ac–14ai, we explore the consequences of changing river length. Along the east coastline, the shelf break generally lies within 50 km of the coast and estuaries extend less than 20 km inland. Changing river lengths by these amounts can shift peak uplift rates by up to 10 Myr.

#### 4.3.2. Independent Constraints

Changes in  $v$ ,  $m$ , and  $n$  can yield differing uplift rate histories. It is important to identify the combinations of erosional parameters that yield uplift histories that honor independent geologic constraints. We selected four rivers from the Eastern Highlands that have independently constrained uplift histories. The head of

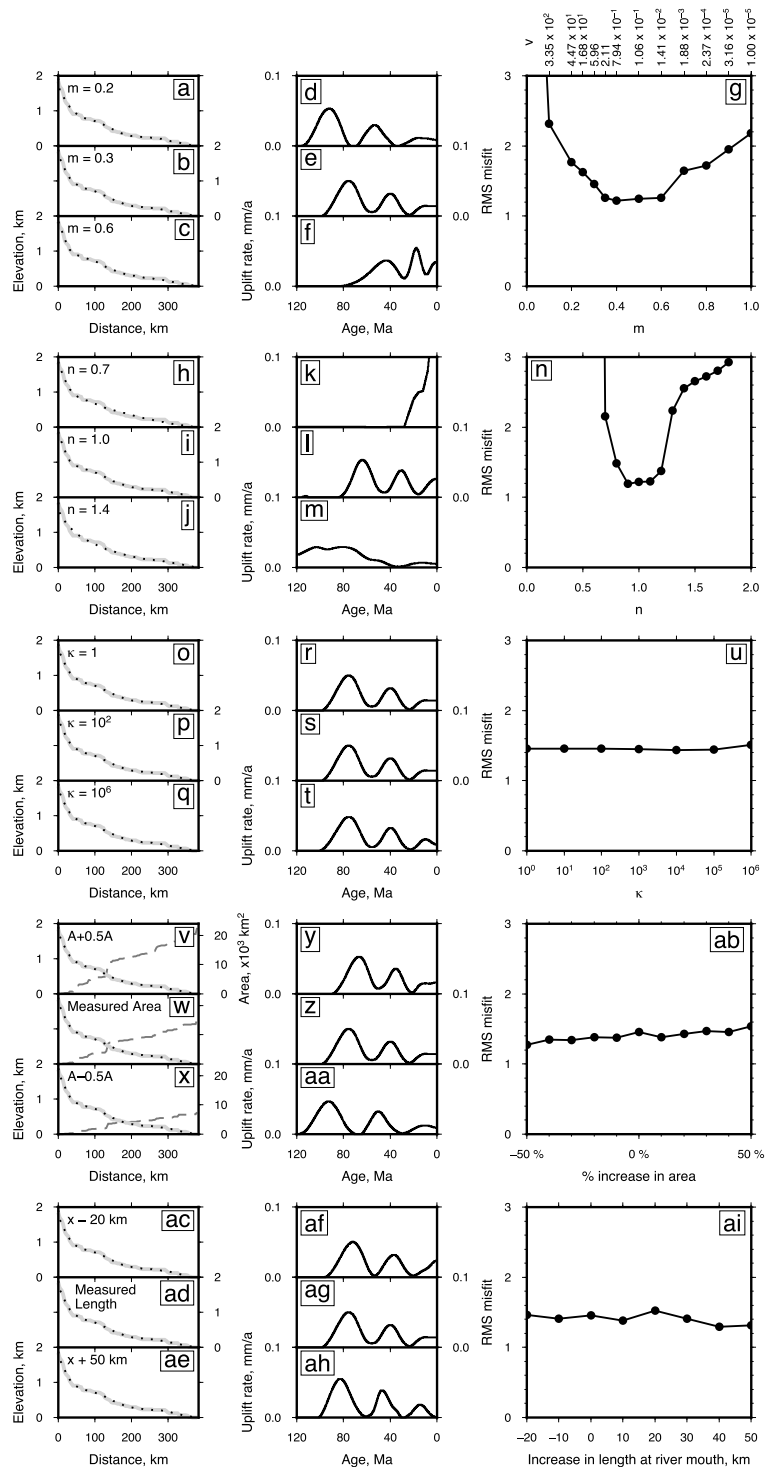


**Figure 14.** Effect of erosional parameter variation on calculated 1-D uplift histories and residual misfit between theoretical and observed Snowy River profiles. (a–g) Systematically covaried  $m$  and  $v$  at  $n = 1$  along the Tumut River trade-off to determine which values yield smallest residual misfit (Figure 12). (a–c) show how different values of  $m$  and  $v$  effect the shapes of theoretic river profiles. Gray line = observed river profiles; dotted line = theoretic river profile. Values of  $m$  are shown in top right, corresponding  $v$  values are shown in Figure 14g. (d–f) uplift rate histories for best-fitting adjacent theoretic river profiles. (g) minimum misfit as a function of covaried  $m$  and  $v$ . Notice the value of  $m = 0.3 \pm 0.05$ , which best satisfy observational constraints in Figures 15–17, is within error of the global minimum around  $m = 0.4$ . (h–n) Systematic variation of  $n$  with  $m$  and  $v$  selected for each  $n$  at minimum misfit values from Tumut River parameter sweep (Figure 12). Notice global minimum is centered around  $n = 1$ . (o–u) Variation of  $\kappa$  over 6 orders of magnitude showing negligible change in uplift history. (v–ab) Variation of upstream area by 0.5A–1.5A. (ac–ai) Variation in river length by –20 to +50 km applied to the river mouth. At increased river lengths, drainage area at river mouth was kept constant.





each of these rivers lies within 200 km of the coast (Figure 15). We also identified rivers, which drain southern and western Australia, where uplift histories can be independently constrained (Figures 16 and 17).

Uplifted marine strata provide an important constraint for maximum uplift age (e.g., Northern Queensland; Figures 15q and 15w). Bands of marine strata along the coastal plain may arise from the interplay between knickzone migration and eustasy (e.g., west coast of Australia; Figures 1a, 17h, and 17l). If uplift varies only as a function of time, then knickzone initiation should be the same age as, or younger than, the onset of rifting at a margin. Fault architecture within the Gippsland Basin constrains the age of rifting, which culminates in Tasman Sea floor spreading at 80–100 Ma [Rahmanian et al., 1990; Lowry and Longley, 1991; Norvick and Smith, 2001]. Similar constraints along the southern and western margin imply that rifting occurred between 165 and 140 Ma and 160 and 133 Ma, respectively [Totterdell et al., 2003; Longley et al., 2002]. The vertical extent of basalt flows constrains the minimum cumulative uplift at the time of basalt eruption (Figures 15e, 15k, 15q, and 15w). Incised basalt flows also provide spot estimates of paleoriver channel elevation (Figures 15b and 15h).

By varying  $n$ ,  $m$ , and  $v$  along a minimum misfit relationship for the Tumut River, independent constraints are most closely honored when  $1 \leq n \leq 1.05$ ,  $0.25 \leq m \leq 0.35$ , and  $2.11 \leq v \leq 16.78$  (Figures 15–16). The optimal values are  $n = 1$ ,  $m = 0.3$ , and  $v = 5.96 \text{ m}^{0.4} \text{ Myr}^{-1}$ . These values result in a residual misfit that is close to the global minimum for the Tumut River (Figures 12b and 14g). A formal goodness of fit is one of several considerations when selecting geologically valid erosional parameters.

In this way, we have attempted to honor all maximum age constraints and all minimum cumulative uplift constraints. For the Shoalhaven River, however, we underpredict cumulative uplift by  $\sim 200 \text{ m}$  at 30 Ma while satisfying the paleoelevation of 30 Ma basaltic flows preserved along the rim of the Shoalhaven River gorge (Figures 15h and 15k) [Nott et al., 1996]. This discrepancy probably arises because of the 60 km separation between the river and the cumulative uplift constraints and/or because of uncertainties in K–Ar dating of the basalts [Young and McDougall, 1982]. Our inability to match all constraints from the Eucla Basin stems from the spatial variation of uplift and from  $\sim 70 \text{ m}$  glacio-eustatic sea level variations, which modulate the uplift signal (Figure 16) [Hou et al., 2008]. On the west coast, our cumulative uplift predictions are within 50 m of the independent constraints, which is within the amplitude of glacio-eustatic sea-level variation (Figure 17). Independent uplift constraints across the continent are honored by a single set of erosional parameters, which implies that erosion is not sensitive to climate variation.

### 4.3.3. Implications

Inverting for uplift rate as a function of time,  $U(t)$ , yields insights into the regional uplift of Australia. Drainage of the Eastern Highlands is consistent with a two phase uplift history (Figure 15). The older phase of uplift occurs between 120 and 80 Ma and has a maximum uplift rate of 0.05 mm per year. It roughly coincides with the age of rifting. A second phase of uplift occurs between 70 and 20 Ma and has a maximum uplift rate of 0.04 mm per year. It coincides with the age of intraplate Cenozoic volcanism. In areas where we have constraints on uplift from basalt flows, uplift immediately precedes volcanism. A similar relationship is observed for the Eucla Basin (Figures 16e and 16h).

**Figure 15.**  $U(t)$  inverse modeling of east coast rivers. (a) Solid gray line = river profile; dashed line = upstream area; black dotted line = best fit synthetic river profile. Inverted triangle = base of incised basalt flow overlying fluvial sediment [Wellman, 1979b]. (b) Black line and gray band = mean and  $1\sigma$  theoretic river profile derived from uplift rate in Figure 15d. Inverted triangle = elevation of incised basalt flow. (c) Normalized probability density function of Cenozoic volcanism ages within 150 km of river [Vasconcelos et al., 2008];  $n$  = number of dated samples; black triangle = age of oldest adjacent Tasman Sea magnetic anomaly [Gaina et al., 1998]. (d) Calculated uplift rate history; back line and gray band = mean and  $1\sigma$  uncertainty from 50 Monte Carlo inversions varying erosion parameters  $m$  and  $v$  along the Tumut River minimum misfit trade-off at  $n = 1$  for  $0.25 \leq m \leq 0.35$  and randomly varying  $n$  and  $v$  for  $1.0 \leq n \leq 1.05$  and  $2 \times 10^2 \leq v \leq 7 \times 10^2$ . (e) Cumulative uplift history,  $\int_0^t U(t)dt$ , and independent uplift constraints; circles = age of rifting in Gippsland Basin [Rahmanian et al., 1990; Lowry and Longley, 1991; Norvick and Smith, 2001]. Hashed polygon = minimum uplift constraints from basalt flows [Wellman, 1979b]. Inverted triangle with error bars = palaeoelevation of creeks [Holdgate et al., 2008]. Dashed and dotted line = AFT cooling trend which fits (U-Th)/He ages within  $1\sigma$  error from Persano et al. [2005] scaled to cumulative uplift (sample 00-CP-03). (f) Sedimentary flux and denudation rate as a function of time. Solid line and grey band = calculated mean sediment flux and  $1\sigma$  uncertainty. Dashed line = denudation rate from AFT analysis [Kohn et al., 2005]; stippled boxes = siliciclastic sediment flux in the Gippsland Basin [Weber et al., 2004]. Inset shows geological units: white = terrestrial; gray = marine; black = unconformity; v letters = volcanoclastic sediment; stippled = siliciclastic sediment; rectangles = carbonate sediment [Bernecker and Partridge, 2005]. (g–l) Shoalhaven River. Basalt flows in Figures 15g and 15k from Nott et al. [1996] and Young and McDougall [1982, 1985]; thermochronology in Figure 15k from Persano et al. [2005] (sample 99-OZ-12). (m–r) MacLeay River. Basalts and youngest marine deposits in Figure 15q from Wellman [1987] and Langford et al. [1995] (Figure 1a). (s–x) Herbert River. Age of Coral Sea in Figure 15u from Gaina et al. [1999]. In Figure 15w, dashed and dotted line = AFT cooling trend [Marshall et al., 2000]; vertical extent of basalt flows from Ollier [1982]; and youngest marine deposits from Langford et al. [1995] (Figure 1a). River locations are shown in Figure 6.

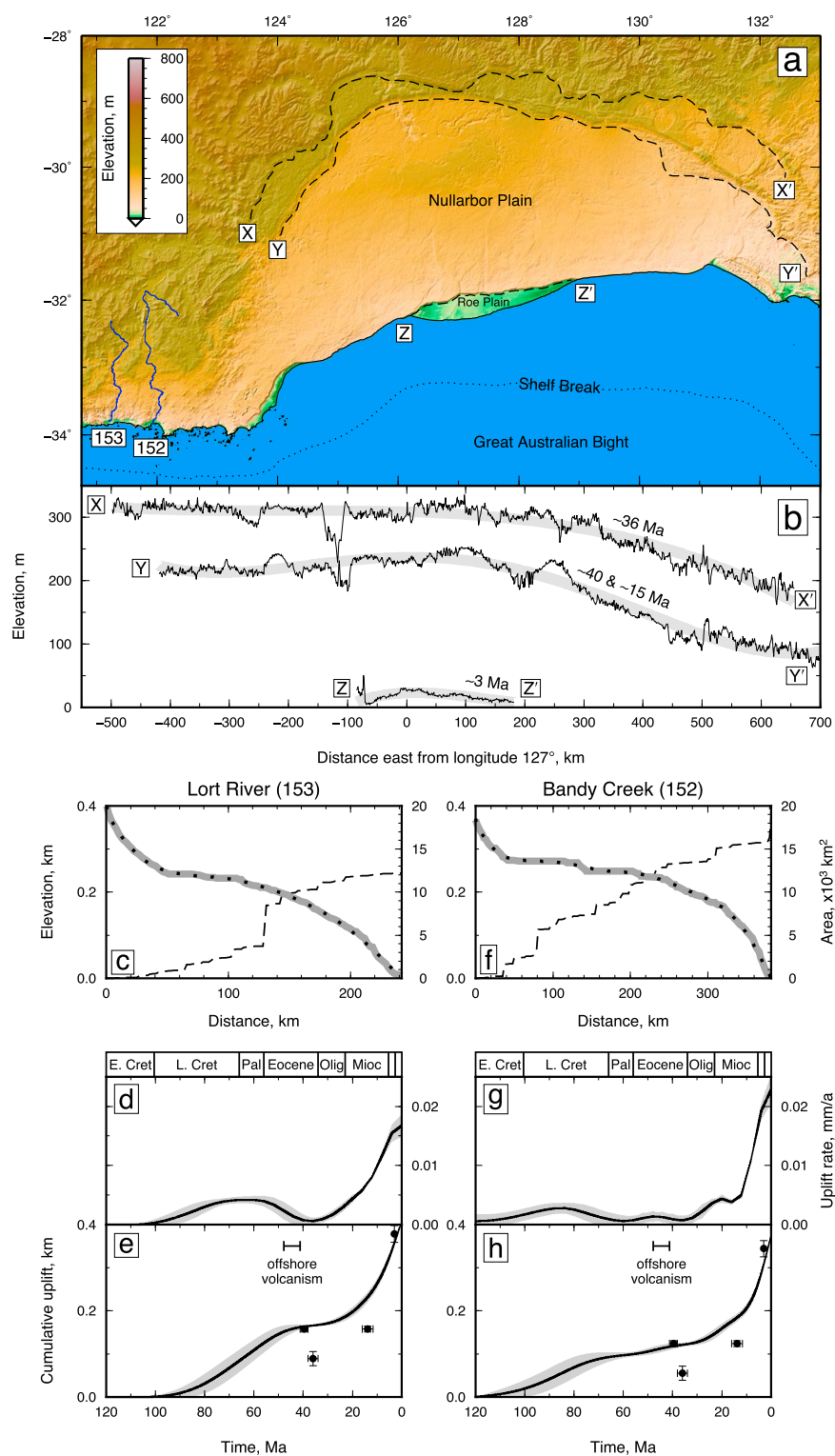


**Figure 16.** Constraints on uplift derived from Eucla Basin paleoshorelines and  $U(t)$  inverse modeling of adjacent rivers. (a) Topographic map of the Eucla Basin. Blue lines = closest rivers to Eucla Basin which drain into Southern Ocean; dashed lines = transects along paleoshorelines after Sandiford [2007]; dotted line = shelf break position. (b) Black lines = topography as a function of distance along paleoshorelines extracted from SRTM data set, centered at 127°E, locations in Figure 16a; gray band = long-wavelength topography; age of palaeoshorelines from Hou et al. [2008]. Notice that uplift varies on wavelengths > 2000 km. (c–h) Symbols as in Figure 15. Filled circles in Figures 16e and 16h = cumulative uplift constraints from elevation of palaeoshorelines west of 128°E, shown in Figures 16a–16b.

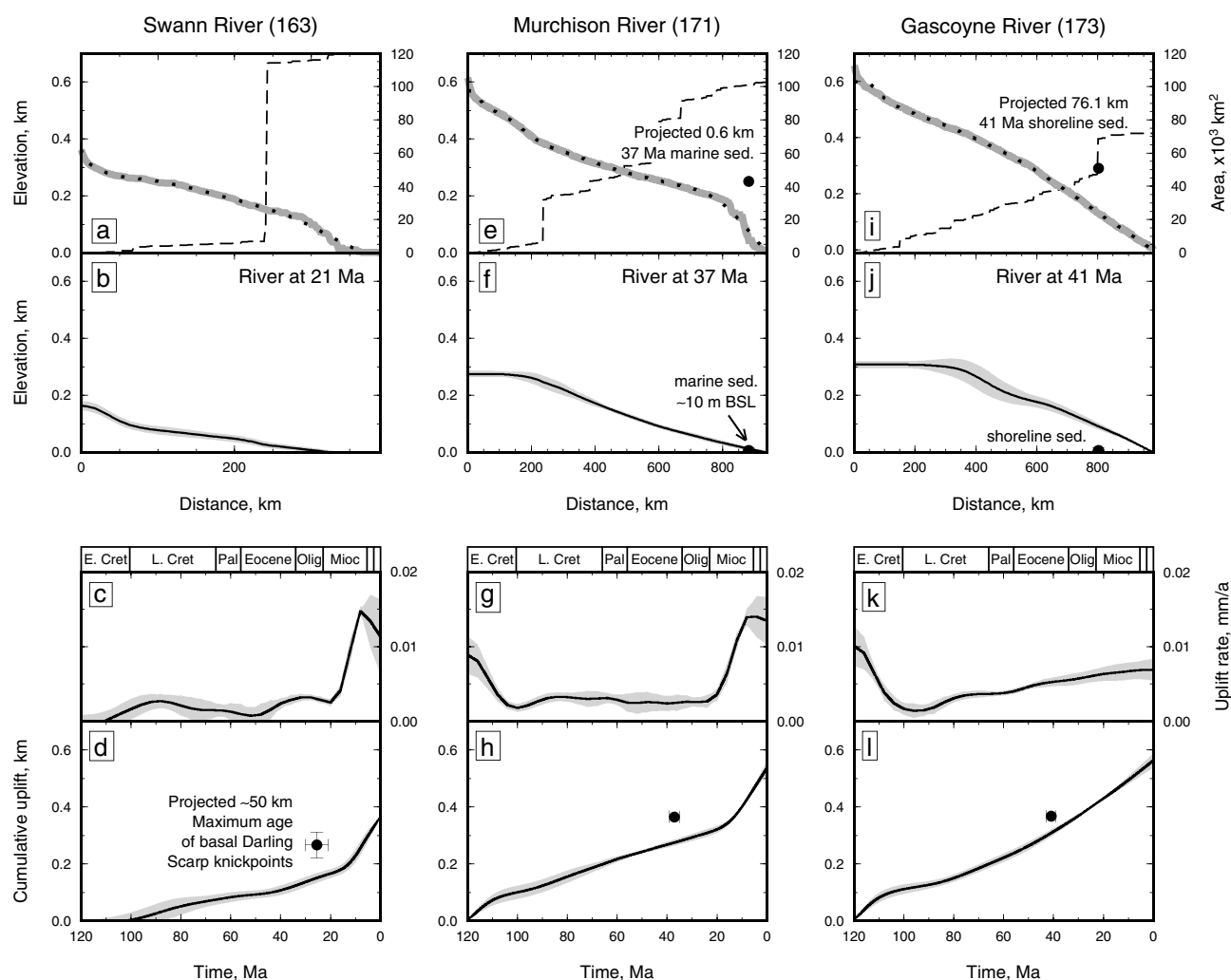


**Figure 17.**  $U(t)$  inverse modeling of rivers draining the southern Pilbara and western plateau. For locations, see Figure 6. Panels same as in Figure 15. In Figure 17d, maximum age of Darling Scarp initiation based on cosmogenic  $^{10}\text{Be}$  analysis by Jakica et al. [2011]. In Figures 17e–17f, locations and elevations of shoreline and marine strata from Haig and Mory [2003].

A multiple uplift history of the southeastern highlands is reflected in the stratigraphic record of the Gippsland Basin (Figure 15f). Both phases of uplift are associated with basin-wide unconformities [Bernecker and Partridge, 2005]. The second phase of uplift is associated with development of onshore and offshore low-angle unconformities across southeastern Australia and with major channel incision in the Gippsland Basin between 44 and 40 Ma [Johnstone et al., 2001; Holdgate et al., 2003].

Sedimentary flux can be predicted from river profile evolution (e.g., Figure 15f). In the Gippsland Basin, onset of carbonate sedimentation corresponds with a decrease in sediment flux at  $\sim 30$  Ma. The maximum clastic flux estimated from isopach maps roughly coincides with peak uplift rate but does not agree with the predicted sediment flux. There is some correspondence between the maximum rate of uplift and denudation predicted from thermochronologic analyses (Figures 15q–15r) [Kohn et al., 2005].

#### 4.4. Uplift as Function of Time and Space

Having established the values of erosional parameters from one-dimensional river profile inversion, we can now address the more general problem and attempt to constrain uplift rate history as a function of both time and space by jointly inverting 254 river profiles from across Australia [Roberts et al., 2012a] (Figure 6 and Table A1). First, we define an  $X \times Y \times T$  grid where  $X$ ,  $Y$ , and  $T$  are spatial and temporal vertices, respectively (Table 2). We set the grid spacing,  $\Delta x = \Delta y = 500$  km, and invert for a period lasting 120 Ma with a time step of  $\Delta t = 10$  Myr. Optimal values of  $n = 1$ ,  $m = 0.3$ , and  $v = 5.96 \text{ m}^{0.4} \text{ Myr}^{-1}$ , determined from 1-D river profile analysis, are used. Figure 18 shows an analysis of the model null space by calculating,  $\tau_G$

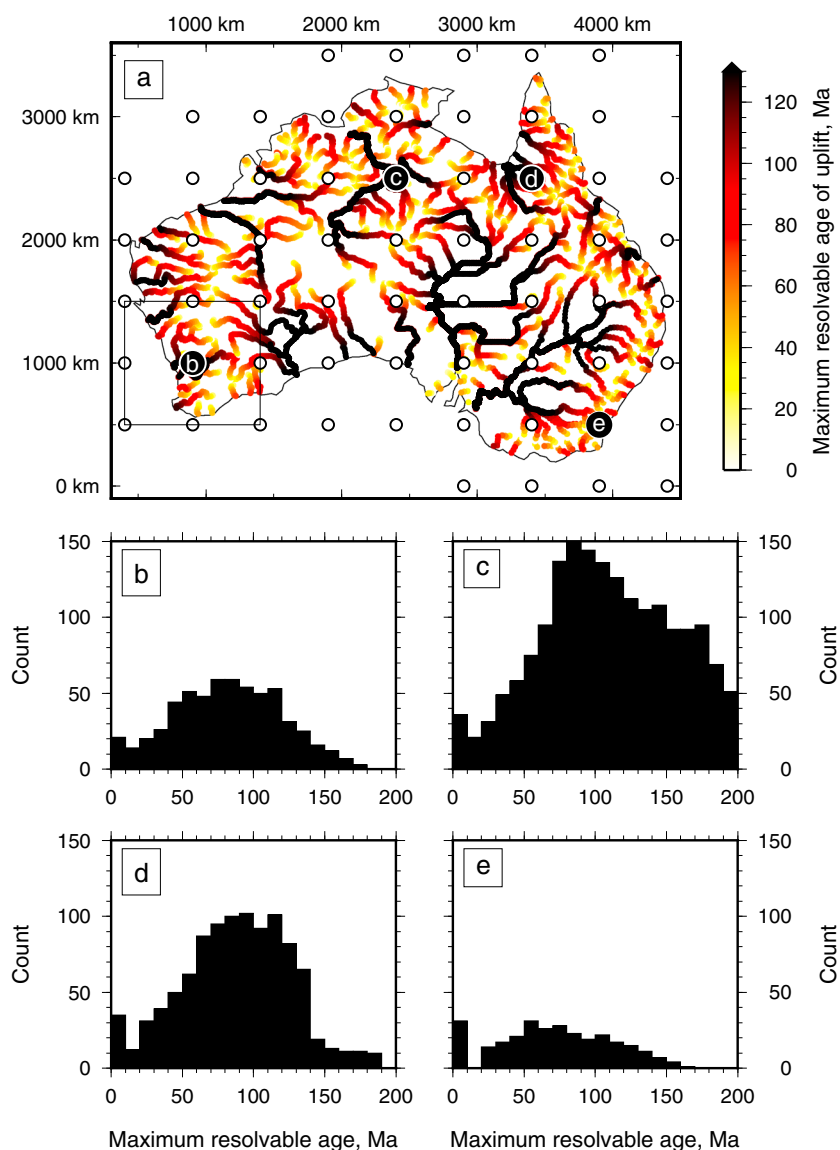


**Figure 18.** Spatial distribution of the maximum resolvable age of uplift input at all points along 254 rivers. (a) Colored circles =  $\tau_G$  calculated for each point along individual rivers in the upstream direction. White circles =  $U(x, y, t)$  inversion grid vertices. (b) Histogram of maximum resolvable ages within the four adjacent boxes to vertex “b” in Figure 18a. (c–e) As for Figure 18b.

along each river in the downstream direction (equation (7)). The result shows the maximum resolvable age of knickzones input at any point along the river. Oldest ages are at the river mouth and decrease toward the head. If the model is not damped, then each vertex is only sensitive to uplift ages younger than the oldest  $\tau_G$  within the four surrounding cells. Figures 18b–18e shows histograms of these ages for four vertices. Each vertex is sensitive to uplift ages back to at least 120 Ma. By damping the model, maximum resolvable age increases.

We set  $U(x, y, t) = 0$  as the starting condition and seek the smoothest uplift history which minimizes the misfit between observed and calculated river profiles. An additional four terms are included in the trial function of equation (8), which minimize slope and curvature in both the  $X$  and  $Y$  directions. At each model iteration, uplift rate is bilinearly interpolated between vertices to obtain values along each river profile. During optimization, the residual misfit between observed and calculated river profiles,  $\chi^2$ , decreases from 8.9 to 2.4. An optimal smoothing value is obtained by running multiple inverse models as before (Figure 13b). Good fits were obtained for many different river profiles (e.g., Figures 19e and 19f). The largest residual misfits occur for river profiles which drain the southeastern highlands. These discrepancies are a consequence of the coarse grid spacing, which cannot resolve short-frequency topographic variations.



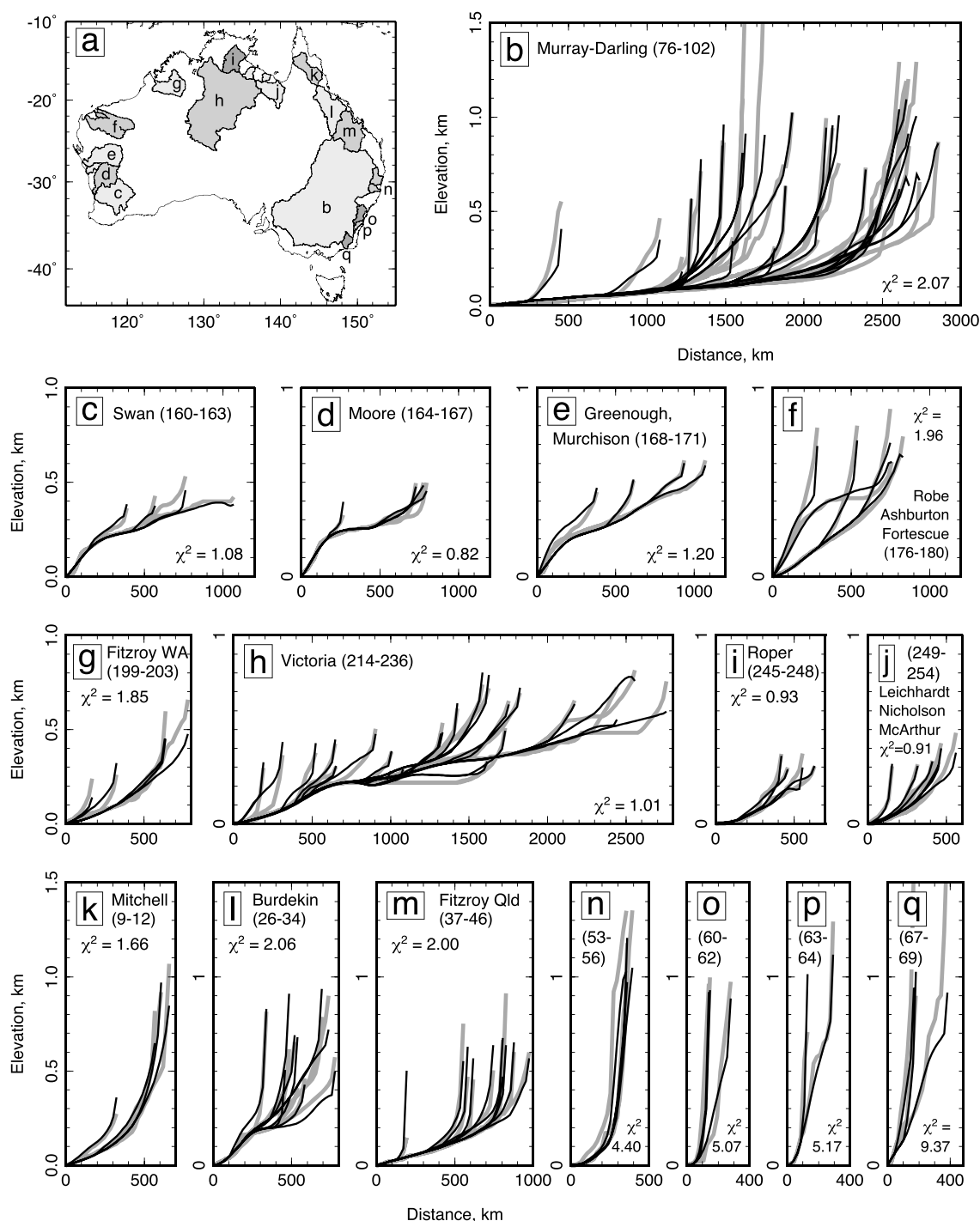


**Figure 19.** Comparison between observed and calculated river profiles from joint inversion of 254 rivers (Figure 20). (a) Distribution of drainage basins corresponding to catchments shown in Figures 19b–19q. (b–q) Gray lines = observed river profiles; numbers in brackets = river numbers in Figure 6 and cataloged in Appendix A; black lines = calculated river profiles. Notice excellent fits to rivers draining western plateau and poorer fits along the Eastern Highlands. This discrepancy arises due to the coarse vertex spacing (500 km) which cannot capture shorter wavelength elevation variations along the southeastern highlands.

The resultant cumulative uplift history,  $\int_0^t U(x, y, t)dt$ , is shown in Figure 20. It is important to emphasize that a priori assumptions about the spatial and temporal pattern of uplift were not included. Instead, the inversion algorithm produces the smoothest uplift history which best fits all 254 river profiles. A comparison between the final cumulative uplift and a surface envelope fitted to drainage divides shows that we can accurately resolve most major topographic elements, despite the coarse grid spacing. The resultant uplift

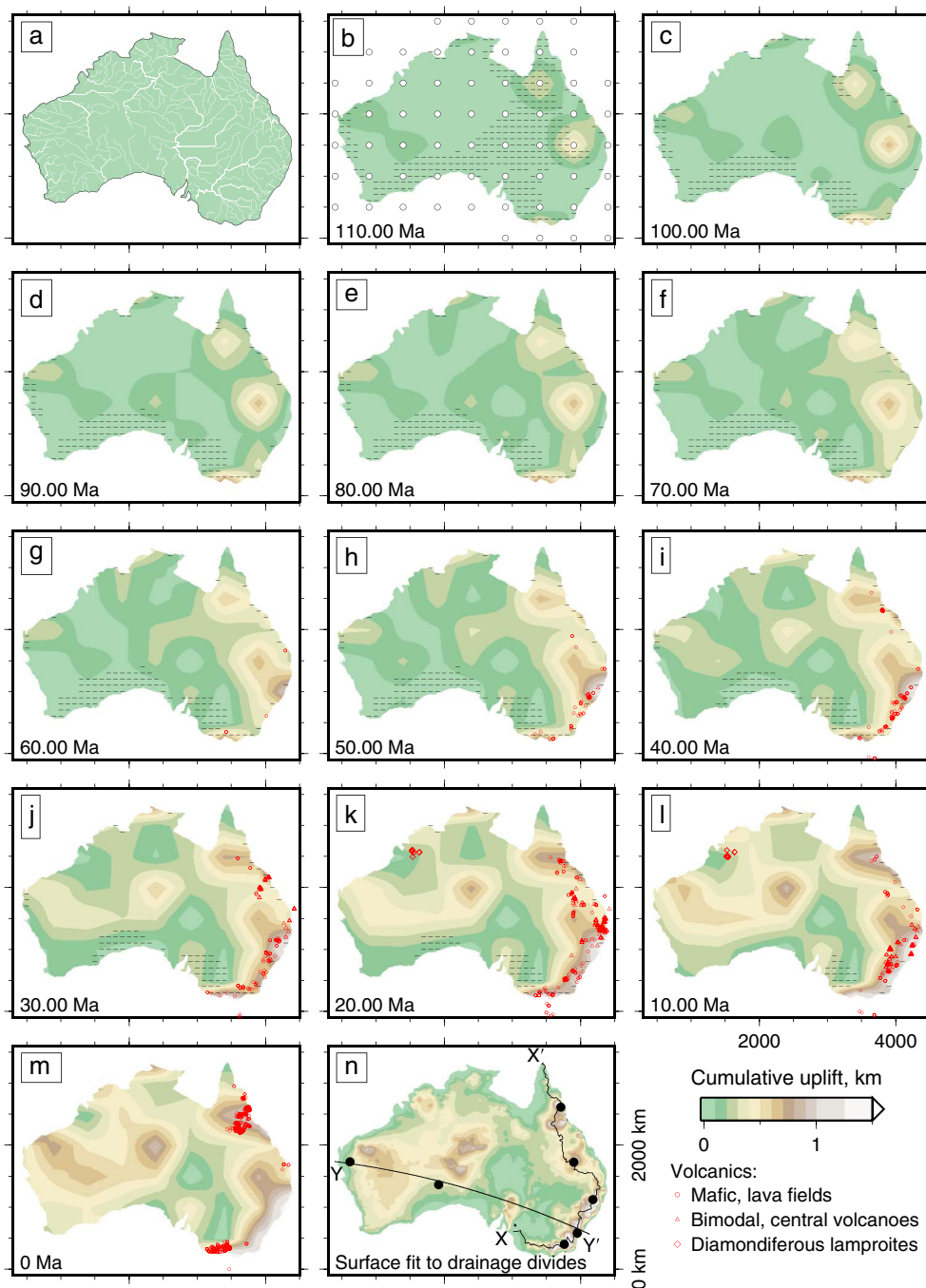


**Figure 20.** Cumulative uplift history,  $\int_0^t U(x, y, t) dt$ , from joint inversion of 254 rivers. (a) Starting condition; white lines = input rivers (Figure 6). (b–m) Growth of topography shown at 10 Ma intervals; white circles = 500 km spaced vertices at which uplift rate is varied during inversion; black dashed lines = distribution of marine and coastal strata  $\leq$  labeled age; red symbols = location of volcanism erupted in preceding 10 Ma. (n) Surface fit to present-day drainage divides for comparison with final modeled cumulative uplift shown in Figure 20m; black lines = location of transects shown in Figures 21–22; black circles = location of independent uplift constraints shown in Figures 21–22.

history also honors the distribution of coastal and marine strata. The first time step is at 110 Ma and shows uplift commencing along the northeast margin. The minor discrepancy at 110 Ma between predicted topography and distribution of marine strata west of the Atherton Tablelands arises from a lack of spatial nodes on the drainage divide. In general, our results suggest that the Eastern Highlands were uplifted before central and western Australia.

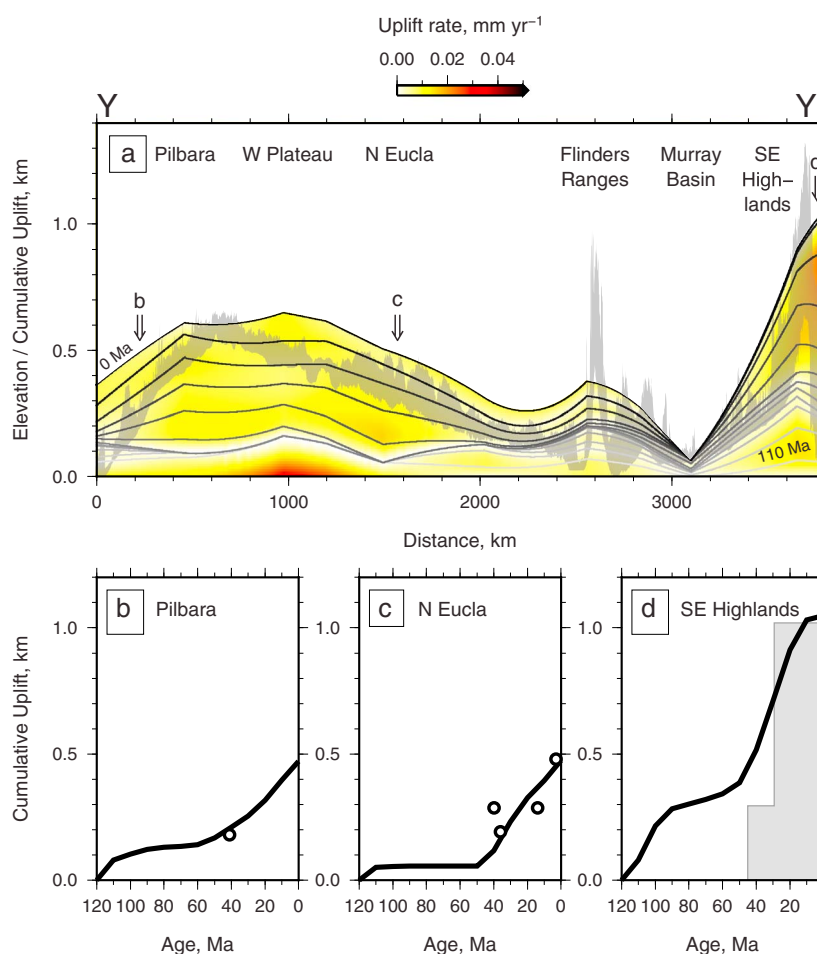


**Figure 21.** Cumulative uplift history from joint inversion of rivers along a northwest-southeast transect. Transect location shown in Figure 20n. (a) Gray band = 100 km wide topographic swath along transect; gray to black solid lines = 10 Ma isochrons from cumulative uplift history in Figures 20b–20m; color grid = uplift rate at cumulative uplift isochrons; labels b–d = location of cumulative uplift points with independent uplift constraints. (b) Black line = cumulative uplift history from 2-D river inversion; white circle = constraint on cumulative uplift since 41 Ma from marine deposits [Haig and Mory, 2003]. (c) Same as Figure 21b with uplift constraints from Figure 16. (d) Same as Figure 21b; gray hatching = minimum age uplift constraints from basalt flow elevations [Young and McDougall, 1982, 1985].

In Figures 21–22, we compare the growth of topography along different swaths. Comparisons with independent uplift estimates from the western Plateau and from the northern Eucla Basin demonstrate that temporal and spatial variation in uplift rate histories produces a better fit than that obtained from  $U(t)$  models (compare Figure 21b with 17h, and Figure 21c with 16e and 16h). These results suggest that our estimates of uplift of the Western Plateau since ~50 Ma are robust. The pattern of uplift shows diachroneity from north to south. In the Flinders Ranges, increased uplift rates since ~30 Ma are older than the inferred 10–5 Ma onset of the Australian compressional stress field, which is considered responsible for fault-controlled uplift in these ranges [Sandiford *et al.*, 2004]. This result suggests that there might have been dynamic uplift preceding fault-related uplift.

Regional uplift of the Eastern Highlands appears to vary through space and time. The northern highlands were rapidly uplifted between 120 and 100 Ma and were subsequently uplifted at a constant rate. The southeastern highlands, including New England, were uplifted in two phases. Uplift between 120 and 80 Ma was regionally distributed with decreasing amplitude toward the north. Uplift between 80 and 10 Ma becomes progressively younger from north to south and corresponds to the duration of volcanic activity (Figure 5). Our results are consistent with many independent uplift constraints (Figures 22b–22e).

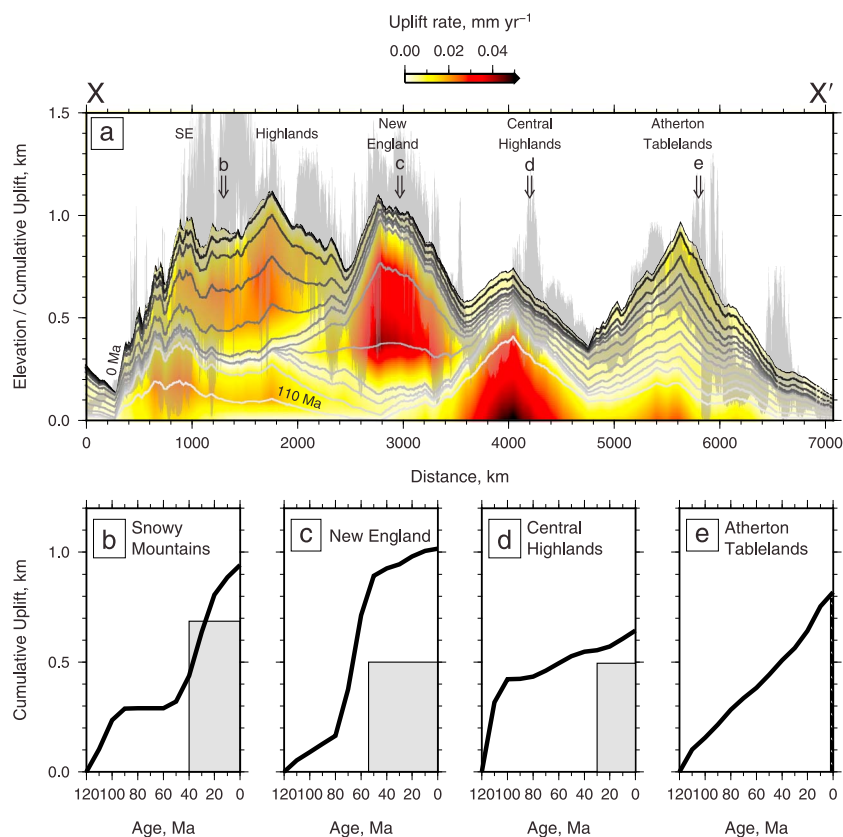


**Figure 22.** Cumulative uplift history from joint inversion of rivers along the crest of the Eastern Highlands. Transect location shown in Figure 20n. Symbols as in Figure 21. Minimum cumulative uplift constraints from paleobasalt flows as in Figure 15 and in the Central Highlands from Young and Wray [2000].

## 5. Discussion

Continent-wide analysis of drainage patterns suggests that present-day topography was primarily generated during the Cenozoic Era. Admittance studies and tomographic models suggest that the Eastern Highlands are dynamically supported by a thermal anomaly, which is probably located within or just beneath the thermal boundary layer of the lithosphere. This inference contrasts with other regional models, which assume that isostatic compensation occurs at the base of the crust [Wellman, 1979a]. An important question then concerns the age of this dynamic support. Correlation between the amplitude of dynamic support and the elevation of prominent knickzones on either side of the drainage divide imply that onset of dynamic support can be determined provided that the age of knickzone formation is constrained. Inversion of river profiles suggests that regional dynamic uplift occurred between 80 and 10 Ma when volcanism occurred along the crest of the highlands. Possible links between uplift and Cenozoic volcanism have previously been downplayed due to the inferred antiquity of the Australian landscape which was thought to be responding to isostatic rebound [e.g., Bishop and Goldrick, 1999]. This inference was based upon observed rates of river incision and on the minimum age on uplift constrained by basaltic flows. In our river profile modeling, we have matched both incision rates and minimum age uplift constraints while demonstrating a temporal link between uplift and Cenozoic volcanism (Figures 15). Persistence of dynamic support in Eastern Australia over the last 80 Ma indicates that the inferred mantle thermal anomaly is either aligned north-south (i.e., parallel to Australia's rapid northward trajectory) or coupled to the lithospheric plate. Finn *et al.* [2005] proposed that volcanism in eastern Australia and western Antarctica is contemporaneous and spatially linked by low shear wave velocity zones within the upper mantle which could be interpreted as support for the first hypothesis. However, dynamic support of eastern Australia has a pronounced right-angle bend at  $\sim 27^\circ\text{S}$ . Immediately to the west, there is no evidence for successive waves of uplift and subsidence since a continuous succession of Cretaceous marine strata is preserved in the Darling

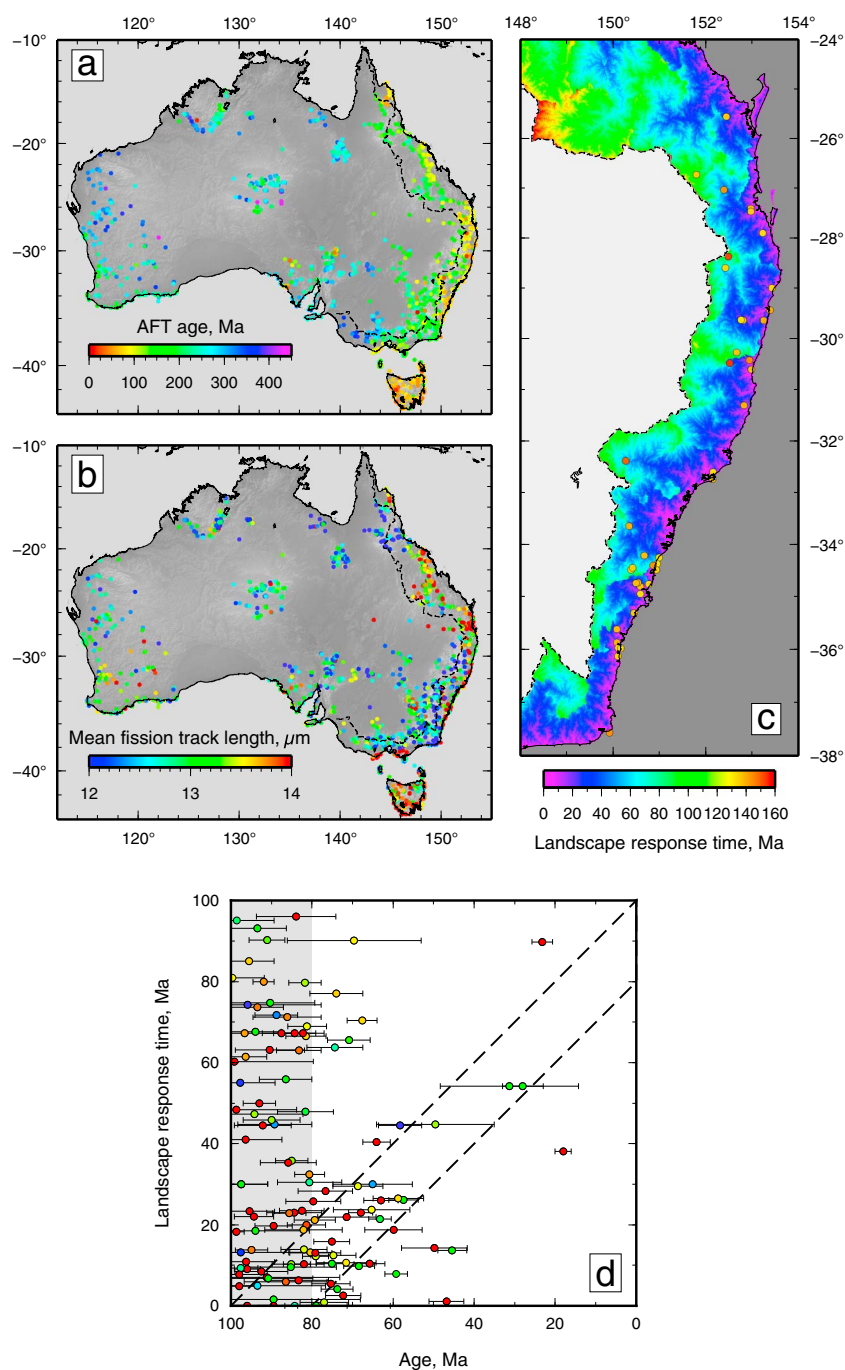


**Figure 23.** Apatite fission track ages from *Gleadow et al.* [2002] compared to landscape response time. (a) Apatite fission track ages. (b) Mean fission track length for each dated sample. (c) Landscape response time for eastern Australia overlain by apatite fission track ages  $\leq 80$  Ma, east of Great Divide. (d) Landscape response time as a function of apatite fission track ages and error colored by mean fission track length; light gray box = age of rifting leading to Tasman Sea floor spreading [Lowry and Longley, 1991; Veevers et al., 1991]; dashed band = expected relationship for knickzones initiated at the coast between 100 and 80 Ma; knickzones initiated inland will plot below this box.

Basin (Figures 1 and 3c). These observations suggest that the mantle thermal anomaly is confined to the thermal boundary layer of the lithospheric plate, which is consistent with seismic tomographic evidence.

Uplift of the Eastern Highlands is not only associated with growth of present-day dynamic support. There is evidence for an early (120–80 Ma) phase of uplift along the length of the Eastern Highlands. This event correlates with rifting along the eastern margin and with thermochronologic apatite fission track ages with



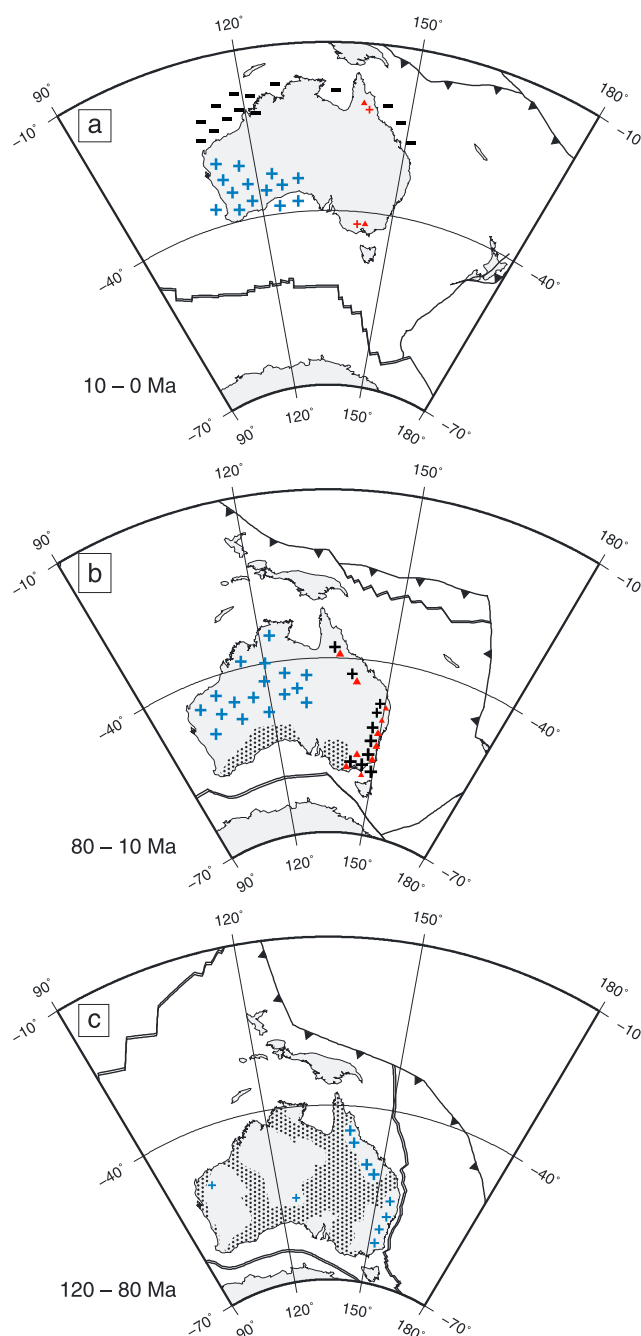


**Figure 24.** Cartoon showing Australia's major vertical motions in moving hot spot reference frame [Gurnis *et al.*, 2012]. Plus and minus signs = uplift and subsidence colored by the isostatic state prior to onset of vertical motion: blue = drawn down; black = unperturbed; red = uplifted. Red triangles = volcanoes; black dots = marine sediments of labeled age or younger. (a–b) Diachronous uplift of Western Australia associated with rapid northward translation. (b) Uplift associated with Cenozoic volcanism along the east coast. (c) Rift-related uplift of eastern Australia.

long mean tracks located east of the Great Escarpment [Rahmanian *et al.*, 1990; Lowry and Longley, 1991; Gleadow *et al.*, 2002]. The closing temperature for apatite fission tracks is  $110 \pm 10^\circ\text{C}$ , which corresponds to a minimum depth range of 1.8–2.2 km, based on a geothermal gradient calculated from mantle xenoliths [Kohn *et al.*, 2005; Cull *et al.*, 1991]. Thus, fission track data should be insensitive to formation of the < 1 km Great Escarpment. Yet there is good agreement between 60 Ma denudation predicted using fission track data and uplift of New England (Figures 15q–15r and 22c). It is straightforward to envisage how exhumation along normal faults can result in fission track cooling ages which correspond to the age of rifting along the margin between 100 and 80 Ma. However, younger ages might record the upstream propagation of inland

knickzones established during rifting. There is a spatial association between elevation along the Eastern Highlands and < 80 Ma fission track ages along the coastal strip (Figure 23c). To investigate whether these ages are related to the propagation of knickzones, we compare them with the landscape response time,  $\tau_G$ . Ages of knickzones which originate at the coast should plot within the diagonal dashed band in Figure 23d whereas knickzones originating inland will fall below the band. A cluster of data following this trend suggests that the fission track data and our landscape evolution model are mutually consistent. Together, these results indicate that the initial phase of rift-related uplift and erosion locked in the observed apatite fission track ages; yet it was the second phase of uplift and erosion which exposed these samples beneath the Great Escarpment. The second uplift event is unlikely to generate a denudational signal large enough to be measured by thermochronometry. Our uplift history also corresponds to the thermal evolution of the coastal plain, determined using lower temperature apatite (U–Th)/He thermochronometry (Figures 15e and 15k) [Persano *et al.*, 2005].

The precise uplift mechanism of the first, rift-related, uplift event remains unclear. Lister and Etheridge [1989] suggested that syn-rift uplift and mafic underplating were generated by a subplate thermal anomaly at the time of rifting. However, mapping of oceanic crustal thickness variation abutting the eastern Australian continental margin reveals an average crustal thickness of 6.4 km, which is 0.7 km thinner than the global average. These values imply that asthenospheric mantle was cool at the inception of the Tasman Sea (84–64 Ma) [Czarnota *et al.*, 2013]. Alternatively, there may have been a sharp gradient in asthenospheric temperature across the margin. Another explanation is that syn-rift uplift was caused by rebound from a previously drawdown state. Middle Cretaceous intracontinental flooding of eastern Australia has long been inferred to be the consequence of dynamic drawdown above a subducting slab [Gallagher, 1990; Gurnis *et al.*, 2000; Matthews *et al.*, 2011]. On removal of this negative mantle anomaly, the region should have rebounded to achieve isostatic equilibrium. This inference is supported by subsidence analysis combined with vitrinite and fission track data, which suggests that the central highlands underwent regional uplift with no change in upper crustal geothermal gradient prior to the onset of seafloor spreading [Raza *et al.*, 2009]. In contrast, oceanic crustal thickness is almost double the global average within the Coral Sea, where spreading began at ~62 Ma [Shor, 1967; Gaina *et al.*, 1999]. This observation implies a thermal anomaly within the mantle grew beneath northern Australia immediately before this time, consistent with a second phase of uplift along the Eastern Highlands (Figures 15 and 22).

It is probable that rapid south-north plate motion has caused diachronous uplift of the Western Plateau and subsequent drawdown of the Northwest Shelf (Figure 19) [Czarnota *et al.*, 2013]. Regional uplift is generated by emergence of Australia from a region of drawdown which is consistent with offshore estimates of residual topography and with the gradient of long-wavelength free-air gravity anomalies (Figure 1a). On the Northwest Shelf, regional uplift attained an unperturbed elevation before drawdown commenced. The amplitude of this drawdown is significant, and so our estimates of the amplitude of regional uplift of an area encompassing the Kimberley is likely to be a minimum. Timing of uplift of the Western Plateau corresponds with the age of Manganese oxide formation throughout Western Australia [Dammer *et al.*, 1999]. This correspondence suggests that development of low topographic gradients in a landscape may be critical for the growth of these supergene deposits. Kimberlitic intrusions in northwestern Australia coincide with the highest rates of uplift in the region. We attribute both processes to changes in the thermal regime at the base of the lithosphere.

## 6. Conclusions

The spatial and temporal pattern of Australian dynamic topography is difficult to constrain away from coastal strips where uplifted marine terraces and strata provide useful constraints [Sandiford, 2007]. We suggest that, when combined with local constraints for fluvial erosion, drainage patterns provide useful information. We have modeled an inventory of 254 longitudinal river profiles using a combination of inverse algorithms which permit the temporal and spatial history of uplift rate to be extracted. Our results suggest that the epeirogeny of Australia is largely a Cenozoic phenomenon. Uplift of the Eastern Highlands began at about 120 Ma and intensified during the Cenozoic Era associated with volcanism. Variations in vertical motion correlate with the sign of long-wavelength gravity anomalies which suggests that there are significant gradients in dynamic topography across the east coast of Australia. This spatial pattern of uplift does not match a simple north-south trend, although there is evidence for a north to south diachroneity. Immediately offshore, the oceanic floor is drawn down and basin sediments record anomalous Cenozoic subsidence

[Czarnota *et al.*, 2013]. In central and western Australia, inversion of river profiles, calibrated using the uplift histories of marine deposits, suggests that widespread regional uplift is dominantly of Cenozoic age. A marked north to south diachroneity is consistent with Australia's rapid, northward translation over slower moving or stationary long-wavelength convective cells within the mantle (Figure 24) [Czarnota *et al.*, 2013].

## Appendix A: Drainage Inventory

Vital statistics of drainage networks used in our analysis are given in Table A1.

**Table A1.** Attributes of Australian Rivers, Numbered in Figure 6

River Mouth Name <sup>a</sup>	River Head Name	Number	Longitude <sup>b</sup> at Mouth	Latitude <sup>b</sup> at Mouth	Longitude <sup>b</sup> at Head	Latitude <sup>b</sup> at Head	Elevation <sup>c</sup> (m)	Length <sup>d</sup> (km)	Basin <sup>e</sup> (km <sup>2</sup> )
Bynoe River	Cloncurry River	1	140.564	−17.599	140.709	−21.564	478	675	108,943
Bynoe River	McKinlay River	2	140.564	−17.599	140.753	−21.562	477	713	108,943
Bynoe River	O'Connell Creek	3	140.564	−17.599	143.602	−21.320	311	771	108,943
Bynoe River	Flinders River	4	140.564	−17.599	144.670	−19.923	805	1039	108,943
Bynoe River	Stawell River	5	140.564	−17.599	144.230	−19.636	908	915	108,943
Norman River	Norman River	6	140.828	−17.470	143.456	−19.475	657	571	63,031
Norman River	Gilbert River	7	140.828	−17.470	144.052	−19.585	1054	683	63,031
Gilbert River	Einasleigh River	8	141.288	−16.641	144.193	−19.586	909	666	26,167
Mitchell River	Lynd River	9	141.615	−15.215	144.766	−18.260	918	610	73,004
Mitchell River	Walsh River	10	141.615	−15.215	145.419	−17.298	1069	661	73,004
Mitchell River	Prospect Creek	11	141.615	−15.215	144.953	−16.317	819	570	73,004
Mitchell River	Big Coleman River	12	141.615	−15.215	143.457	−14.528	274	324	73,004
Holroyd River	Station Creek	13	141.543	−14.408	143.165	−14.052	266	260	4,956
West Archer River	The Dry River	14	141.716	−13.390	143.287	−13.791	665	305	12,457
Jardine River	McHenry River	15	142.246	−10.960	142.702	−11.665	131	154	3,001
Pascoe River	Pascoe River	16	143.241	−12.524	143.216	−13.041	354	121	1,912
Stewart River	Stewart River	17	143.675	−14.006	143.306	−13.897	558	101	831
North Kennedy River	Kennedy River	18	144.029	−14.482	143.765	−15.600	250	213	18,237
North Kennedy River	West Normanby River	19	144.029	−14.482	144.973	−16.152	974	346	18,237
Jeannie River	Jeannie River	20	144.916	−14.626	144.921	−14.907	327	56	588
Daintree River	Daintree River	21	145.452	−16.283	145.201	−16.376	1097	117	1,309
Barron River	Barron River	22	145.776	−16.942	145.533	−17.211	709	111	2,203
Johnstone River	North Johnstone River	23	146.031	−17.513	145.495	−17.490	1093	101	1,512
Herbert River	The Millstream	24	146.274	−18.506	145.531	−17.620	992	319	8,557
Crystal Creek	Unnamed	25	146.263	−18.863	146.188	−18.959	799	29	1,165
Burdekin River	Keelbottom Creek	26	147.490	−19.648	146.395	−19.198	617	484	131,219
Burdekin River	Dry River	27	147.490	−19.648	144.673	−18.480	787	693	131,219
Burdekin River	Gregory River	28	147.490	−19.648	144.372	−19.920	900	738	131,219
Burdekin River	Cape River	29	147.490	−19.648	144.939	−20.284	653	520	131,219
Burdekin River	Belyando River	30	147.490	−19.648	146.111	−21.734	433	459	131,219
Burdekin River	Alpha Creek	31	147.490	−19.648	146.554	−24.430	573	778	131,219
Burdekin River	Mistake Creek	32	147.490	−19.648	147.370	−22.959	462	585	131,219
Burdekin River	Sutton Creek	33	147.490	−19.648	148.306	−21.384	411	538	131,219
Burdekin River	Urannah Creek	34	147.490	−19.648	148.606	−20.990	814	339	131,219
Pioneer River	Rocky Dam Creek	35	149.198	−21.138	148.562	−21.358	753	115	1,511
Styx River	Granite Creek	36	149.636	−22.570	149.386	−22.540	476	45	1,010
Fitzroy River	Marlborough Creek	37	150.705	−23.502	149.929	−22.720	146	193	139,274
Fitzroy River	Hut Creek	38	150.705	−23.502	149.410	−22.054	455	620	139,274
Fitzroy River	Isaac River	39	150.705	−23.502	148.115	−21.465	503	746	139,274
Fitzroy River	Tomahawk Creek	40	150.705	−23.502	147.293	−23.504	664	806	139,274
Fitzroy River	Nogoa River	41	150.705	−23.502	147.002	−25.023	599	975	139,274
Fitzroy River	Peawaddy Creek	42	150.705	−23.502	148.077	−24.907	912	830	139,274
Fitzroy River	Comet Creek	43	150.705	−23.502	148.967	−25.358	601	877	139,274
Fitzroy River	Zamia Creek	44	150.705	−23.502	149.134	−25.114	469	583	139,274
Fitzroy River	Juandah Creek	45	150.705	−23.502	149.958	−26.400	407	807	139,274
Fitzroy River	North Kariboe Creek	46	150.705	−23.502	150.967	−24.487	751	555	139,274
Boyne River	Glassford Creek	47	151.358	−23.945	151.169	−24.576	608	138	2,405
Burnett River	Three Moon Creek	48	152.401	−24.759	151.016	−24.411	830	489	33,215
Burnett River	Johnson Creek	49	152.401	−24.759	150.788	−26.224	417	438	33,215
Burnett River	Barker Creek	50	152.401	−24.759	151.627	−26.870	670	448	33,215
Brisbane River	Emu Creek	51	153.149	−27.408	151.957	−27.234	634	321	13,556
Logan River	Burnett Creek	52	153.293	−27.698	152.589	−28.314	618	177	3,795
Clarence River	Cataract River	53	153.364	−29.429	152.116	−29.114	945	359	21,944
Clarence River	Oban River	54	153.364	−29.429	151.792	−30.097	1352	393	21,944
Clarence River	Nymboida River	55	153.364	−29.429	152.476	−30.352	1178	360	21,944
MacLeay River	Gara River	56	153.020	−30.905	151.702	−30.050	1350	354	11,264

Table A1. (continued)

River Mouth Name <sup>a</sup>	River Head Name	Number	Longitude <sup>b</sup> at Mouth	Latitude <sup>b</sup> at Mouth	Longitude <sup>b</sup> at Head	Latitude <sup>b</sup> at Head	Elevation <sup>c</sup> (m)	Length <sup>d</sup> (km)	Basin <sup>e</sup> (km <sup>2</sup> )
Hastings River	Fenwicks Creek	57	152.914	−31.424	151.997	−31.306	1051	142	3,662
Hunter River	Isis River	58	151.714	−32.862	151.011	−31.620	749	341	21,299
Hunter River	Blackwater Creek	59	151.714	−32.862	150.387	−32.811	736	312	21,299
Hawkesbury River	Bungleboori Creek	60	151.144	−33.471	150.239	−33.419	962	140	20,586
Hawkesbury River	Grose River	61	151.144	−33.471	150.283	−33.517	997	147	20,586
Hawkesbury River	Coxs River	62	151.144	−33.471	150.008	−33.370	973	279	20,586
Shoalhaven River	Bungonia Creek	63	150.747	−34.861	149.825	−34.835	707	130	6,985
Shoalhaven River	Shoalhaven River	64	150.747	−34.861	149.501	−35.818	1293	295	6,985
Tuross River	Jibolaro Creek	65	150.089	−36.069	149.455	−36.271	991	109	1,792
Genoa River	Genoa River	66	149.706	−37.499	149.217	−37.125	813	86	1,780
Snowy River	Bonang River	67	148.506	−37.772	148.805	−37.280	900	181	15,077
Snowy River	Snowy River	68	148.506	−37.772	148.301	−36.443	1842	383	15,077
Snowy River	Buchan River	69	148.506	−37.772	148.141	−36.865	1559	168	15,077
Mitchell River	Wongungarra River	70	147.652	−37.863	147.061	−37.051	1053	175	4,670
La Trobe River	Thomson River	71	147.457	−38.072	146.144	−37.630	1177	188	11,202
Yarra River	Baker Creek	72	144.941	−37.820	146.080	−37.669	931	153	3,894
Werribee River	Lerderderg River	73	144.674	−37.973	144.227	−37.431	739	95	1,421
Hopkins River	Fiery Creek	74	142.509	−38.405	143.251	−37.290	748	241	8,961
Glenelg River	Glenelg River	75	141.004	−38.053	142.284	−37.373	382	374	13,147
Murray River	Avoca River	76	139.382	−35.347	143.343	−37.291	566	1289	1,054,636
Murray River	Campaspe River	77	139.382	−35.347	144.425	−37.448	714	1343	1,054,636
Murray River	Big River	78	139.382	−35.347	146.165	−37.559	866	1501	1,054,636
Murray River	Ovens River	79	139.382	−35.347	147.072	−36.974	875	1488	1,054,636
Murray River	Gehee River	80	139.382	−35.347	148.400	−36.187	1761	1639	1,054,636
Murray River	Tumbarumba Creek	81	139.382	−35.347	148.118	−35.606	1098	1618	1,054,636
Murray River	Tumut River	82	139.382	−35.347	148.379	−36.153	1805	1757	1,054,636
Murray River	Cooma Creek	83	139.382	−35.347	149.067	−36.391	1023	1926	1,054,636
Murray River	Lachlan River	84	139.382	−35.347	149.548	−34.937	755	2235	1,054,636
Murray River	Wheeo Creek	85	139.382	−35.347	149.436	−34.486	994	2154	1,054,636
Murray River	Bolong River	86	139.382	−35.347	149.641	−34.457	941	2188	1,054,636
Murray River	Goobang Creek	87	139.382	−35.347	148.457	−33.017	634	1889	1,054,636
Murray River	Crowl Creek	88	139.382	−35.347	146.432	−32.317	362	1563	1,054,636
Murray River	Mulga Creek	89	139.382	−35.347	146.434	−31.650	313	1826	1,054,636
Murray River	Fish River	90	139.382	−35.347	149.828	−33.890	1202	2682	1,054,636
Murray River	Binnia Creek	91	139.382	−35.347	149.806	−31.706	733	2405	1,054,636
Murray River	MacDonald River	92	139.382	−35.347	151.619	−31.309	1190	2653	1,054,636
Murray River	Gwydir River	93	139.382	−35.347	151.644	−30.298	1292	2625	1,054,636
Murray River	Beardy Waters	94	139.382	−35.347	151.630	−29.948	1292	2724	1,054,636
Murray River	Condamine River	95	139.382	−35.347	151.951	−28.476	869	2855	1,054,636
Murray River	Oakey Creek	96	139.382	−35.347	152.018	−27.289	656	2743	1,054,636
Murray River	Maranoa River	97	139.382	−35.347	147.992	−24.930	847	2681	1,054,636
Murray River	Warrego River	98	139.382	−35.347	147.891	−24.832	898	2615	1,054,636
Murray River	Paroo River	99	139.382	−35.347	145.134	−26.109	350	2099	1,054,636
Murray River	Grasmere Creek	100	139.382	−35.347	142.396	−31.280	257	1230	1,054,636
Murray River	Olary Creek	101	139.382	−35.347	139.892	−32.528	463	1092	1,054,636
Murray River	Unnamed	102	139.382	−35.347	138.910	−33.042	552	456	1,054,636
Torrens River	Torrens River	103	138.509	−34.967	139.056	−34.763	450	73	610
Wakefield River	Wakefield River	104	138.108	−34.156	138.849	−33.932	451	122	5,601
Broughton River	Rocky River	105	137.910	−33.438	138.582	−32.921	610	139	2,365
Spear Creek	Spear Creek	106	137.845	−32.643	138.036	−32.546	554	25	88
Lake Torrens	Morgan Creek	107	137.755	−32.429	138.710	−31.996	632	245	1,356,600
Lake Torrens	Warrioota Creek	108	137.755	−32.429	138.714	−30.849	735	296	1,356,600
Lake Eyre	Taylor Creek	109	137.755	−32.429	139.114	−30.368	639	656	1,356,600
Lake Frome	Molkegna Creek	110	137.755	−32.429	138.688	−30.911	669	1145	1,356,600
Lake Frome	Siccas River	111	137.755	−32.429	138.729	−31.873	703	1296	1,356,600
Lake Frome	Pine Creek	112	137.755	−32.429	139.688	−32.461	449	1300	1,356,600
Lake Frome	Spring Creek	113	137.755	−32.429	141.498	−31.612	340	1370	1,356,600
Lake Frome	Williams Creek	114	137.755	−32.429	142.651	−30.801	235	1389	1,356,600
Lake Frome	Cardenyabba Creek	115	137.755	−32.429	143.733	−28.513	223	1560	1,356,600
Lake Frome	Thistle Creek	116	137.755	−32.429	145.339	−25.518	413	2220	1,356,600
Lake Eyre	Wilson River	117	137.755	−32.429	143.512	−27.221	208	1818	1,356,600
Lake Eyre	Windeyer Creek	118	137.755	−32.429	146.738	−24.667	575	2600	1,356,600
Lake Eyre	Aramac Creek	119	137.755	−32.429	145.733	−23.372	427	2602	1,356,600
Lake Eyre	Torrens Creek	120	137.755	−32.429	144.990	−20.380	649	2885	1,356,600
Lake Eyre	Rockwood Creek	121	137.755	−32.429	143.632	−21.405	320	2682	1,356,600
Lake Eyre	Wokingham Creek	122	137.755	−32.429	143.611	−21.390	319	2884	1,356,600
Lake Eyre	Mayne River	123	137.755	−32.429	142.800	−23.658	295	2638	1,356,600
Lake Eyre	Bustard Creek	124	137.755	−32.429	140.730	−21.582	458	2647	1,356,600



Table A1. (continued)

River Mouth Name <sup>a</sup>	River Head Name	Number	Longitude <sup>b</sup> at Mouth	Latitude <sup>b</sup> at Mouth	Longitude <sup>b</sup> at Head	Latitude <sup>b</sup> at Head	Elevation <sup>c</sup> (m)	Length <sup>d</sup> (km)	Basin <sup>e</sup> (km <sup>2</sup> )
Lake Eyre	Wills Creek	125	137.755	−32.429	139.550	−21.071	468	2686	1,356,600
Lake Eyre	Buckley River	126	137.755	−32.429	139.305	−20.279	412	3079	1,356,600
Lake Eyre	Ranken River	127	137.755	−32.429	137.465	−19.001	268	3138	1,356,600
Lake Eyre	Elkedra River	128	137.755	−32.429	134.985	−21.109	512	3211	1,356,600
Lake Eyre	Gillen Creek	129	137.755	−32.429	134.112	−23.253	800	3445	1,356,600
Lake Eyre	Tomahawk Creek	130	137.755	−32.429	135.764	−22.499	535	2911	1,356,600
Lake Eyre	Plenty River	131	137.755	−32.429	134.691	−23.122	730	2356	1,356,600
Lake Eyre	Todd River	132	137.755	−32.429	134.076	−23.458	779	2176	1,356,600
Lake Eyre	Ormiston Creek	133	137.755	−32.429	132.660	−23.489	840	2427	1,356,600
Lake Eyre	Eateringinna Creek	134	137.755	−32.429	132.364	−26.291	671	1795	1,356,600
Lake Eyre	Henrietta Creek	135	137.755	−32.429	133.955	−27.289	342	1046	1,356,600
Lake Eyre	Wattiwarriganna Creek	136	137.755	−32.429	135.385	−29.731	230	724	1,356,600
Unnamed	Hotel Creek	137	137.755	−32.429	137.114	−32.260	260	113	1,356,600
Unnamed	Salt Creek	138	137.481	−33.124	136.965	−32.630	227	102	4,174
Driver River	Gum Creek	139	136.482	−33.998	136.426	−33.574	321	105	1,279
Lake Malata	Unnamed	140	135.364	−34.388	135.895	−34.277	185	75	1,406
Eucla Basin	Unnamed	141	133.839	−32.254	133.500	−27.085	386	964	178,751
Eucla Basin	Officer Creek	142	133.839	−32.254	132.103	−26.206	805	1254	178,751
Eucla Basin	Unnamed	143	131.213	−31.480	131.765	−30.217	227	206	75,626
Eucla Basin	Unnamed	144	131.213	−31.480	129.878	−26.040	794	1005	75,626
Eucla Basin	Unnamed	145	129.020	−31.685	126.588	−26.612	518	876	78,507
Eucla Basin	Unnamed	146	125.086	−32.721	125.550	−26.117	487	1438	456,797
Eucla Basin	Lake Mckay Paleodrainage	147	125.086	−32.721	125.313	−24.603	480	1641	456,797
Eucla Basin	Unnamed	148	125.086	−32.721	119.350	−26.002	630	1644	456,797
Eucla Basin	Pontoon Creek	149	125.086	−32.721	119.124	−28.105	525	1195	456,797
Eucla Basin	Unnamed	150	125.086	−32.721	120.686	−30.921	513	1070	456,797
Eucla Basin	Unnamed	151	125.086	−32.721	119.885	−32.663	427	828	456,797
Bandy Creek	Unnamed	152	121.935	−33.830	122.358	−32.236	368	383	18,896
Lort River	Unnamed	153	121.196	−33.799	121.244	−32.308	402	244	12,219
Unnamed	Unnamed	154	120.051	−33.921	120.050	−32.991	393	185	3,641
Kalgan River	Boonawarrup Creek	155	117.976	−34.930	117.947	−34.376	326	104	2,696
Bow River	Frankland River	156	116.963	−34.983	117.097	−34.017	317	175	4,974
Blackwood River	Coblinine River	157	115.204	−34.264	118.410	−33.689	345	593	21,483
Collie River	Bingham River	158	115.695	−33.308	116.535	−33.220	332	140	4,055
Murray River	Hotham River	159	115.725	−32.780	117.330	−32.589	373	281	7,680
Swan River	Salt River	160	115.736	−32.056	119.119	−31.975	428	572	124,322
Swan River	Lake Seabrook Drainage	161	115.736	−32.056	119.798	−32.660	422	1070	124,322
Swan River	Hamersley Lakes Drainage	162	115.736	−32.056	119.048	−29.621	532	763	124,322
Swan River	Mortlock Creek	163	115.736	−32.056	117.161	−30.666	361	390	124,322
Moore River	Moore River	164	115.513	−31.351	116.622	−30.287	325	268	77,779
Moore River	Lake Moore Drainage	165	115.513	−31.351	118.737	−29.612	498	799	77,779
Moore River	Mongers Lake Drainage	166	115.513	−31.351	118.086	−28.692	496	730	77,779
Moore River	Salt River	167	115.513	−31.351	118.091	−28.520	498	778	77,779
Greenough River	Greenough River	168	114.655	−28.874	116.702	−27.813	449	381	12,318
Murchison River	Roderick River	169	114.164	−27.705	117.289	−26.949	509	617	102,743
Murchison River	Hope River	170	114.164	−27.705	119.280	−26.540	617	1073	102,743
Murchison River	Murchison River	171	114.164	−27.705	119.231	−25.956	615	940	102,743
Gascoyne River	Gascoyne River	172	113.657	−24.860	119.710	−24.632	657	981	71,986
Wooramel River	Wooramel River	173	114.240	−25.879	117.092	−25.619	451	416	15,548
Gascoyne River	Lyons River	174	113.657	−24.860	117.908	−24.498	652	687	71,986
Lyndon River	Lyndon River	175	113.635	−24.802	115.584	−23.720	324	428	30,276
Ashburton River	Brumby Creek	176	114.684	−21.830	119.430	−24.658	742	831	75,092
Ashburton River	Angelo River	177	114.684	−21.830	118.695	−23.220	889	753	75,092
Ashburton River	Hardey River	178	114.684	−21.830	117.832	−22.681	800	537	75,092
Robe River	Robe River	179	115.680	−21.317	117.360	−22.265	790	305	7,406
Fortescue River	Jigalong Creek	180	116.097	−21.027	120.871	−23.521	608	760	47,265
Yule River	Cockeraga River	181	118.186	−20.376	118.755	−22.084	466	256	8,653
De Grey River	Shaw River	182	119.175	−20.006	119.638	−22.271	476	346	465,407
De Grey River	Rudall River	183	119.175	−20.006	121.958	−22.466	462	730	465,407
De Grey River	Savory Creek	184	119.175	−20.006	120.126	−24.144	650	1272	465,407
De Grey River	Ilgarari Creek Drainage	185	119.175	−20.006	119.481	−24.613	711	1467	465,407
De Grey River	Lake Burnside Drainage	186	119.175	−20.006	121.446	−25.445	611	1345	465,407
De Grey River	Lake Carnegie Drainage	187	119.175	−20.006	120.923	−25.292	629	1581	465,407
De Grey River	Lake Wells Drainage	188	119.175	−20.006	122.523	−27.728	572	1571	465,407
De Grey River	Unnamed	189	119.175	−20.006	126.267	−22.390	406	1076	465,407
De Grey River	Lake Percival Drainage	190	119.175	−20.006	126.888	−21.450	470	1318	465,407
De Grey River	Lake Dora Drainage	191	119.175	−20.006	123.411	−21.325	313	692	465,407
De Grey River	Lake Waukarlycarly Drainage	192	119.175	−20.006	122.805	−21.299	319	529	465,407

Table A1. (continued)

River Mouth Name <sup>a</sup>	River Head Name	Number	Longitude <sup>b</sup> at Mouth	Latitude <sup>b</sup> at Mouth	Longitude <sup>b</sup> at Head	Latitude <sup>b</sup> at Head	Elevation <sup>c</sup> (m)	Length <sup>d</sup> (km)	Basin <sup>e</sup> (km <sup>2</sup> )
Unnamed	Unnamed	193	120.845	−19.679	125.972	−20.829	348	786	209,030
Unnamed	Unnamed	194	120.845	−19.679	127.503	−22.608	456	1188	209,030
Unnamed	Lake Gregory Drainage	195	120.845	−19.679	129.838	−19.381	469	1227	209,030
Unnamed	Sturt Creek	196	120.845	−19.679	130.011	−18.927	503	1351	209,030
Unnamed	Wolfe Creek	197	120.845	−19.679	127.286	−18.953	437	1023	209,030
Unnamed	Unnamed	198	122.609	−16.964	122.763	−17.394	169	99	1,792
Fitzroy River	Unnamed	199	123.581	−17.597	123.174	−18.533	240	169	83,660
Fitzroy River	Christmas Creek	200	123.581	−17.597	127.237	−18.993	408	635	83,660
Fitzroy River	Leopold River	201	123.581	−17.597	127.081	−17.513	597	638	83,660
Fitzroy River	Hann River	202	123.581	−17.597	125.969	−16.259	658	781	83,660
Fitzroy River	Mount Hardman Creek	203	123.608	−17.580	125.237	−17.803	261	323	11,088
May River	Barker River	204	123.922	−17.259	124.881	−16.717	402	204	10,127
Isdell River	Plain Creek	205	124.827	−16.431	125.610	−16.618	526	175	5,483
Prince Regent River	Prince Regent River	206	125.075	−15.457	125.799	−15.999	488	111	3,127
Roe River	Roe River	207	125.545	−15.213	125.703	−15.744	517	89	2,988
King Edward River	King Edward River	208	126.610	−14.263	126.123	−15.501	479	230	8,329
Drysdale River	Drysdale River	209	126.938	−14.025	125.944	−16.255	679	425	15,288
Durack River	North Creek	210	127.840	−15.605	127.118	−17.174	584	363	13,978
Ord River	Wilson River	211	128.371	−15.505	127.389	−17.305	566	445	50,787
Ord River	Black Elvire River	212	128.371	−15.505	127.606	−18.500	465	571	50,787
Ord River	Stirling Creek	213	128.371	−15.505	130.003	−17.822	442	482	50,787
Victoria River	Baines river	214	129.932	−15.441	129.732	−17.081	364	312	657,136
Victoria River	Wickham River	215	129.932	−15.441	130.000	−17.219	377	525	657,136
Victoria River	Victoria River	216	129.932	−15.441	129.994	−17.838	425	648	657,136
Victoria River	Winnecke Creek	217	129.932	−15.441	130.012	−18.933	504	907	657,136
Victoria River	Wilson Creek	218	129.932	−15.441	130.008	−18.963	492	1326	657,136
Lake Hopkins	Hull River	219	129.932	−15.441	129.537	−25.264	723	2453	657,136
Lake Amadeus	Beare Creek	220	129.932	−15.441	131.368	−26.227	756	2759	657,136
Lake Lewis	Fifteen Mile Creek	221	129.932	−15.441	134.108	−23.299	815	2561	657,136
Lake MacKay	Waite Creek	222	129.932	−15.441	130.798	−22.263	655	2176	657,136
Victoria River	Buger Creek	223	129.932	−15.441	130.770	−22.251	652	1757	657,136
Victoria River	Cockatoo Creek	224	129.932	−15.441	132.099	−22.204	694	1835	657,136
Victoria River	Lander River	225	129.932	−15.441	132.803	−22.360	720	1632	657,136
Victoria River	Hanson River	226	129.932	−15.441	132.922	−22.390	738	1587	657,136
Victoria River	Taylor Creek	227	129.932	−15.441	133.932	−21.738	612	1427	657,136
Victoria River	Bonney Creek	228	129.932	−15.441	134.674	−20.681	536	1334	657,136
Victoria River	Unnamed	229	129.932	−15.441	133.906	−19.292	382	1010	657,136
Lake Sylvester	Frew River	230	129.932	−15.441	134.981	−21.056	507	1737	657,136
Lake Sylvester	Playford River	231	129.932	−15.441	137.434	−18.631	335	1619	657,136
Lake Woods	Newcastle Creek	232	129.932	−15.441	135.450	−17.304	316	1153	657,136
Lake Woods	Newcastle Creek	233	129.932	−15.441	134.366	−16.485	297	1084	657,136
Lake Woods	Bucket Creek	234	129.932	−15.441	133.757	−16.140	267	1002	657,136
Victoria River	Bullock Creek	235	129.932	−15.441	132.440	−16.505	303	655	657,136
Victoria River	Angalarri River	236	129.932	−15.441	131.083	−15.143	296	191	657,136
Moyle River	Moyle River	237	129.748	−13.972	130.476	−14.326	313	117	3,436
Daly River	Dinnabung Creek	238	130.258	−13.326	131.042	−14.436	298	460	53,853
Daly River	Forrest Creek	239	130.258	−13.326	132.062	−16.103	256	619	53,853
Daly River	Fergusson River	240	130.258	−13.326	132.567	−13.774	340	472	53,853
Mary River	Mary River	241	131.690	−12.281	132.561	−13.693	369	293	7,799
East Alligator River	East Alligator River	242	132.752	−12.141	133.196	−13.332	402	215	7,669
Liverpool River	Mann River	243	134.155	−12.170	133.353	−13.358	411	242	7,327
Glyder River	Goyder River	244	135.057	−12.261	135.198	−13.465	255	193	10,267
Roper River	Wilton River	245	135.327	−14.712	133.586	−13.499	370	421	76,412
Roper River	Waterhouse River	246	135.327	−14.712	133.204	−13.867	373	557	76,412
Roper River	Western Creek	247	135.327	−14.712	132.424	−16.462	305	630	76,412
Roper River	Arnold River	248	135.327	−14.712	134.321	−16.484	299	461	76,412
McArthur River	Sandy Creek	249	136.676	−15.813	135.570	−17.375	315	318	17,900
Settlement Creek	Bullet Creek	250	138.318	−16.778	137.644	−17.584	304	154	6,768
Nicholson River	Coanjula Creek	251	139.266	−17.336	136.656	−17.549	328	453	46,522
Nicholson River	Fish-hole Creek	252	139.266	−17.336	137.597	−18.680	335	413	46,522
Leichhardt River	Gidya Creek	253	139.795	−17.576	139.355	−20.284	427	470	32,572
Leichhardt River	Leichhardt River	254	139.795	−17.576	139.751	−21.090	482	562	32,572

<sup>a</sup>Mouth of rivers labeled lake or Eucla Basin indicate rivers which do not drain into the ocean directly or via interconnected lake systems.

<sup>b</sup>In decimal degrees.

<sup>c</sup>Maximum elevation.

<sup>d</sup>Length from river head to the coast.

<sup>e</sup>Drainage area calculated from SRTM data set, measured at the coast.

## Acknowledgments

K.C. publishes with the permission of the CEO of Geoscience Australia. We thank D. McKenzie and A. Crosby for assistance with admittance calculations and M. Hoggard for comments and advice. M. Sandiford provided a thoughtful review. G.G.R. is supported by BP Exploration. S.F. is supported by NERC New Investigator grant NE/G000859/1. Geocat 78680. Earth Sciences contribution esc.2933.

## References

- Anderson, R. N., D. McKenzie, and J. G. Sclater (1973), Gravity, bathymetry and convection in the Earth, *Earth Planet. Sci. Lett.*, **18**(3), 391–407, doi:10.1016/0012-821X(73)90095-2.
- Belton, D. X., R. W. Brown, B. P. Kohn, D. Fink, and K. A. Farley (2004), Quantitative resolution of the debate over antiquity of the central Australian landscape: Implications for the tectonic and geomorphic stability of cratonic interiors, *Earth Planet. Sci. Lett.*, **219**(1–2), 21–34, doi:10.1016/S0012-821X(03)00705-2.
- Bernecker, T., and A. D. Partridge (2005), Approaches to palaeogeographic reconstructions of the Latrobe Group, Gippsland Basin, southeastern Australia, *APPEA J.*, **45**, 581–599.
- Bishop, P. (1982), Stability or change: A review of ideas on ancient drainage in eastern New South Wales, *Aust. Geogr.*, **15**(4), 219–230, doi:10.1080/00049188208702820.
- Bishop, P. (1989), Geomorphology and evolution of the Eastern Highlands, in *Intraplate Volcanism in Eastern Australia and New Zealand*, edited by R. W. Johnson, pp. 21–26, Cambridge Univ. Press, Cambridge, U.K.
- Bishop, P., and G. Goldrick (1999), Geomorphological evolution of the east Australia continental margin, in *Geomorphology and Global Tectonics*, edited by M. A. Summerfield, pp. 225–254, Wiley, Chichester, U.K.
- Bishop, P., R. W. Young, and I. McDougall (1985), Stream profile change and long-term landscape evolution: Early Miocene and modern rivers of the East Australian Highland crest, central New South Wales, Australia, *J. Geol.*, **93**(4), 455–474.
- Braun, J., D. R. Burbidge, F. N. Gesto, M. Sandiford, A. J. W. Gleadow, B. P. Kohn, and P. R. Cummins (2009), Constraints on the current rate of deformation and surface uplift of the Australian continent from a new seismic database and low-T thermochronological data, *Aust. J. Earth Sci.*, **56**(2), 99–110, doi:10.1080/08120090802546977.
- Brown, N. J., W. E. Featherstone, G. Hu, and G. M. Johnston (2011), AUSGeoid09: A more direct and more accurate model for converting ellipsoidal heights to AHD heights, *J. Spat. Sci.*, **56**(1), 27–37, doi:10.1080/14498596.2011.580498.
- Chen, X. Y., and C. E. Barton (1991), Onset of aridity and dune-building in central Australia: Sedimentological and magnetostratigraphic evidence from Lake Amadeus, *Palaeogeogr. Palaeoclimatol. Palaeoecol.*, **84**(1–4), 55–73, doi:10.1016/0031-0182(91)90035-P.
- Chen, X. Y., J. M. Bowler, and J. W. Magee (1991), Aeolian landscapes in central Australia: Gypsiferous and quartz dune environments from Lake Amadeus, *Sedimentology*, **38**(3), 519–538, doi:10.1111/j.1365-3091.1991.tb00365.x.
- Christensen, N. I. (1982), Seismic velocities, in *Handbook of Physical Properties of Rocks*, vol. 2, edited by R. S. Carmichael, pp. 57–74, CRC Press, Boca Raton, Fla.
- Clark, D., A. McPherson, and C. Collins (2011), Australia's seismogenic neotectonic record: A case for heterogeneous intraplate deformation, *Geoscience Australia, Record 2011/11*, 95.
- Coblentz, D. D., M. Sandiford, R. M. Richardson, S. Zhou, and R. Hillis (1995), The origins of the intraplate stress field in continental Australia, *Earth Planet. Sci. Lett.*, **133**(3–4), 299–309, doi:10.1016/0012-821X(95)00084-P.
- Collins, L. B., and J. L. Baxter (1984), Heavy mineral-bearing strandline deposits associated with high-energy beach environments, southern Perth Basin, Western Australia, *Aust. J. Earth Sci.*, **31**(3), 287–292, doi:10.1080/14400958408527931.
- Crosby, A. G. (2007), An assessment of the accuracy of admittance and coherence estimates using synthetic data, *Geophys. J. Int.*, **171**(1), 25–54, doi:10.1111/j.1365-246X.2007.03520.x.
- Crosby, A. G., and D. McKenzie (2009), An analysis of young ocean depth, gravity and global residual topography, *Geophys. J. Int.*, **178**(3), 1198–1219, doi:10.1111/j.1365-246X.2009.04224.x.
- Cull, J. P., S. Y. O'Reilly, and W. L. Griffin (1991), Xenolith geotherms and crustal models in eastern Australia, *Tectonophysics*, **192**(3–4), 359–366, doi:10.1016/0040-1951(91)90109-6.
- Czarnota, K., M. J. Hoggard, N. White, and J. Winterbourne (2013), Spatial and temporal patterns of Cenozoic dynamic topography around Australia, *Geochem. Geophys. Geosyst.*, **14**, 634–658, doi:10.1029/2012GC004392.
- Dammer, D., I. McDougall, and A. R. Chivas (1999), Timing of weathering-induced alteration of manganese deposits in Western Australia: evidence from K/Ar and <sup>40</sup>Ar/<sup>39</sup>Ar dating, *Econ. Geol.*, **94**(1), 87–108, doi:10.2113/gsecongeo.94.1.87.
- Demidjuk, Z., S. Turner, M. Sandiford, R. George, J. Foden, and M. Etheridge (2007), U-series isotope and geodynamic constraints on mantle melting processes beneath the Newer Volcanic Province in South Australia, *Earth Planet. Sci. Lett.*, **261**(3–4), 517–533, doi:10.1016/j.epsl.2007.07.006.
- DiCaprio, L., M. Gurnis, and R. D. Müller (2009), Long-wavelength tilting of the Australian continent since the Late Cretaceous, *Earth Planet. Sci. Lett.*, **278**(3–4), 175–185, doi:10.1016/j.epsl.2008.11.030.
- Dodson, J. R., and H. Lu (2005), Salinity episodes and their reversal in the late Pliocene of south-western Australia, *Palaeogeogr. Palaeoclimatol. Palaeoecol.*, **228**(3–4), 296–304, doi:10.1016/j.palaeo.2005.06.006.
- English, P., N. A. Spooner, J. Chappell, D. G. Questiaux, and N. G. Hill (2001), Lake Lewis basin, central Australia: Environmental evolution and OSL chronology, *Quat. Int.*, **83–85**, 81–101, doi:10.1016/S1040-6182(01)00032-5.
- Ewart, A., K. Baxter, and J. A. Ross (1980), The petrology and petrogenesis of the Tertiary anorogenic mafic lavas of southern and central Queensland, Australia—Possible implications for crustal thickening, *Contrib. Mineral. Petrol.*, **75**(2), 129–152, doi:10.1007/BF00389774.
- Farr, T. G., et al. (2007), The shuttle radar topography mission, *Rev. Geophys.*, **45**, RG2004, doi:10.1029/2005RG000183.
- Ferguson, J., R. J. Arculus, and J. Joyce (1979), Kimberlite and kimberlitic intrusives of southeastern Australia: A review, *Aust. Bur. Miner. Res. J. Aust. Geol. Geophys.*, **4**, 227–241.
- Finlayson, D. M. (1979), Seismic structure of southeastern Australia and constraints on crustal evolution, *Bur. Miner. Res., Australia, Record*, **1979/2**, 35–38.
- Finn, C. A., R. D. Müller, and K. S. Panter (2005), A Cenozoic diffuse alkaline magmatic province (DAMP) in the southwest Pacific without rift or plume origin, *Geochem. Geophys. Geosyst.*, **6**, Q02005, doi:10.1029/2004GC000723.
- Fishwick, S., and N. Rawlinson (2012), 3-D structure of the Australian lithosphere from evolving seismic datasets, *Aust. J. Earth Sci.*, **59**(6), 809–826, doi:10.1080/08120099.2012.702319.
- Förste, C., et al. (2011), EIGEN-6—A new combined global gravity field model including GOCE data from the collaboration of GFZ-Potsdam and GRGS-Toulouse, *Geophys. Res. Abst.*, **31**(EGU General Assembly), EGU2011-3242-2.
- Frakes, L. A., et al. (1987), Australian Cretaceous shorelines, stage by stage, *Palaeogeogr. Palaeoclimatol. Palaeoecol.*, **59**, 31–48, doi:10.1016/0031-0182(87)90072-1.
- Fujioka, T., and J. Chappell (2010), History of Australian aridity: Chronology in the evolution of arid landscapes, *Geol. Soc. London, Spec. Pub.*, **346**(1), 121–139, doi:10.1144/SP346.8.
- Gaina, C., D. R. Müller, J.-Y. Royer, J. Stock, J. Hardebeck, and P. Symonds (1998), The tectonic history of the Tasman Sea: A puzzle with 13 pieces, *J. Geophys. Res.*, **103**(B6), 12,413–12,433, doi:10.1029/98JB00386.
- Gaina, C., R. D. Müller, J.-Y. Royer, and P. Symonds (1999), Evolution of the Louisiade triple junction, *J. Geophys. Res.*, **104**(B6), 12,927–12,939, doi:10.1029/1999JB900038.

- Gallagher, K. (1990), Permian to Cretaceous subsidence history along the Eromanga–Brisbane geoscience transect, in *The Eromanga–Brisbane Geoscience Transect: A Guide to Basin Development Across Phanerozoic Australia in Southern Queensland*, vol. 232, edited by D. M. Finlayson, pp. 133–151, *Bur. Miner. Res. Bull.*, Canberra, Australia.
- Gleadow, A. J. W., B. P. Kohn, R. W. Brown, P. B. O'Sullivan, and A. Raza (2002), Fission track thermotectonic imaging of the Australian continent, *Tectonophysics*, 349(1–4), 5–21, doi:10.1016/S0040-1951(02)00043-4.
- Goleby, B. R., R. D. Shaw, C. Wright, B. L. N. Kennett, and K. Lambeck (1989), Geophysical evidence for 'thick-skinned' crustal deformation in central Australia, *Nature*, 337(6205), 325–330, doi:10.1038/337325a0.
- Griffin, W. L., F. L. Sutherland, and J. D. Hollis (1987), Geothermal profile and crust-mantle transition beneath east-central Queensland: Volcanology, xenolith petrology and seismic data, *J. Volcanol. Geotherm. Res.*, 31(3–4), 177–203, doi:10.1016/0377-0273(87)90067-9.
- Gurnis, M., L. Moresi, and D. M. Müller (2000), Models of mantle convection incorporating plate tectonics: The Australian region since the Cretaceous, in *The History and Dynamics of Global Plate Motions*, *Geophys. Monogr. Ser.*, vol. 121, edited by M. A. Richards, R. G. Gordon, and R. D. Van Der Hilst, pp. 211–238, AGU, Washington, D. C., doi:10.1029/GM121p0211.
- Gurnis, M., M. Turner, S. Zahirovic, L. DiCaprio, S. Spasojevic, R. D. Müller, J. Boyden, M. Seton, V. C. Manea, and D. J. Bower (2012), Plate tectonic reconstructions with continuously closing plates, *Comput. Geosci.*, 38(1), 35–42, doi:10.1016/j.cageo.2011.04.014.
- Hack, J. T. (1957), Studies of longitudinal stream profiles in Virginia and Maryland, *U.S. Geol. Surv. Prof. Pap.*, 294B, 45–80.
- Haig, D. W., and A. J. Mory (2003), New record of siliceous, marine, later Eocene from Kalbarri, Western Australia, *J. R. Soc. West. Aust.*, 86, 107–113.
- Hancock, G. R., C. Martinez, K. G. Evans, and D. R. Molire (2006), A comparison of SRTM and high-resolution digital elevation models and their use in catchment geomorphology and hydrology: Australian examples, *Earth Surf. Process. Landforms*, 31(11), 1394–1412, doi:10.1002/esp.1335.
- Heine, C., R. D. Müller, B. Steinberger, and L. DiCaprio (2010), Integrating deep Earth dynamics in paleogeographic reconstructions of Australia, *Tectonophysics*, 483(1–2), 135–150, doi:10.1016/j.tecto.2009.08.028.
- Herczeg, A. L., and A. Chapman (1991), Uranium-series dating of lake and dune deposits in southeastern Australia: A reconnaissance, *Palaeogeogr. Palaeoclimatol. Palaeoecol.*, 84(1–4), 285–298, doi:10.1016/0031-0182(91)90049-W.
- Hesse, P. P., J. W. Magee, and S. van der Kaars (2004), Late Quaternary climates of the Australian arid zone: A review, *Quat. Int.*, 118–119, 87–102, doi:10.1016/S1040-6182(03)00132-0.
- Hillis, R. R., M. Sandiford, S. D. Reynolds, and M. C. Quigley (2008), Present-day stresses, seismicity and Neogene-to-Recent tectonics of Australia's 'passive' margins: Intraplate deformation controlled by plate boundary forces, *Geol. Soc. London, Spec. Pub.*, 306(1), 71–90, doi:10.1144/sp306.3.
- Holdgate, G. R., C. Rodriguez, E. M. Johnstone, M. W. Wallace, and S. J. Gallagher (2003), The Gippsland Basin top Latrobe unconformity, and its expression in other SE Australian basins, *APPEA J.*, 43, 149–173.
- Holdgate, G. R., M. W. Wallace, S. J. Gallagher, B. E. Wagstaff, and D. Moore (2008), No mountains to snow on: Major post-Eocene uplift of the East Victoria Highlands; evidence from Cenozoic deposits, *Aust. J. Earth Sci.*, 55, 211–234, doi:10.1080/08120090701689373.
- Hou, B., L. A. Frakes, M. Sandiford, L. Worrall, J. Keeling, and N. F. Alley (2008), Cenozoic Eucla Basin and associated palaeovalleys, southern Australia – Climatic and tectonic influences on landscape evolution, sedimentation and heavy mineral accumulation, *Sediment. Geol.*, 203(1–2), 112–130, doi:10.1016/j.sedgeo.2007.11.005.
- Howard, A. D., W. E. Dietrich, and M. A. Seidl (1994), Modeling fluvial erosion on regional to continental scales, *J. Geophys. Res.*, 99(B7), 13,971–13,986, doi:10.1029/94JB00744.
- Jakica, S., M. C. Quigley, M. Sandiford, D. Clark, L. K. Fifield, and A. Alimanovic (2011), Geomorphic and cosmogenic nuclide constraints on escarpment evolution in an intraplate setting, Darling Escarpment, Western Australia, *Earth Surf. Process. Landforms*, 36(4), 449–459, doi:10.1002/esp.2058.
- Johnson, R. W. (1989), *Intraplate Volcanism in Eastern Australia and New Zealand*, Cambridge Univ. Press, Cambridge, U.K.
- Johnstone, E. M., C. C. Jenkins, and M. A. Moore (2001), An integrated structural and palaeogeographic investigation of Eocene erosion and related hydrocarbon potential in the Gippsland Basin, in *Eastern Australian Basins Symposium, a Refocused Energy Perspective for the Future*, edited by K. C. Hill and T. Bernecker, pp. 403–412, *Pet. Exp. Soc. Aust., Spec. Pub.*, Perth, Australia.
- Jones, J. G., and J. J. Veevers (1982), A Cainozoic history of Australia's Southeast Highlands, *J. Geol. Soc. Aust.*, 29(1–2), 1–12, doi:10.1080/00167618208729189.
- Jones, S. M., B. Lovell, and A. G. Crosby (2012), Comparison of modern and geological observations of dynamic support from mantle convection, *J. Geol. Soc. London*, 169(6), 745–758, doi:10.1144/jgs2011-118.
- Kershaw, A. P., H. A. Martin, and J. C. McEwen-Mason (1994), The Neogene: A time of transition, in *History of the Australian Vegetation: Cretaceous to Recent*, edited by R. S. Hill, pp. 299–327, Cambridge Univ. Press, Cambridge, U.K.
- Knesel, K. M., B. E. Cohen, P. M. Vasconcelos, and D. S. Thiede (2008), Rapid change in drift of the Australian plate records collision with Ontong Java Plateau, *Nature*, 454(7205), 754–757, doi:10.1038/nature07138.
- Kohn, B. P., A. J. Gleadow, R. W. Brown, K. Gallagher, M. Lorencak, and W. P. Noble (2005), Visualizing thermotectonic and denudation histories using apatite fission track thermochronology, *Rev. Mineral. Geochem.*, 58(1), 527–565, doi:10.2138/rmg.2005.58.20.
- Lambeck, K., and R. Stephenson (1985), Post-orogenic evolution of a mountain range: South-eastern Australian highlands, *Geophys. Res. Lett.*, 12(12), 801–804, doi:10.1029/GL012i012p00801.
- Langford, R., G. Wilford, E. Truswell, and A. Isern (1995), *Palaeogeographic Atlas of Australia – Cainozoic, Cretaceous*, vol. 10, Australian Geological Survey Organisation, Canberra, Australia.
- Leonard, M., I. Ripper, and L. Yue (2002), Australian earthquake fault plane solutions, *Geoscience Australia, Record 2002/19*, 114.
- Lister, G. S., and M. A. Etheridge (1989), Detachment models for uplift and volcanism in the Eastern Highlands, and their application to the origin of passive margin mountains, in *Intraplate Volcanism in Eastern Australia and New Zealand*, edited by R. W. Johnson, pp. 297–313, Cambridge Univ. Press, Cambridge, U.K.
- Lithgow-Bertelloni, C., and M. Gurnis (1997), Cenozoic subsidence and uplift of continents from time-varying dynamic topography, *Geology*, 25(8), 735–738.
- Longley, I. M., et al. (2002), The North West Shelf of Australia – A Woodside perspective, in *The Sedimentary Basins of Western Australia 3: Proceedings of the Petroleum Exploration Society of Australia Symposium*, edited by M. Keep and S. Moss, pp. 27–88, PESA, Perth.
- Lovering, J. F., and A. J. R. White (1969), Granulitic and eclogitic inclusions from basic pipes at Delegate, Australia, *Contrib. Mineral. Petrol.*, 21(1), 9–52, doi:10.1007/BF00377416.
- Lowry, D. C., and I. M. Longley (1991), A new model for the Mid-Cretaceous structural history of the northern Gippsland Basin, *APPEA J.*, 31, 143–153.
- Macphail, M. K., N. F. Alley, E. M. Truswell, and I. R. Sluiter (1994), Evidence from spores and pollen, in *History of the Australian Vegetation: Cretaceous to Recent*, edited by R. S. Hill, pp. 188–261, Cambridge Univ. Press, Cambridge, U.K.



- Marshallsea, S. J., P. F. Green, and J. Webb (2000), Thermal history of the Hodgkinson Province and Laura Basin, Queensland: Multiple cooling episodes identified from apatite fission track analysis and vitrinite reflectance data, *Aust. J. Earth Sci.*, **47**(4), 779–797, doi:10.1046/j.1440-0952.2000.00809.x.
- Matthews, K. J., A. J. Hale, M. Gurnis, R. D. Müller, and L. DiCaprio (2011), Dynamic subsidence of Eastern Australia during the Cretaceous, *Gondwana Res.*, **19**(2), 372–383, doi:10.1016/j.jgr.2010.06.006.
- McLaren, S., and M. W. Wallace (2010), Plio-Pleistocene climate change and the onset of aridity in southeastern Australia, *Global Planet. Change*, **71**(1–2), 55–72, doi:10.1016/j.gloplacha.2009.12.007.
- McKenzie, D. (2003), Estimating  $T_e$  in the presence of internal loads, *J. Geophys. Res.*, **108**(B9), 2438, doi:10.1029/2002JB001766.
- McKenzie, D. (2010), The influence of dynamically supported topography on estimates of  $t_e$ , *Earth Planet. Sci. Lett.*, **295**(1–2), 127–138, doi:10.1016/j.epsl.2010.03.033.
- McKenzie, D., and D. Fairhead (1997), Estimates of the effective elastic thickness of the continental lithosphere from Bouguer and free air gravity anomalies, *J. Geophys. Res.*, **102**(B12), 27,523–27,552, doi:10.1029/97JB02481.
- McKenzie, D., A. Watts, B. Parsons, and M. Roufousse (1980), Planform of mantle convection beneath the Pacific Ocean, *Nature*, **288**, 442–446, doi:10.1038/288442a0.
- Müller, R. D., M. Sdrolias, C. Gaina, and W. R. Roest (2008), Age, spreading rates, and spreading asymmetry of the world's ocean crust, *Geochem. Geophys. Geosyst.*, **9**, Q04006, doi:10.1029/2007GC001743.
- Nanson, G. C., D. M. Price, and S. A. Short (1992), Wetting and drying of Australia over the past 300 ka, *Geology*, **20**(9), 791–794.
- Norvick, M. S., and M. A. Smith (2001), Mapping the plate tectonic reconstruction of southern and southeastern Australia and implications for petroleum systems, *APPEA J.*, **41**, 15–35.
- Nott, J., and S. Horton (2000), 180 Ma continental drainage divide in northeastern Australia: Role of passive margin tectonics, *Geology*, **28**(8), 763–766, doi:10.1130/0091-7613(2000)28<763:MCDDIN>2.0.CO;2.
- Nott, J., R. Young, and I. McDougall (1996), Wearing down, wearing back and gorge extension in the long-term denudation of a highland mass: Quantitative evidence from the Shoalhaven catchment, southeast Australia, *J. Geol.*, **104**(2), 224–232.
- Nott, J. F. (1992), Long-term drainage evolution in the Shoalhaven catchment, southeast highlands, Australia, *Earth Surf. Process. Landforms*, **17**(4), 361–374, doi:10.1002/esp.3290170406.
- Ollier, C. D. (1982), The Great Escarpment of eastern Australia: Tectonic and geomorphic significance, *J. Geol. Soc. Aust.*, **29**(1), 13–23, doi:10.1080/00167618208729190.
- Ollier, C. D., and C. F. Pain (1994), Landscape evolution and tectonics in southeastern Australia, *AGSO J. Aust. Geol. Geophys.*, **15**(3), 335–345.
- Ollier, C. D., G. F. M. Gaunt, and I. Jurkowski (1988), The Kimberley Plateau, Western Australia: A Precambrian erosion surface, *Z. Geomorphol.*, **32**, 239–246.
- O'Reilly, S., and W. L. Griffin (1985), A xenolith-derived geotherm for southeastern Australia and its geophysical implications, *Tectonophysics*, **111**(1–2), 41–63, doi:10.1016/0040-1951(85)90065-4.
- O'Reilly, S. Y., and M. Zhang (1995), Geochemical characteristics of lava-field basalts from eastern Australia and inferred sources: Connections with the subcontinental lithospheric mantle?, *Contrib. Mineral. Petrol.*, **121**(2), 148–170, doi:10.1007/s004100050096.
- O'Reilly, S. Y., W. Griffin, and A. Stabel (1988), Evolution of Phanerozoic eastern Australian lithosphere: Isotopic evidence for magmatic and tectonic underplating, *J. Petrol., Special Volume*(1), 89–108, doi:10.1093/petrology/Special\_Volume.1.89.
- O'Sullivan, P. B., D. L. Gibson, B. P. Kohn, B. Pillans, and C. F. Pain (2000), Long-term landscape evolution of the Northparkes region of the Lachlan Fold Belt, Australia: Constraints from fission track and paleomagnetic data, *J. Geol.*, **108**(1), 1–16, doi:10.1086/314388.
- Pain, C. F., B. J. Pillans, I. C. Roach, L. Worrall, and J. R. Wilford (2012), Old, flat and red – Australia's distinctive landscape, in *Shaping a Nation: A Geology of Australia*, edited by R. S. Blewett, pp. 227–275, Geoscience Australia and ANU E Press, Canberra.
- Parker, R. (1994), *Geophysical Inverse Theory*, Princeton Series in Geophysics, Princeton Univ. Press, Princeton, N. J.
- Parsons, B., and S. Daly (1983), The relationship between surface topography, gravity anomalies, and temperature structure of convection, *J. Geophys. Res.*, **88**(B2), 1129–1144, doi:10.1029/JB088iB02p01129.
- Persano, C., F. M. Stuart, P. Bishop, and D. N. Barfod (2002), Apatite (U–Th)/He age constraints on the development of the Great Escarpment on the southeastern Australian passive margin, *Earth Planet. Sci. Lett.*, **200**(1–2), 79–90, doi:10.1016/S0012-821X(02)00614-3.
- Persano, C., F. M. Stuart, P. Bishop, and T. J. Dempster (2005), Deciphering continental breakup in eastern Australia using low-temperature thermochronometers, *J. Geophys. Res.*, **110**, B12405, doi:10.1029/2004JB003325.
- Pillans, B. (2005), Geochronology of the Australian regolith, in *Regolith-Landscape Evolution Across Australia*, edited by R. R. Anand and P. de Broekert, pp. 41–61, CRC LEME, Perth, Australia.
- Pillans, B. (2007), Pre-Quaternary landscape inheritance in Australia, *J. Quat. Sci.*, **22**(5), 439–447, doi:10.1002/jqs.1131.
- Press, W. H., S. A. Teukolsky, W. T. Vetterling, and B. P. Flannery (1992), *Numerical Recipes in FORTRAN: The Art of Scientific Computing*, 2nd ed., Cambridge Univ. Press, Cambridge.
- Priestley, K., and D. McKenzie (2006), The thermal structure of the lithosphere from shear wave velocities, *Earth Planet. Sci. Lett.*, **244**(1–2), 285–301, doi:10.1016/j.epsl.2006.01.008.
- Pritchard, D., G. G. Roberts, N. J. White, and C. N. Richardson (2009), Uplift histories from river profiles, *Geophys. Res. Lett.*, **36**, L24301, doi:10.1029/2009GL040928.
- Purss, M. B. J., and J. Cull (2001), Heat-flow data in western Victoria, *Aust. J. Earth Sci.*, **48**(1), 1–4, doi:10.1046/j.1440-0952.2001.00840.x.
- Quigley, M. C., D. Clark, and M. Sandiford (2010), Tectonic geomorphology of Australia, *Geol. Soc. London, Spec. Pub.*, **346**(1), 243–265, doi:10.1144/sp346.13.
- Rahmanian, V. D., P. S. Moore, W. J. Mudge, and D. E. Spring (1990), Sequence stratigraphy and the habitat of hydrocarbons, Gippsland Basin, Australia, *Geol. Soc. London, Spec. Pub.*, **50**(1), 525–544, doi:10.1144/gsl.sp.1990.050.01.32.
- Raymond, O., R. Gallagher, R. Shaw, A. Yeates, H. Douth, D. Palfreyman, and D. Blake (2010), Surface geology of Australia 1:2 500 000 scale, 2010 edition [Digital Dataset], *Geoscience Australia, Commonwealth of Australia*, Canberra.
- Raymond, O., S. Liu, R. Gallagher, L. M. Highet, and W. Zhang (2012), Surface geology of Australia, 1:1 000 000 scale, 2012 ed. [Digital Dataset], *Geoscience Australia, Commonwealth of Australia*, Canberra, Australia.
- Raza, A., K. C. Hill, and R. J. Korsch (2009), Mid-Cretaceous uplift and denudation of the Bowen and Surat Basins, eastern Australia: Relationship to Tasman Sea rifting from apatite fission-track and vitrinite-reflectance data, *Aust. J. Earth Sci.*, **56**(3), 501–531, doi:10.1080/08120090802698752.
- Reynolds, S. D., D. D. Coblenz, and R. R. Hillis (2002), Tectonic forces controlling the regional intraplate stress field in continental Australia: Results from new finite element modeling, *J. Geophys. Res.*, **107**(B7), 2131, doi:10.1029/2001JB000408.
- Roach, I. C. (2004), Mineralogy, textures and P–T relationships of a suite of xenoliths from the Monaro Volcanic Province, New South Wales, Australia, *J. Petrol.*, **45**(4), 739–758, doi:10.1093/petrology/egg108.

- Roberts, G. G., and N. White (2010), Estimating uplift rate histories from river profiles using African examples, *J. Geophys. Res.*, *115*, B02406, doi:10.1029/2009JB006692.
- Roberts, G. G., N. J. White, G. L. Martin-Brandis, and A. G. Crosby (2012a), An uplift history of the Colorado Plateau and its surroundings from inverse modeling of longitudinal river profiles, *Tectonics*, *31*, TC4022, doi:10.1029/2012TC003107.
- Roberts, G. G., J. D. Paul, N. White, and J. Winterbourne (2012b), Temporal and spatial evolution of dynamic support from river profiles: A framework for Madagascar, *Geochem. Geophys. Geosyst.*, *13*, Q04004, doi:10.1029/2012GC004040.
- Rosenbloom, N. A., and R. S. Anderson (1994), Hillslope and channel evolution in a marine terraced landscape, Santa Cruz, California, *J. Geophys. Res.*, *99*(B7), 14,013–14,029, doi:10.1029/94JB00048.
- Salmon, M., B. L. N. Kennett, and E. Saygin (2013), Australian Seismological Reference Model (AuSREM): Crustal component, *Geophys. J. Int.*, *192*(1), 190–206, doi:10.1093/gji/ggs004.
- Sandiford, M. (2007), The tilting continent: A new constraint on the dynamic topographic field from Australia, *Earth Planet. Sci. Lett.*, *261*(1–2), 152–163, doi:10.1016/j.epsl.2007.06.023.
- Sandiford, M., and M. Quigley (2009), TOPO-OZ: Insights into the various modes of intraplate deformation in the Australian continent, *Tectonophysics*, *474*, 405–416, doi:10.1016/j.tecto.2009.01.028.
- Sandiford, M., M. Wallace, and D. Coblenz (2004), Origin of the in situ stress field in south-eastern Australia, *Basin Res.*, *16*(3), 325–338, doi:10.1111/j.1365-2117.2004.00235.x.
- Sandiford, M., M. Quigley, P. de Broekert, and S. Jakica (2009), Tectonic framework for the Cenozoic cratonic basins of Australia, *Aust. J. Earth Sci.*, *56*, 5–18, doi:10.1080/08120090902870764.
- Schoenbohm, L., K. Whipple, B. Burchfiel, and L. Chen (2004), Geomorphic constraints on surface uplift, exhumation, and plateau growth in the Red River region, Yunnan Province, China, *Geol. Soc. Am. Bull.*, *116*(7–8), 895–909, doi:10.1130/b25364.1.
- Shor, G. G. (1967), Seismic refraction profile in Coral Sea Basin, *Science*, *158*(3803), 911–913, doi:10.1126/science.158.3803.911.
- Sklar, L. S., and W. E. Dietrich (2001), Sediment and rock strength controls on river incision into bedrock, *Geology*, *29*(12), 1087–1090.
- Stewart, A. J., D. H. Blake, and C. D. Ollier (1986), Cambrian river terraces and ridgetops in central Australia - Oldest persisting landforms, *Science*, *233*(4765), 758–761, doi:10.1126/science.233.4765.758.
- Stock, J. D., and D. R. Montgomery (1999), Geologic constraints on bedrock river incision using the stream power law, *J. Geophys. Res.*, *104*(B3), 4983–4993, doi:10.1029/98JB02139.
- Strahler, A. N. (1952), Hypsometric (area-altitude) analysis of erosional topography, *Geol. Soc. Am. Bull.*, *63*(11), 1117–1142, doi:10.1130/0016-7606(1952)63[1117:HAAOET]2.0.CO;2.
- Taylor, G., G. R. Taylor, M. Bink, C. Foudoulis, I. Gordon, J. Hedstrom, J. Minello, and F. Whipple (1985), Pre-basaltic topography of the northern Monaro and its implications, *Aust. J. Earth Sci.*, *32*, 65–71, doi:10.1080/08120098508729313.
- Tkalčić, H., N. Rawlinson, P. Arroucau, A. Kumar, and B. L. N. Kennett (2012), Multistep modelling of receiver-based seismic and ambient noise data from WOMBAT array: Crustal structure beneath southeast Australia, *Geophys. J. Int.*, *189*(3), 1680–1700, doi:10.1111/j.1365-246X.2012.05442.x.
- Totterdell, J. M., B. E. Bradshaw, and J. B. Willcox (2003), Structural and tectonic setting, in *Petroleum Geology of South Australia*, v. 5: *Great Australian Bight*, edited by G. W. O'Brien, E. Parascioiu, and J. E. Hibbert, Department of Primary Industries, South Australia.
- van der Beek, P., and P. Bishop (2003), Cenozoic river profile development in the Upper Lachlan catchment (SE Australia) as a test of quantitative fluvial incision models, *J. Geophys. Res.*, *108*(B6), 2309, doi:10.1029/2002JB002125.
- van der Beek, P., and J. Braun (1998), Numerical modelling of landscape evolution on geological time-scales: A parameter analysis and comparison with the south-eastern highlands of Australia, *Basin Res.*, *10*(1), 49–68, doi:10.1046/j.1365-2117.1998.00056.x.
- van der Beek, P., and J. Braun (1999), Controls on post-mid-Cretaceous landscape evolution in the southeastern highlands of Australia: Insights from numerical surface process models, *J. Geophys. Res.*, *104*(B3), 4945–4966, doi:10.1029/1998JB900060.
- Van Der Beek, P. A., J. Braun, and K. Lambeck (1999), Post-Palaeozoic uplift history of southeastern Australia revisited: Results from a process-based model of landscape evolution, *Aust. J. Earth Sci.*, *46*(2), 157–172, doi:10.1046/j.1440-0952.1999.00701.x.
- Vasconcelos, P. M., K. M. Knesel, B. E. Cohen, and J. A. Heim (2008), Geochronology of the Australian Cenozoic: A history of tectonic and igneous activity, weathering, erosion, and sedimentation, *Aust. J. Earth Sci.*, *55*(6–7), 865–914, doi:10.1080/08120090802120120.
- Veevers, J. J., C. M. Powell, and S. R. Roots (1991), Review of sea-floor spreading around Australia. 1. Synthesis of the patterns of spreading, *Aust. J. Earth Sci.*, *38*(4), 373–389, doi:10.1080/08120099108727979.
- Watts, A. (2001), *Isostasy and Flexure of the Lithosphere*, Cambridge Univ. Press, Cambridge, U.K.
- Weber, U. D., K. C. Hill, R. W. Brown, K. Gallagher, B. P. Kohn, A. J. W. Gleadow, and D. A. Foster (2004), Sediment supply to the Gippsland Basin from thermal history analysis: Constraints on Emperor–Golden Beach reservoir composition, *APPEA J.*, *44*, 397–416.
- Weber, U. D., B. P. Kohn, A. J. W. Gleadow, and D. R. Nelson (2005), Low temperature Phanerozoic history of the northern Yilgarn Craton, Western Australia, *Tectonophysics*, *400*(1–4), 127–151, doi:10.1016/j.tecto.2005.03.008.
- Wellman, P. (1979a), On the isostatic compensation of Australian topography, *BMR J. Aust. Geol. Geophys.*, *4*, 373–382.
- Wellman, P. (1979b), On the Cainozoic uplift of the southeastern Australian highland, *J. Geol. Soc. Aust.*, *26*(1–2), 1–9, doi:10.1080/00167617908729061.
- Wellman, P. (1987), Eastern Highlands of Australia; their uplift and erosion, *BMR J. Aust. Geol. Geophys.*, *10*, 277–286.
- Wellman, P., and I. McDougall (1974a), Cainozoic igneous activity in eastern Australia, *Tectonophysics*, *23*(1–2), 49–65, doi:10.1016/0040-1951(74)90110-3.
- Wellman, P., and I. McDougall (1974b), Potassium-argon ages on the Cainozoic volcanic rocks of New South Wales, *J. Geol. Soc. Aust.*, *21*(3), 247–272, doi:10.1080/00167617408728849.
- Whipple, K. X., and G. E. Tucker (1999), Dynamics of the stream-power river incision model: Implications for height limits of mountain ranges, landscape response timescales, and research needs, *J. Geophys. Res.*, *104*(B8), 17,661–17,674, doi:10.1029/1999JB900120.
- Willgoose, G., R. L. Bras, and I. Rodriguez-Iturbe (1991), A coupled channel network growth and hillslope evolution model: 1. Theory, *Water Resour. Res.*, *27*(7), 1671–1684, doi:10.1029/91WR00935.
- Wynne, P., and B. Bacchin (2009), Index of gravity surveys, *Geoscience Australia, Record 2009/07*, 1–1832.
- Young, R., and I. McDougall (1993), Long-term landscape evolution – Early Miocene and modern rivers in southern New South Wales, Australia, *J. Geol.*, *101*(1), 35–49.
- Young, R. W. (1983), The tempo of geomorphological change: Evidence from southeastern Australia, *J. Geol.*, *91*(2), 221–230.
- Young, R. W. (1989), Crustal constraints on the evolution of the continental divide of eastern Australia, *Geology*, *17*(6), 528–530.
- Young, R. W., and I. McDougall (1982), Basalts and silcretes on the coast near Ulladulla, southern New South Wales, *J. Geol. Soc. Aust.*, *29*(3–4), 425–430, doi:10.1080/00167618208729224.
- Young, R. W., and I. McDougall (1985), The age, extent and geomorphological significance of the Sassafras basalt, south-eastern New South Wales, *Aust. J. Earth Sci.*, *32*(4), 323–331, doi:10.1080/08120098508729335.

- Young, R. W., and R. A. L. Wray (2000), Contribution to the theory of scarpland development from observations in central Queensland, Australia, *J. Geol.*, *108*(6), 705–719.
- Zheng, H., K.-H. Wyrwoll, Z. Li, and C. McA Powell (1998), Onset of aridity in southern Western Australia: A preliminary palaeomagnetic appraisal, *Global Planet. Change*, *18*(3–4), 175–187, doi:10.1016/S0921-8181(98)00019-8.
- Zoback, M. L. (1992), First- and second-order patterns of stress in the lithosphere: The World Stress Map Project, *J. Geophys. Res.*, *97*, 11,703–11,728, doi:10.1029/92JB00132.
- Zuber, M. T., T. D. Bechtel, and D. W. Forsyth (1989), Effective elastic thicknesses of the lithosphere and mechanisms of isostatic compensation in Australia, *J. Geophys. Res.*, *94*(B7), 9353–9367, doi:10.1029/JB094iB07p09353.